Effect of radiation damage on the migration behaviour of Europium implanted into both single crystalline 6H-SiC and polycrystalline SiC

Tshegofatso Magapeletse Mohlala

Submitted in partial fulfilment of the requirements

for the degree

Doctor Philosophy (PhD) in Physics

in the Faculty of Natural and Agricultural Sciences

University of Pretoria

Supervisor: Prof TT Hlatshwayo

Co supervisor: Prof JB Malherbe

June to July, 2021

UNIVERSITY OF PRETORIA

DECLARATION OF ORIGINALITY

This form must be submitted together with the copies of the dissertation/thesis/essay for the examiners.

TITLE: Mr

REGISTRATION NUMBER: 10064487

Full names: Tshegofatso Magapeletse Mohlala

STATEMENT BY CANDIDATE

I declare that the thesis, which I hereby submit for the degree PhD in Physics at the University of Pretoria, is my own work and has not previously been submitted by me for a degree at another university.

I am aware that, should the thesis be accepted, I must submit the additional copies as required by the relevant regulations at least six weeks before the next graduation ceremony, and that the degree will not be conferred if this requirement is not fulfilled.

SIGNATURE:…….

DATE:…….....

Summary

The containment of fission products (FPs) in a nuclear fuel particle is the biggest concern regarding the safety of high temperature reactors (HRTs). In modern high temperature gas cooled nuclear reactors (HTGRs), safety is improved by coating the fuel particle with layers of chemical vapour deposited carbon and silicon carbide (SiC). In this Tri-structural Isotropic (TRISO) fuel particle, SiC is the main barrier layer of FPs. The release of radioactive FPs through the silicon carbide (SiC) containment layer presents an issue of radiological health concern to the environment. During normal operation, The TRISO particle contains most of the important FPs with the exception of other key FPs such as: silver (Ag), cesium (Cs), strontium (Sr) and europium (Eu). Most investigations have been performed on the migration behaviour of Ag and very limited investigations have been performed on the migration behaviour of Cs, Sr and Eu. In this study, the influence of radiation damage in the migration behaviour of Eu implanted into SiC was investigated.

A model of ion implantation is known to be effective in simulating the neutron irradiation in a nuclear fuel particle, hence it was used in this study. Eu ions of 270 keV were implanted into polycrystalline SiC and single crystalline 6H-SiC to a fluence of 1×10^{16} cm^2 at room temperature (RT), 350 ^oC and 600 ^oC. Some of the as-implanted samples were sequentially annealed at temperatures of 1000 ^oC to 1400 ^oC, in steps of 100 ^oC for 5 hours. The as-implanted and implanted then annealed samples were characterized by Raman spectroscopy, scanning electron microscopy (SEM), x-ray photoluminescence spectroscopy (XPS) and Rutherford backscattering spectrometry (RBS).

Implantation at RT resulted in amorphization of the implanted layer in SiC for both polycrystalline and single crystalline samples, while implantation at 350 ^oC and 600 ^oC retained a defective SiC with slightly more defects in the 350 ^oC implanted samples than in the 600 ^oC implanted samples. The radiation damage gradually annealed out with increasing annealing temperature in all implanted samples. However, the full re-crystallization was not achieved at the highest annealing temperature of 1400 ^oC reached in this investigation.

The broadening of Eu depth profile, indicating some diffusion was taking place in the RT implanted polycrystalline SiC sample, was observed after annealing at 1000 ^oC up to 1300 ^oC. This broadening was accompanied by the formation of surface peak after annealing at 1000 ^oC, indicating the formation of europium oxalate compound on the surface. A larger

amount of Eu loss was observed after annealing at 1100 ^{o}C. There was a steady loss of Eu from 1200 ^{o}C up to 1400 ^{o}C. The diffusion coefficients of: 0.015, 0.033 and 0.035 nm^2/s were extracted at 1000 ^{o}C, 1100 ^{o}C and 1200 ^{o}C, respectively. Annealing the 350 ^{o}C implanted polycrystalline sample at 1000 ^{o}C resulted in the formation of rather small europium oxalate compound on the surface compared to the RT implanted polycrystalline SiC annealed at 1000 ^{o}C. Contrary to the RT implanted sample, no broadening was observed after annealing up to 1400 ^{o}C. However, the loss of Eu was observed after annealing at temperatures $\geq$ 1100 ^{o}C.

Unlike the RT and 350 ^{o}C implanted samples, annealing the 600 ^{o}C implanted polycrystalline sample at 1000 ^{o}C did not result in a formation of europium oxalate surface peak. A slight broadening was observed after annealing the 600 ^{o}C implanted polycrystalline sample at temperatures of 1100 ^{o}C and higher. Due to the error limit of the RBS system used, no reliable diffusion coefficients could be extracted for this sample at these annealing temperatures. Almost all Eu was retained after annealing the 600 ^{o}C implanted samples at all temperatures.

Annealing the RT implanted 6H-SiC at temperatures from 1000 ^{o}C to 1400 ^{o}C resulted in the behaviour similar to that observed in the RT implanted polycrystalline sample annealed in the same temperature range. Similar to the polycrystalline SiC, the highest loss of Eu was recorded after annealing at 1100 ^{o}C. Ultimately, the loss of Eu was steady in the samples annealed at 1200 ^{o}C up to 1400 ^{o}C. The diffusion coefficients of 0.017, 0.024 and 0.31 nm^2/s were extracted at 1000 ^{o}C, 1100 ^{o}C and 1200 ^{o}C respectively. Neither diffusion nor loss of Eu was observed in the 350 ^{o}C implanted single crystalline 6H-SiC samples annealed at temperatures from 1000 ^{o}C to 1400 ^{o}C. Also, the Eu oxalate compound surface peak that was observed in the 350 ^{o}C implanted polycrystalline after annealing at 1000 ^{o}C, was not observed in the 350 ^{o}C implanted 6H-SiC sample. This difference is due to the fact that Eu is able to migrate via the grain boundaries and sit on the surface in the polycrystalline sample while this is not possible in the single crystalline 6H-SiC because of the absence of grain boundaries in the 6H-SiC sample.

Acknowledgements

I would like to acknowledge my supervisors; Prof TT Hlatshwayo and Prof JB Malherbe for supporting and guiding me throughout my research. I was always welcome to discuss any issues regarding my work. I would also like to thank all my fellow postgraduate students in Nuclear Materials Group and friends for their motivation and support.

I would also like to thank my family, my parents (Kelly and Malesela Mohlala) and my brothers for their trust in me, support and encouragement

The financial support from the University of Pretoria (UP) is hereby appreciated.

I thank God for nourishing my memory with his great news, promises and motivations, I thank him for keeping me away from life threatening situations and protecting me at all times.

Table of Contents

List of Figures

Figure 6.5: *SEM micrographs of SiC implanted with 270 keV Eu ions at RT before and after sequentially annealing: (a)the as-implanted sample, (b) annealed at 1000 ^{o}C, (c)annealed at 1100 ^{o}C, (d)annealed at 1200 ^{o}C, (e)annealed at 1300 ^{o}C and (f) annealed at 1400 ^{o}C.*

Figure 6.6: *SEM micrographs of SiC implanted with 270 keV Eu ions at 350 ^{o}C before and after isochronal annealing: (a) as-implanted sample, (b) 1000 ^{o}C annealed sample, (c) 1100 ^{o}C annealed sample, (d) 1200 ^{o}C annealed sample and (e) 1300 ^{o}C annealed sample and (f) 1400 ^{o}C.*

Figure 6.7: *SEM micrographs of SiC implanted with 270 keV Eu ions at 600 ^{o}C before and after isochronal annealing: (a) as-implanted sample, implanted then sequential annealed up to (b) 1000 ^{o}C, (c) 1100 ^{o}C, (d) 1200 ^{o}C and (e) 1300 ^{o}C and (f) 1400 ^{o}C.*

Figure 6.8: *Depth profiles of Eu implanted into SiC at (a) RT, (b) 350 and (c) 600 ^{o}C at 270 keV, and after isochronal annealing from 1000 to 1400 ^{o}C insteps of 100 ^{o}C for 5 hrs.*

Figure 6.9: *Graphs of (a)retained ratio of Eu implanted into SiC at RT, 350 and 600 ^{o}C after isochronal annealing at 1000 to 1400 ^{o}C for 5hrs in steps of 100 ^{o}C, (b) full width at half maximum as a function of annealing temperature of Eu implanted into SiC at RT, 350 and 600 ^{o}C after isochronal annealing at 1000 to 1400 ^{o}C for 5hrs in steps of 100 ^{o}C and (c)peak position as a function of annealing temperature of Eu implanted into SiC at RT, 350 and 600 ^{o}C after isochronal annealing at 1000 ^{o}C to 1400 ^{o}C for 5hrs in steps of 100 ^{o}C.*

Figure 6.10: *XPS survey spectra of SiC implanted with Eu and annealed at 1000 ^{o}C.*

Figure 6.11: High resolution *XPS spectra of SiC implanted with Eu and then annealed at 1000 ^{o}C for (a) Si2p peak, (b) C1s peaks and resolved peaks, (c) O1s peak and (d) Eu3d peaks.*

Figure 6.12: *Eu RBS depth profiles of the RT implanted samples (a) as-implanted sample and of (b) the sample vacuum-annealed at 1100 ^{o}C. The solid lines are least-square fits of a Gaussian function to the as-implanted data in (a) and of the Fick solution to only the surface half of the 1100^{o}Cannealed profile in (b).*

Figure 6.13: *Arrhenius plot of the diffusion coefficients of polycrystalline 3C-SiC implanted at room temperature with 270 keV europium ions and sequentially vacuum annealed for 5 h at 1000 ^{o}C, 1100 ^{o}C and 1200 ^{o}C.*

Figure 6.14: *The Eu depth profiles from RBS of Eu implanted into 6H-SiC at RT and 350 ^{o}C together with SRIM simulated Eu depth profile and displacement per atom (dpa).*

Figure 6.15: *Raman spectra of un-implanted single-crystalline 6H-SiC and 6H-SiC implanted with Eu ions at RT and 350 ^{o}C.*

Figure 6.16: *Raman spectra of un-implanted, (a) as-implanted and RT implanted then annealed at 1000 ^{o}C and 1400 ^{o}C (b) 350 ^{o}C implanted then annealed at 1000 ^{o}C and 1400 ^{o}C.*

Figure 6.17: *SEM micrographs of the (a) virgin/un-implanted 6H-SiC compared with the samples implanted with 270 keV Eu ions at (b) RT and (c) 350 ^{o}C.*

Figure 6.18: *SEM micrographs of 6H-SiC implanted with 270 keV Eu ions at RT before and after isochronal annealing, (a) the as-implanted sample, (b) annealed at 1000 ^{o}C, (c) annealed at 1100 ^{o}C, (d) annealed at 1200 ^{o}C, (e) annealed at 1300 ^{o}C and (f) annealed at 1400 ^{o}C.*

Figure 6.19: *SEM micrographs of 6H-SiC implanted with 270 keV Eu ions at 350 ^{o}C before and after annealing, (a) as-implanted sample, (b) 1000 ^{o}C annealed sample, (c) 1100 ^{o}C annealed sample, (d) 1200 ^{o}C annealed sample and (e) 1300 ^{o}C annealed sample and (f) 1400 ^{o}C.*

Figure 6.20: *Depth profiles of Eu (270 keV) implanted into 6H-SiC at RT and 350 ^{o}C, after isochronal annealing from 1000 ^{o}C to 1400 ^{o}C in steps of 100 ^{o}C for 5 hours.*

Figure 6.21: *(a) Retained ratios of Eu implanted into 6H-SiC at RT and 350 ^{o}C after isochronal annealing at 1000 to 1400 ^{o}C for 5 hours in steps of 100 ^{o}C, (b) peak shift as a function of annealing temperature and(c) full width at half maximum as a function of annealing temperature.*

Figure 6.22: *Eu RBS depth profiles of an as-implanted sample and of the sample vacuum-annealed at 1100 ^{o}C. The solid line is least-squares fit of a Gaussian function to the as-implanted data and the broken line is the Fick solution to the 1100 ^{o}C annealed data.*

Figure 6.23: *Arrhenius plot of the diffusion coefficients of 6H-SiC implanted at room temperature with 270 keV Eu ions and sequentially vacuum annealed for 5 h at 1000 ^{o}C, 1100 ^{o}C and 1200 ^{o}C, (error bars not included as the data points are all on the straight line).*

CHAPTER 1

INTRODUCTION

The need for a clean and sustainable source of energy has become a priority in the selection of the world energy generation sources. The renewable energy consumption has grown strongly recently in the energy mix, from 4.5% in 2018 to 5% in 2019 while nuclear energy consumption increased by 3.2%, which marked its fastest growth since 2004 [1]. These statistics show that the world is rapidly moving away from energy sources that impose a high health risk to the environment with the emission of greenhouse gases that contribute heavily in the atmospheric pollution. Modern nuclear energy systems are designed to provide a sustainable energy generation that meets clean-air objectives and provides long-term availability of systems and effective fuel utilization for worldwide energy production [2].

The high-temperature gas-cooled reactors (HTGRs) are series of reactor technologies considered in the Generation IV reactor designs. These reactors are guided by a number of goals, such as sustainability, economics, safety, reliability, proliferation resistance and physical protection. The very-high temperature reactor (VHTR) design is one of these reactor designs. A VHTR reactor has a core outlet temperature of > 900 ^{o}C. The ability of this reactor to reach such high temperatures makes it additionally useful for the production of hydrogen through thermo-chemical processes that require high temperatures. The technical basis for VHTR is its fuel particle, thus the tri-structural isotropic (TRISO) coated particle. Its potential for inherent safety, low operation and maintenance costs, high thermal efficiency, modular construction and process-heat-application capability makes it ideal in the progressive development of high temperature reactors (HTRs). The TRISO-coated fuel particle enables the VHTR in achieving high temperature and the retention of fission products (FPs) inside the coated particle during normal operation and accident conditions.

The Pebble Bed Modular Reactor (PBMR) design originated with the German high-temperature reactor (HTR) development programme [3], a small modular reactor that is helium cooled and graphite moderated. The PBMR project in South Africa PBMR Ltd (1999) was established with the intention of developing and marketing the reactor. The PBMR

employs a TRISO-coated fuel particle. The design of the fuel particle consists of a fuel kernel (UO_2) that is coated with a layer of graphite buffer, inner pyrolytic carbon (IPyC), silicon carbide (SiC) and finally an outer pyrolytic carbon (OPyC) - see Figure 1.1. The low density PyC layer (the buffer) attenuates fission recoils and also provides voids for gaseous FPs and carbon monoxide that are produced. The inner PyC retains gaseous FPs. The SiC layer serves as the main barrier to solid FPs and provides adequate structural stability during fuel compact fabrication. The outer-high density PyC protects SiC layer mechanically.

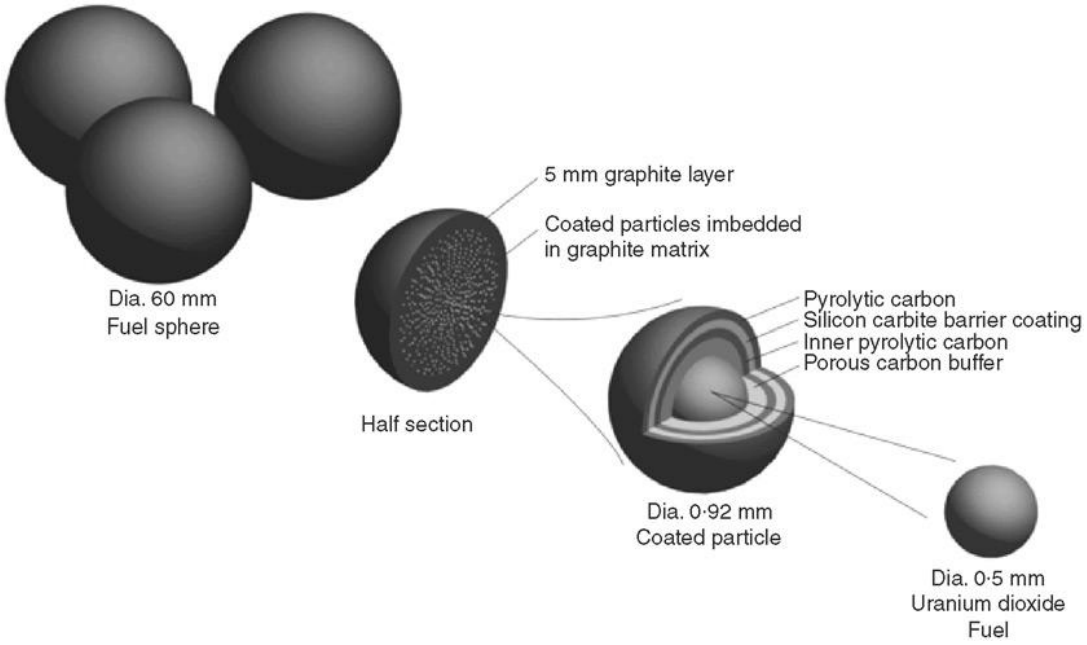

Figure 1.1: *A schematic diagram of a TRISO fuel particle. Taken from reference [3].*

Silicon carbide is a compound of silicon and carbon atoms and has a chemical formula SiC. The atoms in the compound are linked together by a covalent bonding. Due to the strong nature of the covalent bonding in this material, SiC has a high melting point of about 2700 ^{o}C [4, 5]. It is also a hard substance due to the difficulty in breaking the covalent lattice. The arrangement of the atoms is such that two primary coordination tetrahedral where four carbon (C) atoms are bonded to a central silicon (Si) atom or four Si atoms are bonded to a central C atom see Figure 1.2.

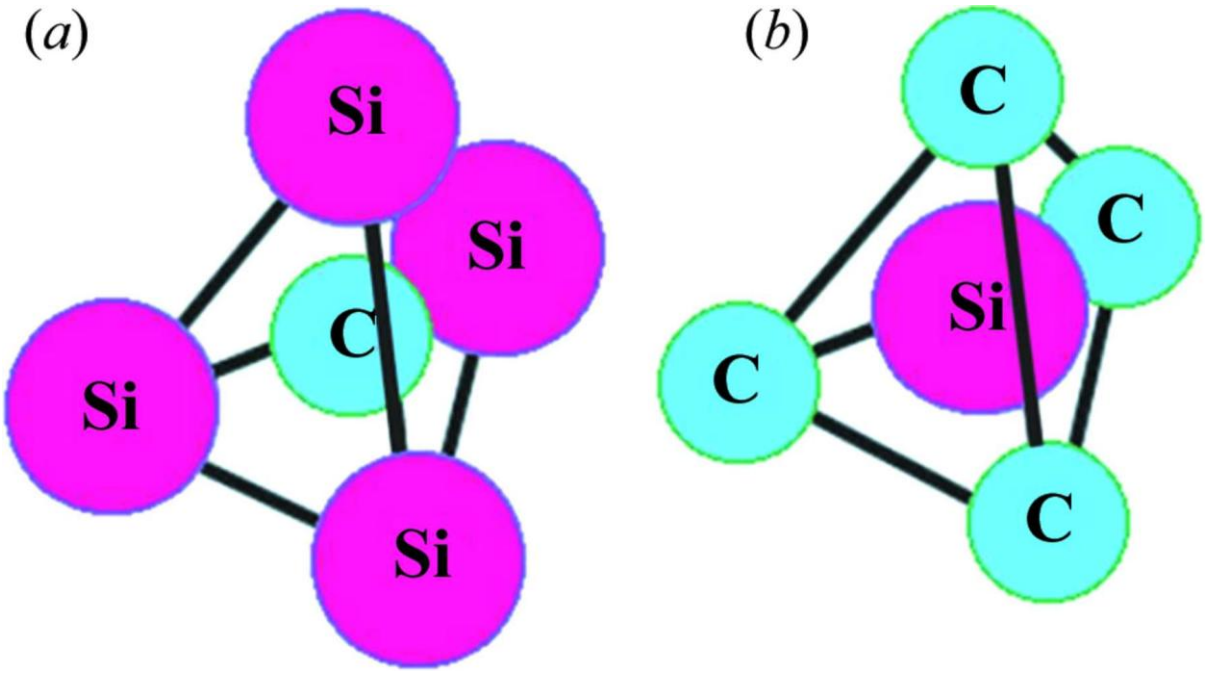

Figure 1.2: *Tetrahedral crystal structure representation of (a) Si_4C tetrahedron and (b) C_4Si tetrahedron. Taken from reference [6].*

SiC derives its outstanding variety of properties from its very high Si-C bond energy (4.6 eV) [7]. The tetrahedral unit cells are connected through their corners and stacked together to form polar structures called polytypes. Polytypism is the phenomenon where a material can adopt different crystal structures that vary in stacking sequence without changes in chemical composition. The well-known example of polytypism material is in SiC [8-12]. SiC has more than 200 polytypes. Figure 1.3. presents popular polytypes of SiC structures. The black and white circles denote C and Si atoms respectively. The hexagonal and cubic sites are indicated by h and k respectively.

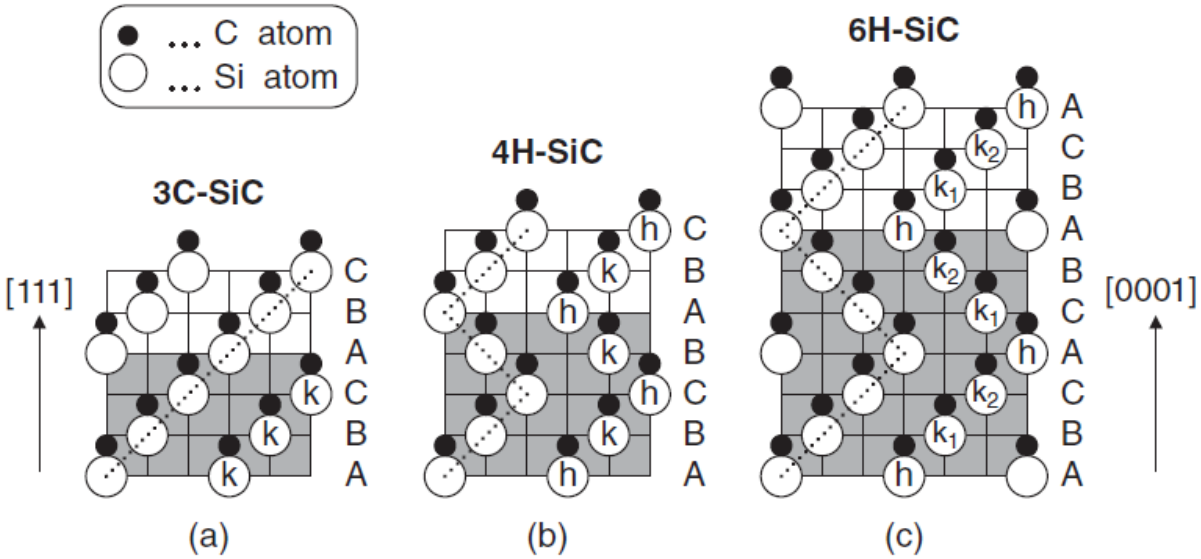

Figure 1.3: *Schematic structures of popular SiC polytypes; (a) 3C-SiC, (b) 4H-SiC, and (c) 6H-SiC. Taken from reference [7].*

Figure 1.4. shows a schematic representation of sites in a cubic close-packed system. The three possible sites are denoted as A, B, and C. No two successive layers are allowed to occupy the same site, e.g. the layer on top of an A layer must occupy either B or C sites, and consequently A or C is allowed over B.

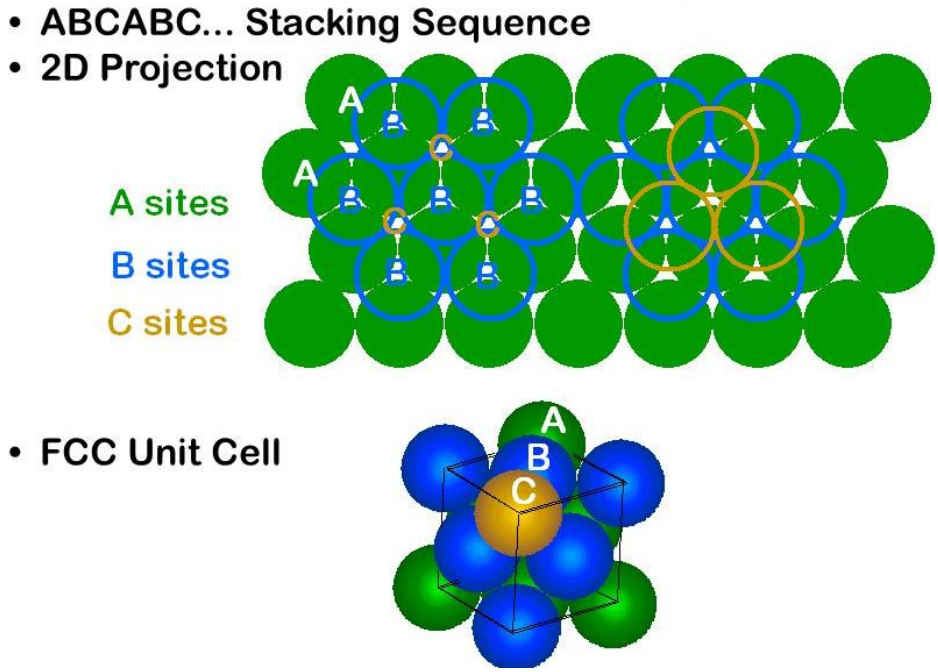

Figure 1.4: *Occupation sites (A, B, and C) in the cubic close-packed system. Taken from reference [13].*

The major SiC polytypes are described using Ramsdell's notation: C for cubic, H for hexagonal, and R for rhombohedral [14]. The 3C-SiC is normally referred to as β-SiC and hexagonal is generally known as α-SiC. The stacking sites make it possible to describe the polytypes by a repeating sequence, thus 3C-SiC can be described by the sequence ABCABC or just ABC, while 4H and 6H-SiC can be described by ABCB and ABCACB respectively. The 3C structure is often called the zincblende while the hexagonal one is known as wurtzite [15].

In a nuclear fuel coating, SiC is used due to its outstanding mechanical and thermal properties such as high thermal conductivity, high radiation resistance and low absorption neutron cross-section. SiC is one of the hardest materials with Moh's hardness of 9.0 and Young's modulus ranging between 300-700 GPa [16]. There is little polytype dependence in the major mechanical properties reported in the literature [17, 18]. For the successful use of SiC in a nuclear reactor, it has to retain its superior properties during reactor operational and accidental conditions.

1.1 Radiation damage in SiC

In nuclear reactor environment SiC will be exposed to different irradiations at elevated temperatures. Under these conditions, SiC should be able to act as the main barrier to fission products. Hence, extensive investigations have been performed on the irradiation behaviour of SiC.

Irradiation of SiC with energetic ions affect the structure and physical properties of SiC. It was revealed a few decades ago, that atoms could be displaced by high energy neutrons, from their equilibrium positions in a crystal lattice [19]. The effects of bombardment of SiC with particles of light to heavy mass of high energies have been at the center of scientific research field ever since. Many results have been reported on the formation of simple point defects in materials [20 - 26]. The study of the relationship between the point defects and the properties of the materials has become important in various fields of applications. The initial studies of the effect of irradiation of neutrons and α-particles on SiC indicated that SiC can be used as a high-temperature radiation-resistant material [27 - 30]. Moreover, early studies on the irradiation of SiC found that irradiation with high-energy electrons (in excess of 1 MeV) into various SiC polytypes exhibited isolated silicon vacancies or negatively charged silicon vacancies as the main radiation defects, which could be more beneficial in the semiconductor

applications [31 - 33]. In irradiation with electrons, the SiC amorphization threshold fluence was found to be 10^{22} - 10^{23} cm^{-2} [34].

Measurements of irradiation with electrons with energies of 1 - 2.5 MeV to fluences of 10^{17} - 10^{18} cm^{-2} into high-purity epitaxial layers of n-3C- , n-6H- , and n-4H-SiC, revealed that, after heat treatment, partial annealing of silicon vacancies (V_{si}) was taking place at 200 ^{o}C [35]. A complete annealing took place at temperatures of 750 - 900 ^{o}C for the V_{Si} vacancy centers, and the complexes that involved these vacancies were annealed out at temperatures of 1200 - 1400 ^{o}C [36 - 38]. Irradiation of the chemical vapour deposited (CVD) layers of 3C- , 4H- , and 6H-SiC polytypes with electrons of energies 0.5 - 2 MeV and fluences of 3×10^{17} - 6×10^{17} cm^{-2} and the annealing of these samples at elevated temperatures up to 1700 ^{o}C in vacuum, indicated the formation of complex defects at different temperatures for different polytypes. It was observed that the annealing temperature increased with the increase in the degree of hexagonality of SiC, from 3C- , through to 4H polytypes [39]. Irradiation with low-energy electrons revealed a variety of configurations and charge states of radiation defects. Irradiation with electrons of different energies from 300 - 900 keV and fluences from 5×10^{17}- 3×10^{19} cm^{-2} into 3C- , 4H- , and 6H-SiC of both n- and p-type, produced Frenkel pairs of the form: $V_{Si}^{3-} - Si_i$ (silicon vacancy and silicon interstitial pair) [40, 41]. The vacancy defects found in the p-SiC samples were observed to be annealed out at low temperatures as compared to similar defects found in the n-SiC samples.

The distribution of the radiation defects induced when irradiating SiC with neutrons of energies ranging between 0 and 15 MeV is uniform over the bulk of the sample [42]. Approximately 90% of the defects formed by irradiation with neutrons in 3C-SiC were observed to be annealed out at 350 ^{o}C [43]. Studies with Electron Spin Resonance (ESR) done at 77K on the n- and p-4H- and 6H-SiC samples irradiated with >0.1 MeV electrons at a fluence of 6×10^{16} cm^{-2} revealed a broad area of defect-related centers in different charge states [44, 45]. These defects were identified with various defect configurations and were annealed out at different temperatures ranging from 800 to 1500 ^{o}C.

It was found that the behaviour of the defects in SiC for the samples irradiated with electrons and those irradiated with neutrons are identical [46]. They were found to become more larger and more complex with an increase of the irradiation fluence (e.g 10^{20} - 10^{21} cm^{-2}) [47].

Irradiation with ions is also commonly used, to study the radiation-induced defects formation. When the irradiating ions collide with the atoms of a solid material, energy is transferred to the atoms in a solid. Depending on the amount of energy transferred, the interatomic bonding between the atoms in a solid can be broken, resulting in permanently displaced atom from its lattice site [48]. The amount of energy that is required to permanently displace an atom from its lattice position is known as the displacement energy. In SiC, the displacement energies are 35 and 20 eV for Si and C atoms respectively [49].

Irradiation with ions at room temperature is known to easily amorphize SiC even at low energies in the order of a few hundred keV, irrespective of ion type implanted [50, 51]. The critical damage energy for α-SiC was found to range from 16 to 20 eV/atom and that of β-SiC was around 25 eV/atom [50]. Furthermore, they found that radiation damage increased with increasing fluence until amorphization occurs. It was also reported by Zinkle et al. that SiC is easily amorphized at room temperature after damage levels of 0.4 displacements per atom (dpa) [52]. McHargue et al. found that implantation at 500 ^{o}C and above, does not produce an amorphous layer for damage levels up to 17 dpa [50].

A wide range of defects and imperfections are formed near the surface when irradiating SiC with ions of low energies. It was indicated that the defects introduced into SiC by implantation of medium mass ions (e.g. Al, Ge, Ar, N, Ag, I) are vacancies, divacancies, and complexes of vacancies [53, 54, 55]. These defects decrease with increasing temperature of irradiation as a result of increased rate of recombination of atoms with vacancies [56, 57]. Investigations by Wesch et al. showed that amorphization is reached by implantation of 230 keV Ga^{+} ions into SiC at 80 K with fluences above 1×10^{14} cm^{-2}, for implantation at 300 K, amorphization was reached for fluences ranging from 2×10^{14} to 3×10^{14} cm^{-2}. However, it was also found in the same study that implantation at around 573 K with fluences of up to 1×10^{16} cm^{-2} does not amorphize SiC [51].

In a study by Carlsson et al, the n-4H- and n-6H-SiC samples were irradiated at temperatures ranging from 25 to 600 ^{o}C with C and Si ions with energies of 110 and 200 keV respectively [58]. A projected range of 200 nm and fluences of 1.4×10^{13} and 4.3×10^{12} cm^{-2} for C and Si ions were achieved. As a result of irradiation at high temperatures, defects were higher in the samples irradiated with C ions because of the increased mobility of these atoms due to heating of the samples [58, 59]. McHargue et al. found that for low damage (without

amorphization) in SiC, the damage annealed out in a temperature range of 200 to 1000 ^{o}C [50]. However, for the amorphous layer, they found that regrowth was not clear and the damage annealed in the temperature range of 750 to 1700 ^{o}C. Slotte et al confirmed with RBS/C and positron annihilation spectroscopy (PAS) that the amount of defects in SiC decreased as the temperature of irradiation increased [60, 61].

Our group at the University of Pretoria had been constantly involved in the study of radiation damage in SiC caused by irradiation by fission products in a nuclear fuel particle. Friedland et al implanted different ions (Cs, Ag, Sr and I) with energy 360 keV into 6H-SiC at room temperature with fluences of 1×10^{16} cm^{-2} for cesium and iodine, and 2×10^{16} cm^{-2} for silver and strontium, all of which resulted in amorphous layers [62, 63, 64, 65]. An epitaxial regrowth in the amorphous layer was observed after annealing the samples at temperatures up to 1200 ^{o}C. Recent studies in our group performed implantations of 360 keV Ag and Sr ions to fluences 2×10^{16} cm^{-2} into 3C-SiC wafers to a projected range of around 140 nm and another study implanted 200 keV selenium ions to a fluence of 1×10^{16} cm^{-2} into 3C-SiC [66, 67, 68]. All these implantations at room temperature resulted in the amorphization of SiC. Annealing of the samples was performed in a temperature range of 1100 - 1500 ^{o}C and 1000 - 1500 ^{o}C for silver, strontium and for selenium, respectively. In both cases, the annealing out of the radiation damage was observed after the first annealing cycle.

1.2 Motivation for the study

Several studies have been conducted with the common aim of understanding the migration behaviour of FPs in SiC. To simulate the reactor conditions ion implantation was used, mostly to address the issue of limited solubility of FPs in SiC and for the study of radiation damage enhanced diffusion [50, 69]. Unlike the time-consuming neutron experiments in the hustle to collect data from reactor core [70], ion irradiation experiments offer more flexibility in processing. More controllable fluences can be obtained much faster, the profiles can be tailored and is not restricted to error function [71].

Due to concerns around the possible radiological hazards under accident conditions and in the plate-out activity of the primary circuit, studies have been done on the release behaviour of FPs from fuels of high temperature gas-cooled reactors (HTGR) [72, 73]. The studies by International Atomic Energy Agency (IAEA) revealed that several FPs are able to escape the

fuel particle through intact SiC [74]. For instance, the fission products such as Ag, Cs, palladium (Pd) and Eu have proven to easily penetrate the SiC layer during operation [74-79]. Thorough studies have been done on the transportation mechanism of Ag through SiC [63, 80 - 84]. Limited information is available on the migration behaviour of Cs, Eu and Sr [75, 62, 67, 85-86]. Ag, Cs, Eu and Sr are known FPs released in measurable quantities with radiological health concerns [87, 88]. To get more insight in the migration of these FPs in SiC the effect of radiation damage need to be understood since SiC is continuously exposed to different irradiations with varying energies during operation of nuclear reactors. That can result in a damaged SiC, which as a result, can play a role in enhancing the migration of FPs.

Not much has been reported in the role of radiation damage in the migration behaviour of Eu in SiC. In the current study, implantation of 270 keV Eu ions was performed on single crystalline (6H) and polycrystalline SiC wafers at different temperatures to investigate the influence of radiation damage in the migration behaviour of implanted Eu. The SiC used in a fuel reactor is a chemical vapour deposited 3C. In this study, implantation of Eu was performed on both the single crystallline 6H- and polycrystalline SiC at various implantation temperatures to investigate the role of radiation damage in the migration of Eu.

References

[1] Bp.com. 2020. *Statistical review of world energy*. [online] Available at: <https://www.bp.com/content/dam/bp/business-sites/en/global/corporate/pdfs/energy-economics/statistical-review/bp-stats-review-2020-full-report.pdf> [Accessed 16 July 2020].

[2] Pioro, I. and Duffey, R., 2019. Current and future nuclear power reactors and plants. In: T. Letcher, ed., *Managing Global Warming: An Interface of Technology and Human*. Elsevier Inc., pp.117-197.

[3] Ion, S., Nicholls, D., Matzie, R. and Matzner, D. (2004). Pebble bed modular reactor? the first Generation IV reactor to be constructed. *Nuclear Energy*, 43(1), pp.55-62.

[4] BYJUS. 2020. *Silicon carbide - structure, properties, and uses of SiC*. [online] Available at: <https://byjus.com/chemistry/silicon-carbide/> [Accessed 20 July 2020].

[5] Webcache.googleusercontent.com. 2020. *Compounds and bonding*. [online] Available at: <https://webcache.googleusercontent.com/search?q=cache:qP8UxUhX8RsJ:https://www.sserc.org.uk/wp-content/uploads/2012/09/Unit-1-Bonding-compounds-intera.ppt+&cd=1&hl=en&ct=clnk&gl=za&client=firefox-b-d> [Accessed 20 July 2020].

[6] Ortiz, A., Sánchez-Bajo, F., Cumbrera, F. and Guiberteau, F., 2013. The prolific polytypism of silicon carbide. *Journal of Applied Crystallography*, 46(1), pp.242-247.

[7] Kimoto, T. and Cooper, J., 2014. *Fundamentals of silicon carbide technology*. 1st ed. Singapore: John Wiley & Sons, Incorporated.

[8] Cheng, C., Needs, R.J. and Heine, V. (1988) Inter-layer interactions and the origin of SiC polytpes. *Journal of Physics. C*, 21, 1049.

[9] Fisher, G.R. and Barnes, P. (1990) Towards a unified view of polytypism in silicon carbide. *Philosophical Magazine. B*, 61, 217.

[10] Verma, A.R. and Krishna, P. (eds) (1966) *Polymorphism and polytypism in crystals*, John Wiley & Sons, Inc., New York.

[11] Denteneer, P.J.H. and van Haeringen,W. (1986) Ground-state properties of polytypes of silicon carbide. *Physical Review. B*, 33, 2831.

[12] Schneer, C.S. (1955) Polymorphism in one dimension. *Acta Crystallogr.*, 8, 279.

[13] Slideplayer.com. 2020. *Chapter 3: Crystal structures & properties - ppt Video Online Download*. [online] Available at: <https://slideplayer.com/slide/3866443/> [Accessed 22 July 2020].

[14] Callaway, B., 2016. [online] Mrl.ucsb.edu. Available at: <https://www.mrl.ucsb.edu/~seshadri/2016_286G/Callaway.pdf> [Accessed 22 July 2020].

[15] Chemistry LibreTexts. 2019. *6.11E: Structure - Zinc Blende (Zns)*. [online] Available at: <https://chem.libretexts.org/Bookshelves/Inorganic_Chemistry/Map%3A_Inorganic_Chemistry_(Housecroft)/06%3A_Structures_and_energetics_of_metallic_and_ionic_solids/6.11%3A_Ionic_Lattices/6.11E%3A_Structure_-_Zinc_Blende_(ZnS)> [Accessed 22 July 2020].

[16] Zorman, C.A. and Parro, R.J. (2008) Micro- and nanomechanical structures for silicon carbide MEMS and NEMS. *Physoca Status Solidi B*, 245, 1404.

[17] Harris, G.L. (1995) *Properties of silicon carbide*, INSPEC.

[18] Adachi, S. (2005) *Properties of group-IV, III-V, and II-VI semiconductors*, JohnWiley&Sons, Ltd, Chichester.

[19] Wigner, E., 1946. Theoretical physics in the metallurgical laboratory of chicago. *Journal of Applied Physics*, 17(11), pp.857-863.

[20] Seitz, F., 1949. On the disordering of solids by action of fast massive particles. *Discussions of the Faraday Society*, 5, p.271.

[21] Keywell, F., 1955. Measurements and collision—radiation damage theory of high-vacuum sputtering. *Physical Review*, 97(6), pp.1611-1619.

[22] Kinchin, G. and Pease, R., 1955. The displacement of atoms in solids by radiation. *Reports on Progress in Physics*, 18(1), pp.1-51.

[23] Harrison, D., 1956. Theory of the sputtering process. *Physical Review*, 102(6), pp.1473-1480.

[24] Bohr, N., *The penetration of atomic particles through matter*, 3rd ed. (Munksgaard, Copenhagen, 1960; Inostrannaya Literatura, Moscow, 1960).

[25] Dienes, G. and Vineyard, G., 1957. *Radiation effects in solids*. Interscience: New York.

[26] Vavilov, V. and Ukhin, N., 1973. *Radiation effects in semiconductors and in semiconductor instruments. Part II*. Ft. Belvoir: Defense Technical Information Center.

[27] O'Connor, J. and Smiltens, J., 1960. *Silicon carbide : a high temperature semiconductor : proceedings of the conference on silicon carbide boston, mass., april 2-3, 1959*. oxford (u. a.): pergamon press.

[28] Babcock, R. and Chang, H., 1963. *Absolute measurement of neutron fluxes inside the reactor core*. [online] Inis.iaea.org. Available at: <https://inis.iaea.org/collection/NCLCollectionStore/_Public/41/124/41124426.pdf> [Accessed 11 October 2020].

[29] Canepa, P., Malinaric, P., Campbell, R. and Ostroski, J., 1964. High temperature nuclear particle detector. *IEEE Transactions on Nuclear Science*, 11(3), pp.262-270.

[30] Madelung, O., n.d. *Semiconductors: Data Handbook*.

[31] Singh, N. and Prabha Singh, S., 1987. Lattice defects and the effect of Melment on the hydration of alite. *Journal of Materials Science*, 22(8), pp.2751-2758.

[32] Schneider, J. and Maier, K., 1993. Point defects in silicon carbide. *Physica B: Condensed Matter*, 185(1-4), pp.199-206.

[33] Kalinina, E., 2007. The effect of irradiation on the properties of SiC and devices based on this compound. *Semiconductors*, 41(7), pp.745-783.

[34] Inui, H., Mori, H. and Fujita, H., 1990. Electron-irradiation-induced crystalline to amorphous transition in α-Sic single crystals. *Philosophical Magazine B*, 61(1), pp.107-124.

[35] Kawasuso, A., Itoh, H., Cha, D. and Okada, S., 1998. Characterization of defects in electron irradiated 6H-SiC by positron lifetime and electron spin resonance. *Materials Science Forum*, 264-268, pp.611-614.

[36] Kawasuso, A., Redmann, F., Krause-Rehberg, R., Yoshikawa, M., Kojima, K. and Itoh, H., 2001. Positron annihilation due to silicon vacancies in 3C and 6H SiC epitaxial layers induced by 1 MeV electron irradiation. *physica status solidi (b)*, 223(2), p.R8.

[37] Staab, T., Torpo, L., Puska, M. and Nieminen, R., 2001. Calculated positron annihilation parameters for defects in SiC. *Materials Science Forum*, 353-356, pp.533-536.

[38] Kawasuso, A., Redmann, F., Krause-Rehberg, R., Weidner, M., Frank, T., Pensl, G., Sperr, P., Triftshäuser, W. and Itoh, H., 2001. Annealing behavior of vacancies and Z1/2 levels in electron-irradiated 4H–SiC studied by positron annihilation and deep-level transient spectroscopy. *Applied Physics Letters*, 79(24), pp.3950-3952.

[39] Kawasuso, A., Yoshikawa, M., Maekawa, M., Itoh, H., Chiba, T., Redmann, F., Krause-Rehberg, R., Weidner, M., Frank, T. and Pensl, G., 2003. Polytype-dependent vacancy annealing studied by positron annihilation. *Materials Science Forum*, 433-436, pp.477-480.

[40] von Bardeleben, H., Cantin, J., Henry, L. and Barthe, M., 2000. Vacancy defects inp-type6H−SiCcreated by low-energy electron irradiation. *Physical Review B*, 62(16), pp.10841-10846.

[41] von Bardeleben, H. and Cantin, J., 2001. Electron irradiation induced defects in monocrystalline 4H–SiC and 6H–SiC: the influence of the electron energy and doping. *Applied Surface Science*, 184(1-4), pp.237-241.

[42] Watt, B., 1952. Energy spectrum of neutrons from thermal fission of U235. *Physical Review*, 87(6), pp.1037-1041.

[43] Nagesh, V., Farmer, J., Davis, R. and Kong, H., 1987. Defects in neutron irradiated SiC. *Applied Physics Letters*, 50(17), pp.1138-1140.

[44] Kanazawa, S., Okada, M., Nozaki, T., Shin, K., Ishihara, S. and Kimura, I., 2002. Radiation-induced defects in p-type silicon carbide. *Materials Science Forum*, 389-393, pp.521-524.

[45] Kanazawa, S., Kimura, I., Okada, M., Nozaki, T., Kanno, I., Ishihara, S. and Watanabe, M., 2000. Electron spin resonance in neutron-irradiated n-type 6H-silicon carbide. *Materials Science Forum*, 338-342, pp.825-830.

[46] Orlinski, S., Schmidt, J., Mokhov, E. and Baranov, P., 2003. Silicon and carbon A high-field electron paramagnetic vacancies in neutron-irradiated SiC: resonance study. *Physical Review B*, 67(12).

[47] Ilyin, I., Muzafarova, M., Mokhov, E., Baranov, P., Orlinskii, S. and Schmidt, J., 2003. Multivacancy clusters in silicon carbide. *Physica B: Condensed Matter*, 340-342, pp.128-131.

[48] Kinchin, G. and Pease, R., 1955. The displacement of atoms in solids by radiation. *Reports on Progress in Physics*, 18(1), pp.1-51.

[49] Devanathan, R., Weber, W. and Gao, F., 2001. Atomic scale simulation of defect production in irradiated 3C-SiC. *Journal of Applied Physics*, 90(5), pp.2303-2309.

[50] McHargue, C. J. and Williams, J. M., 1993. Ion implantation effects in silicon carbide. *Nuclear Instruments and Methods in Physics Research Section B: Beam Interactions with Materials and Atoms*, 80–81(Part 2), pp.889-894.

[51] Wendler, E., Heft, A. and Wesch, W., 1998. Ion-beam induced damage and annealing behaviour in SiC. *Nuclear Instruments and Methods in Physics Research Section B: Beam Interactions with Materials and Atoms*, 141(1-4), pp.105-117.

[52] Zinkle, S. and Snead, L., 1996. Influence of irradiation spectrum and implanted ions on the amorphization of ceramics. *Nuclear Instruments and Methods in Physics Research Section B: Beam Interactions with Materials and Atoms*, 116(1-4), pp.92-101.

[53] Pensl, G. and Choyke, W., 1993. Electrical and optical characterization of SiC. *Physica B: Condensed Matter*, 185(1-4), pp.264-283.

[54] Patrick, L. and Choyke, W., 1972. Photoluminescence of radiation defects in ion-implanted 6H-SiC. *Physical Review B*, 5(8), pp.3253-3259.

[55] Uedono, A., Itoh, H., Ohshima, T., Suzuki, R., Ohdaira, T., Tanigawa, S., Aoki, Y., Yoshikawa, M., Nashiyama, I., Mikado, T., Okumura, H. and Yoshida, S., 1997. Annealing properties of defects in ion-implanted 3C-SiC studied using monoenergetic positron beams. *Japanese Journal of Applied Physics*, 36(Part 1, No. 11), pp.6650-6660.

[56] Wirth, H., Anwand, W., Brauer, G., Voelskow, M., Panknin, D., Skorupa, W. and Coleman, P., 1998. Investigation of ion-impantation induced damage in 6H-SiC by RSB/C and PAS. *Materials Science Forum*, 264-268, pp.729-732.

[57] Anwand, W., Brauer, G., Coleman, P., Voelskow, M. and Skorupa, W., 1999. Characterisation of defects in ion implanted SiC by slow positron implantation spectroscopy and Rutherford backscattering. *Applied Surface Science*, 149(1-4), pp.148-150.

[58] Carlsson, F., Sridhara, S., Hallén, A., Bergman, P. and Janzén, E., 2003. Dll PL Intensity dependence on dose, implantation temperature and implanted species in 4H- and 6H-SiC. *Materials Science Forum*, 433-436, pp.345-348.

[59] Sridhara, S., Nizhner, D., Devaty, R., Choyke, W., Dalibor, T., Pensl, G. and Kimoto, T., 1998. DII Revisited in an modern guise - 6H and 4H SiC. *Materials Science Forum*, 264-268, pp.493-496.

[60] Slotte, J., Saarinen, K., Janson, M., Hallén, A., Kuznetsov, A., Svensson, B., Wong-Leung, J. and Jagadish, C., 2005. Fluence, flux, and implantation temperature

dependence of ion-implantation-induced defect production in 4H–SiC. *Journal of Applied Physics*, 97(3), p.033513.

[61] Slotte, J., Saarinen, K., Kuznetsov, A. and Hallén, A., 2001. Vacancy type defects in Al implanted 4H–SiC studied by positron annihilation spectroscopy. *Physica B: Condensed Matter*, 308-310, pp.664-667.

[62] Friedland, E., van der Berg, N. G, Hlatshwayo, T. T, Kuhudzai, R. J, Malherbe, J. B, Wendler, E. and Wesch, W., 2012. Diffusion behaviour of cesium in silicon carbide at T > 1000 °C. *Nuclear Instruments and Methods in Physics Research B*, 286, pp.102–107

[63] Friedland, E., Malherbe, J. B., van der Berg, N. G., Hlatshwayo, T. T., Botha, A. J., Wendler, E. and Wesch, W. (2009). Study of silver diffusion in silicon carbide. *Journal of Nuclear Materials*, 389(2), pp.326-331.

[64] Friedland, E., van der Berg, N., Malherbe, J., Wendler, E. and Wesch, W., 2012. Influence of radiation damage on strontium and iodine diffusion in silicon carbide. *Journal of Nuclear Materials*, 425(1-3), pp.205-210.

[65] Friedland, E., van der Berg, N., Malherbe, J., Kuhudzai, R., Botha, A., Wendler, E. and Wesch, W., 2010. Study of iodine diffusion in silicon carbide. *Nuclear Instruments and Methods in Physics Research Section B: Beam Interactions with Materials and Atoms*, 268(19), pp.2892-2896.

[66] Abdelbagi, H. A., Skuratov, V. A., Motloung, S. V., Njoroge, E. G., Mlambo, M., Malherbe, J. B., O'Connell, J. H. and Hlatshwayo, T. T., 2019. Effect of swift heavy ions irradiation in the migration of silver implanted into polycrystalline SiC. *Nuclear Instruments and Methods in Physics Research Section B: Beam Interactions with Materials and Atoms*, 461, pp.201-209.

[67] Abdelbagi, H., Skuratov, V., Motloung, S., Njoroge, E., Mlambo, M., Hlatshwayo, T. and Malherbe, J., 2019. Effect of swift heavy ions irradiation on the migration behavior of strontium implanted into polycrystalline SiC. *Nuclear Instruments and Methods in Physics Research Section B: Beam Interactions with Materials and Atoms*, 451, pp.113-121.

[68] Abdalla, Z., Ismail, M., Njoroge, E., Hlatshwayo, T., Wendler, E. and Malherbe, J., 2020. Migration behaviour of selenium implanted into polycrystalline 3C–SiC. *Vacuum*, 175, p.109235.

[69] Ivanov, A. and Rusinkevich, A., 2014. Kinetics of silver release from microfuel with taking into account the limited-solubility effect. *Physics of Atomic Nuclei*, 77(14), pp.1677-1684.

[70] Was, G., 2007. Fundamentals of radiations materials science: *Metals And Alloys*. 1st ed. Berlin: Springer.

[71] Tuttle.merc.iastate.edu. 2020. [online] Available at: <http://tuttle.merc.iastate.edu/ee432/topics/doping/ion_implant.pdf> [Accessed 23 July 2020].

[72] Smith, P., Steinke, R., Jensen, D. and Hama, T., 1977. Release of metallic fission products from multilayered coated particles. *Nuclear Technology*, 35(2), pp.475-482.

[73] Hayashi, K., Kobayashi, F., Minato, K., Ikawa, K. and Fukuda, K., 1987. In-pile release behavior of metallic fission products in graphite materials of an htgr fuel assembly. *Journal of Nuclear Materials*, 149(1), pp.57-68.

[74] Inis.iaea.org. (2018). [online] Available at: https://inis.iaea.org/collection/NCLCollectionStore/_Public/29/009/29009817.pdf [Accessed 3 Dec. 2018].

[75] Dwaraknath, S. and Was, G. (2016). Radiation enhanced diffusion of cesium, strontium, and europium in silicon carbide. *Journal of Nuclear Materials*, 474, pp.76-87.

[76] Stempien, J., Demkowicz, P., Reber, E. and Christensen, C., 2016. High-temperature safety testing of irradiated agr-1 triso fuel. In: *2016 International Topical Meeting on High Temperature Reactor Technology (HTR2016)*. Idaho: Idaho National Laboratory.

[77] Hunn, J., Baldwin, C., Gerczak, T., Montgomery, F., Morris, R., Silva, C., Demkowicz, P., Harp, J. and Ploger, S., 2014. Detection and analysis of particles with failed SiC in AGR-1 fuel compacts. Weihai: Idaho National Laboratory.

[78] Collin, B., Petti, D., Demkowicz, P. and Maki, J., 2015. Comparison of silver, cesium, and strontium release predictions using PARFUME with results from the AGR-1 irradiation experiment. *Journal of Nuclear Materials*, 466, pp.426-442.

[79] Tiegs, T., 1982. Fission Product Pd-SiC Interaction in irradiated coated-particle fuels. *Nuclear Technology*, 57(3), pp.389-398.

[80] Ko, H., Deng, J., Szlufarska, I. and Morgan, D. (2016). Ag diffusion in SiC high-energy grain boundaries: Kinetic Monte Carlo study with first-principle calculations. *Computational Materials Science*, 121, pp.248-257.

[81] Kim, B., Yeo, S., Lee, Y. and Cho, M. (2015). Comparison of diffusion coefficients and activation energies for Ag diffusion in silicon carbide. *Nuclear Engineering and Technology*, 47(5), pp.608-616.

[82] Rabone, J., López-Honorato, E. and Van Uffelen, P. (2014). Silver and Cesium diffusion dynamics at the β-SiC Σ5 grain boundary investigated with density functional theory molecular dynamics and metadynamics. *The Journal of Physical Chemistry A*, 118(5), pp.915-926.

[83] López-Honorato, E., Zhang, H., Yang, D. and Xiao, P. (2011). Silver diffusion in silicon carbide coatings. *Journal of the American Ceramic Society*, 94(9), pp.3064-3071.

[84] Hlatshwayo, T. T., Mtshonisi, N., Njoroge, E. G., Mlambo, M., Msimanga, M., Skuratov, V. A., O'Connell, J. H., Malherbe, J. B. and Motloung, S. V., 2020. Effects of Ag and Sr dual ions implanted into SiC. *Nuclear Instruments and Methods in Physics Research Section B: Beam Interactions with Materials and Atoms*, 472, pp.7-13.

[85] Dwaraknath, S. and Was, G. (2016). The diffusion of cesium, strontium, and europium in silicon carbide. *Journal of Nuclear Materials*, 476, pp.155-167.

[86] Mohlala, T. M., Hlatshwayo, T. T., Mlambo, M., Njoroge, E. G.,Motloung, S. V. and Malherbe, J. B. (2017). Migration behaviour of Europium implanted into single crystalline 6H-SiC. *Vacuum*, 141, pp.130-134.)

[87] Nwmissouri.edu. (2020). [online] Available at: https://www.nwmissouri.edu/naturalsciences/sds/s/Silver%20Wire.pdf [Accessed 27 Feb. 2020].

[88] Petti, D., Buongiorno, J., Maki, J., Hobbins, R. and Miller, G., 2003. Key differences in the fabrication, irradiation and high temperature accident testing of US and German TRISO-coated particle fuel, and their implications on fuel performance. *Nuclear Engineering and Design*, 222(2-3), pp.281-297.

CHAPTER 2

DIFFUSION

In this study, the migration behaviour of Eu implanted into polycrystalline SiC and single-crystalline 6H-SiC was investigated. Implanted Eu might migrate via diffusion in SiC. Therefore, this chapter discusses the diffusion processes taking place in both polycrystalline SiC and 6H-SiC materials.

Diffusion is a phenomenon in which atoms in a material move from regions of high concentration to regions with low concentration, until equal concentration is reached throughout the material. Diffusion in solids occur due to thermally activated random movement of atoms. For diffusion to occur, the atoms must have enough energy to overcome energy barriers to atomic motion. This energy is normally sourced from thermal energy i.e. increasing the temperature. Radiation can also affect diffusion by introducing additional defects which enhance the diffusion of atoms. In solid materials, atoms vibrate continuously about their lattice positions. An atom must have sufficient energy to break the bonds that connect it with its neighbouring atoms in order for it to change position. Figure 2.1 shows interdiffusion in a material. Atoms of type A and type B are on the left and right respectively. After diffusion has taken place, atoms of one type had moved from one side to the other.

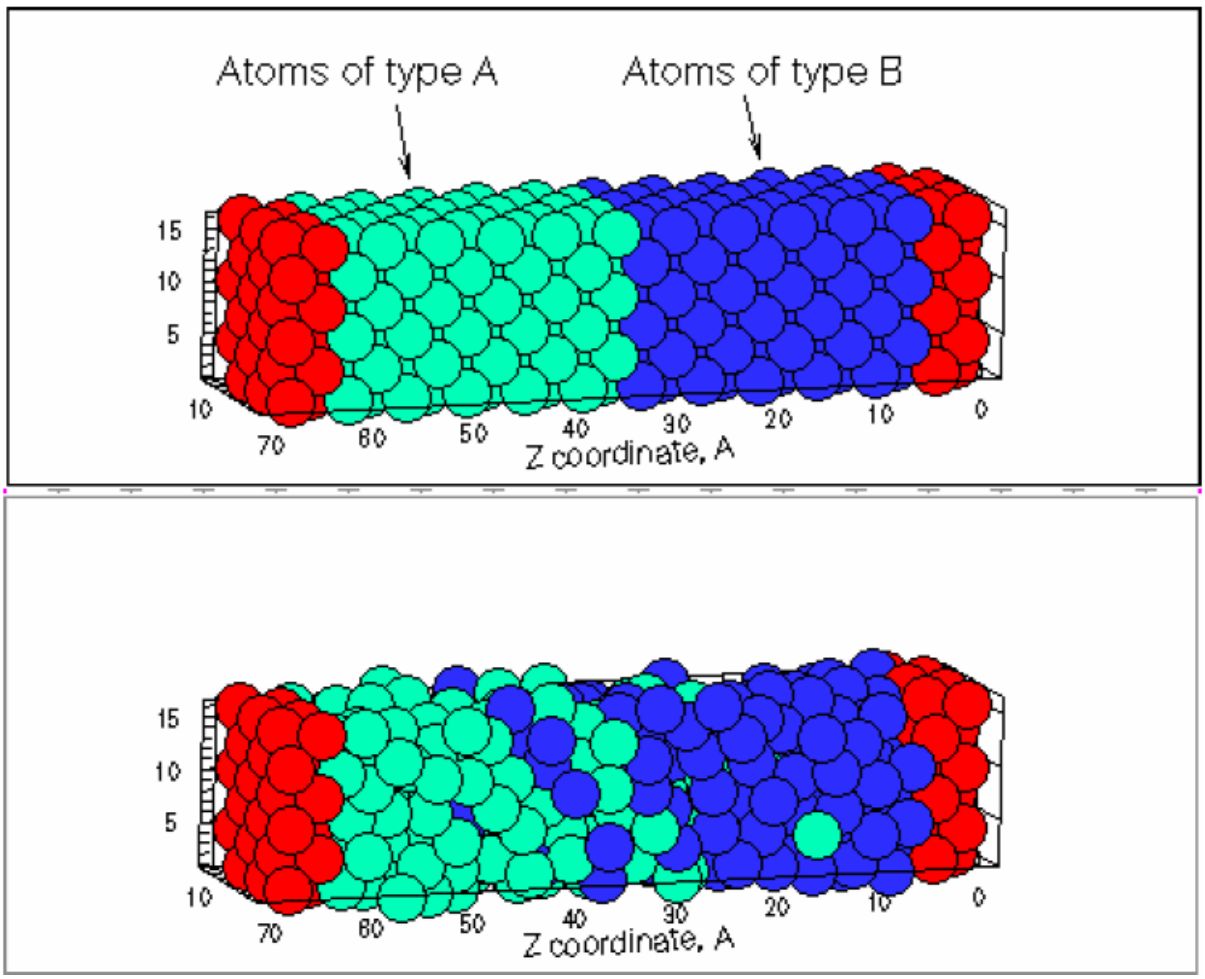

Figure 2.1: *The schematic diagram of an atomic diffusion. Taken from reference [1].*

2.1. Diffusion Laws

Diffusion is governed by Fick's first and second laws. In an isotropic medium, physical and chemical properties are independent of direction. If we consider the flux (J) of diffusing atoms as indicated in Figure 2.2, the flux (J) can be written as:

$$J = \frac{1}{A}\frac{dn}{dt} \tag{2.1}$$

where J can be defined as the number of atoms diffusing through a unit area per unit time (atoms/m^2.s) and dn/dt is the number of atoms crossing area A per unit time.

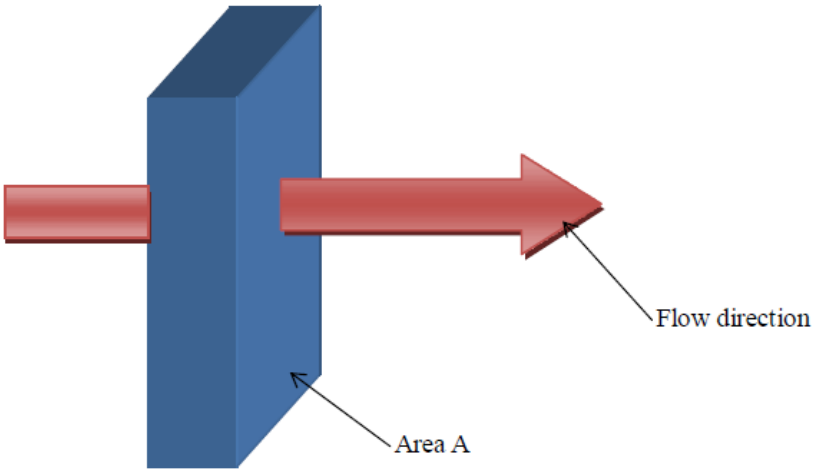

Figure 2.2: *Illustration of diffusion flux.*

According to Fick's first law for an isotropic medium the diffusion flux of atoms can be written as:

$$J_x = -D\frac{\partial C}{\partial x} \tag{2.2}$$

where J_x is the diffusion flux of atoms, C is the concentration while D is a proportionality factor denoted as the diffusion coefficient and $\frac{\partial C}{\partial x}$ is known as the concentration gradient. The negative sign in the equation 2.2 indicates that the diffusion flux and the concentration gradient are in opposite directions. Using a vector notation, Fick's first law can be generalised in three dimensions as:

$$\vec{J} = -D\vec{\nabla}C \tag{2.3}$$

The operator $\vec{\nabla}$ acts on the concentration field C(x,y,z,t) and produces the concentration gradient field $\vec{\nabla}C$. The number of diffusing atoms is usually conserved in diffusion processes [2]. An equation of continuity can be derived for diffusing species that obeys law of conservation [2]. The result of such derivation is given in equation 2.4:

$$-\vec{\nabla}\cdot\vec{J} = \frac{\partial C}{\partial t} \tag{2.4}$$

$\vec{\nabla}$ is the vector operation divergence.

Combining Fick's first law and equation 2.4 results in Fick's second law (diffusion equation):

$$\frac{\partial C}{\partial t} = \vec{\nabla}\cdot(D\vec{\nabla}C) \tag{2.5}$$

In an ideal solid solution, the diffusivity (diffusion coefficient) is independent of concentration and the above equation then simplifies to:

$$\frac{\partial C}{\partial t} = D\Delta C \tag{2.6}$$

where, Δ is the Laplace operator. This equation is called linear diffusion equation.

2.2. Diffusion coefficient

For an initially Gaussian implanted profile, Fick diffusion differential equation is given by [3]:

$$N(x,t) = \frac{1}{2\sqrt{\pi Dt}} \int_0^\infty \left[N(\xi,0)\exp\left(-\frac{(\xi - x)^2}{4Dt} \right) + N_I(-\xi,0)\exp\left(-\frac{(\xi + x)^2}{4Dt} \right) \right] d\xi \tag{2.7}$$

Where *N(x,t)* is the number of diffusing particles per unit volume at time *t* and distance *x*, *N(ξ,0)* is the original distribution of the impurity and $N_I(\xi,0)$ is a function that is determined from the boundary conditions. The following conditions are used: $x = 0$ for $t > 0$, the number of implanted particles is a constant N_0, $N(x,t) \rightarrow 0$ as $x \rightarrow \infty$, leading to:

$$N_I(-\xi,0) = -kN(\xi,0) \tag{2.8}$$

where k is a constant. Equation (2.7) can be written as:

$$N(x,t) = \frac{1}{\sqrt{\pi Dt}} \int N(\xi,0) \left[\exp\left(-\frac{(\xi - x)^2}{4Dt} \right) - k \cdot \exp\left(-\frac{(\xi + x)^2}{4Dt} \right) \right] d\xi \tag{2.9}$$

The general solution to the diffusion differential equation was obtained by Malherbe [3], for $-1 < k < 1$, and it is given as:

$$N(x,t) = \frac{A_0 \cdot \Delta R_p}{2\sqrt{2Dt + \Delta R_p^2}} e^{\left(\frac{(x - R_p)^2}{4Dt + 2\Delta R^2{}_p} \right)} \times \left[\begin{array}{l} 1 + erf\left(\dfrac{2DtR_p + x\Delta R_p^2}{\Delta R_p \sqrt{2(2Dt)^2 + 4Dt\Delta R_p^2}} \right) \\ - ke^{\left(\frac{xR_p}{Dt + \Delta R_p^2/2} \right)} \\ \times \left\{ 1 + erf\left(\dfrac{2DtR_p - x\Delta R_p^2}{\Delta R_p \sqrt{2(2Dt)^2 + 4Dt\Delta R_p^2}} \right) \right\} \end{array} \right] \tag{2.10}$$

and

$$k = 1 - \left[\frac{2C_0}{A_0} \frac{\sqrt{2Dt + \Delta R_p^2}}{\Delta R_p} \exp\left(\frac{R_p^2}{4Dt + 2\Delta R_p^2} \right) \div \left\{ 1 + erf\left(\frac{R_p \sqrt{Dt}}{\Delta R_p \sqrt{2Dt + \Delta R_p^2}} \right) \right\} \right] \qquad (2.11)$$

where R_p is the projected range, ΔR_p is the range sraggling and A_0 is a constant as shown in the equation 2.12and C_0 is a time-dependent surface concentration as given in Equation 2.13. For a purely Gaussian initial profile, we have:

$$N(\xi, 0) = A_0 \exp\left(- \frac{(\xi - R_p)^2}{2\Delta R_p^2} \right) \qquad (2.12)$$

And the time-dependent surface concentration is given by;

$$N(0, t) = C_0(t) \qquad (2.13)$$

For the general solutions of Fick differential equation, k = -1 represents the case of a perfectly reflecting boundary at x= 0 with zero flux at the origin, while k = 1 represents the case of a perfect sink at the surface of the substrate. These solutions are also given by Boltaks [4].

The general solution (equation 2.10 and 2.11) is applicable to the shallow implantations, similar to this study, where some of the implanted species are released to the environment through the surface leaving a non-zero surface concentration of the implants:

$$N(0, t) = \frac{(1 - k)K}{4\sqrt{\pi D(t + t_0)}} e^{\left(\frac{(R_p)^2}{4D(t + t_0)} \right)} \left\{ 1 + erf\left(\frac{tR_p}{\sqrt{4Dtt_0(t + t_0)}} \right) \right\} = C_0(t) \qquad (2.14)$$

Equation 2.14 is used for the fitting of experimental data to the general solution (equation. 2.10 and 2.11).

Figures 2.3 and 2.4 show an example of the simulated diffusion profiles for the cases. k = 1 and k = -1. The implantation parameters used for the Gaussian profile are: R_p = 120 nm, ΔR_p = 30 nm and A_0 = 0.66 atomic percent as given in [3].

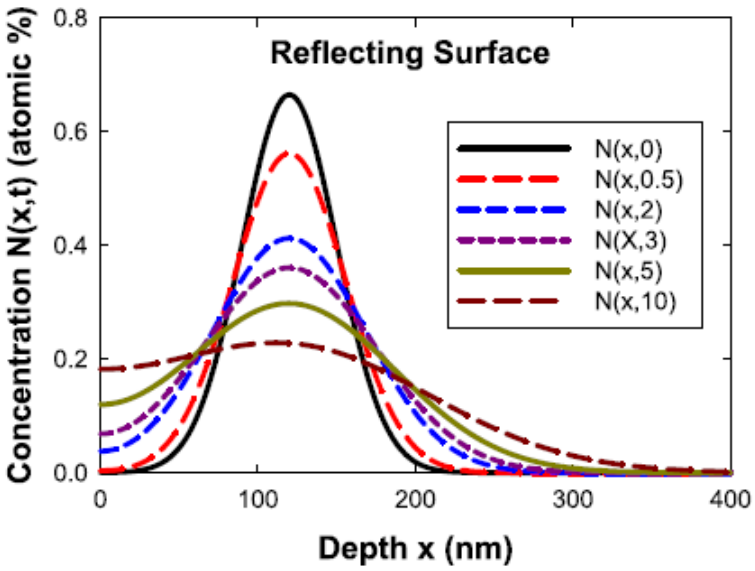

Figure 2.3: *A simulated diffusion profile, i. e. Equation. (2.10) and (2.11), for the case k = -1 (i.e. a perfectly reflecting boundary at x = 0), is given for different diffusion times t (in hours) indicated in the figure. Typical implantation values were used for the initial Gaussian profile: R_p = 120 nm, ΔR_p = 30 nm, A_0 = 0.66 atomic percent, and a diffusion coefficient D = 0.1 nm^2 s^{-1}. Taken from reference [3]*

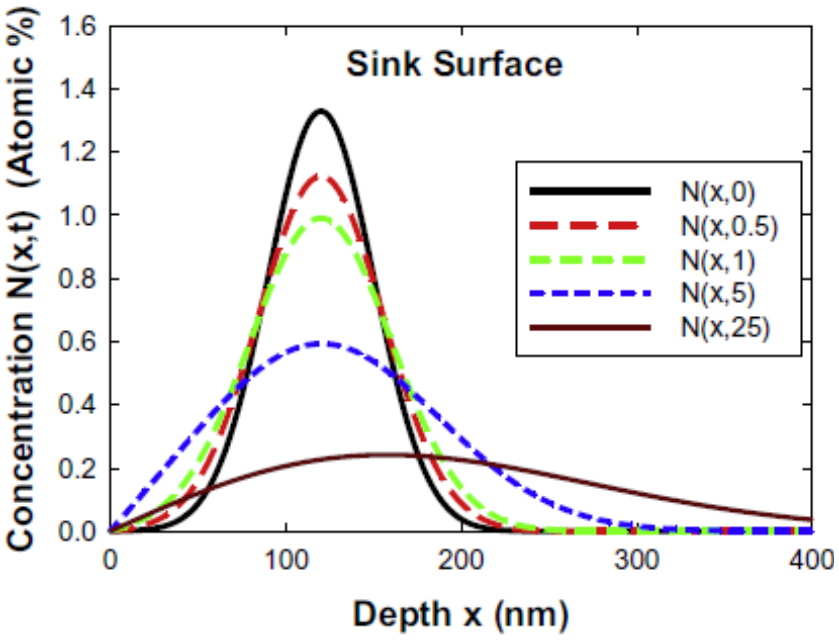

Figure 2.4: *A simulated diffusion profile, i. e. Equation (2.10) and (2.11), for the case k = 1 (i.e. a perfect sink at the surface), is given for different diffusion times t (in hours) indicated in the figure. Typical implantation values were used for the initial Gaussian profile: R_p = 120 nm, ΔR_p = 30 nm, A_0 = 0.66 atomic percent, and a diffusion coefficient D = 0.1 nm^2 s^{-1}. Taken from reference [3].*

For most part of the results presented in this thesis, It was observed that, the initial profiles were almost Gaussian and became asymmetric with increasing annealing temperatures and they also shifted towards the surface, see Chapter 6. In this study, the implanted species slightly diffused deeper into the substrate but mostly outwards through the surface into the environment. Most appropriately, the simulated diffusion profiles of Figure 2.3 resembles the diffusion depth profiles obtained in this study.

The diffusion coefficient depends exponentially on temperature in a limited temperature range. This dependence has important consequences with regard to material behaviour and is governed by Arrhenius equation [5]:

$$D = D_0 \exp\left(-\frac{E_a}{k_B T}\right) \tag{2.15}$$

where D_0 is a temperature-independent pre-exponential factor (m^2/s), E_a is the activation energy for diffusion (J/mol), K_B is the Boltzmann's constant and T is the absolute temperature (K). Taking the natural log, equation 2.15 can be rewritten as:

$$\ln D = \ln D_0 - \frac{E_a}{k_B}\left(\frac{1}{T}\right) \tag{2.16}$$

From equation 2.16, it is clear that the activation energy E_a and the pre-exponential D_0 can both be estimated from a graph of ln$D$ versus 1/T. Figure 2.5 shows a typical example of such graph. E_a and D_0 can be deduced directly from the slope and y intercept of the graph respectively.

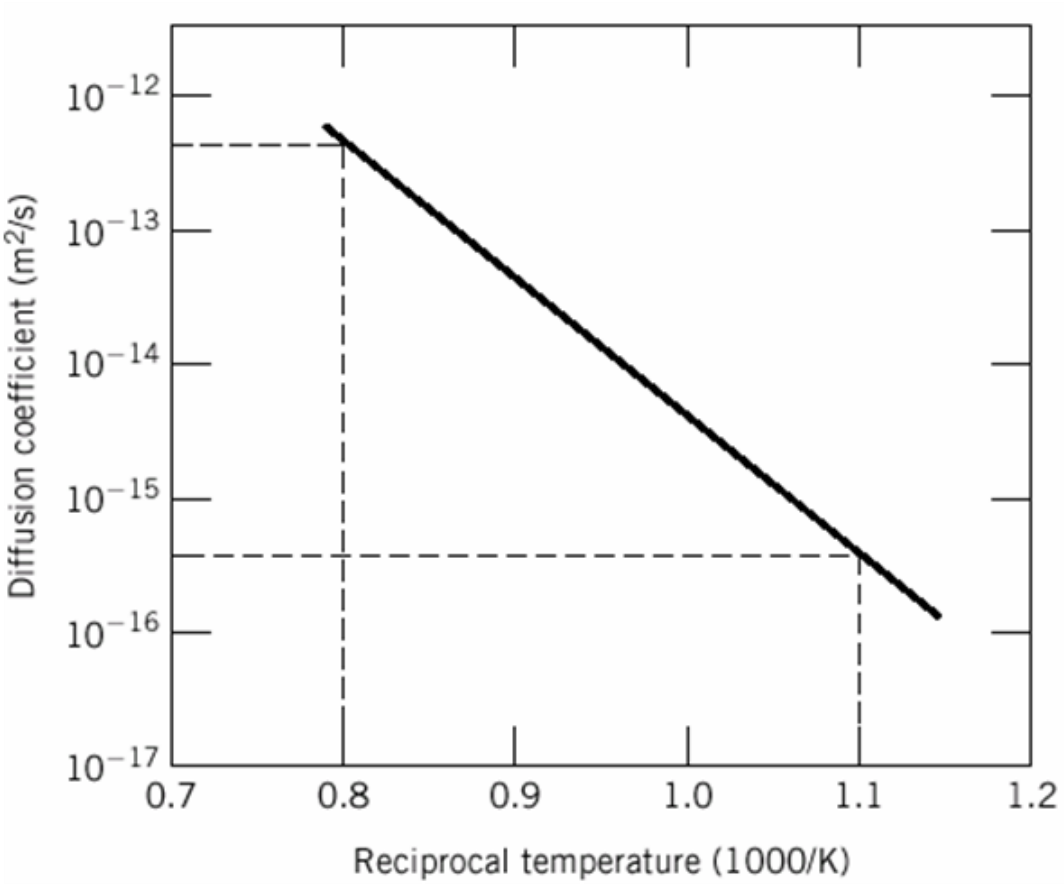

Figure 2.5: *A graph of lnD vs 1/T. Taken from reference [2].*

2.3 Diffusion mechanisms

Many reactions and processes that are important in the analysis of materials depend on mass transfer within a specific solid [5]. As already mentioned above, atoms are in constant vibration about their lattice positions in solid materials. In order for an atom to change position, it must have sufficient energy to break bonds that connects it with neighbouring atoms. In a material of interest, diffusion can occur via different mechanisms.

In this thesis, I shall focus on the diffusion mechanisms that occur in single crystalline 6H-SiC as well as polycrystalline SiC. A single crystalline material is described as one in which the entire crystal lattice is continuous and unbroken to the edges of the sample, without the presence of grain boundaries. On the other hand, a polycrystalline material consists of many grains with varying size and orientation. A clear distinction of single crystalline vs polycrystalline materials is illustrated in Figure 2.6 for silicon.

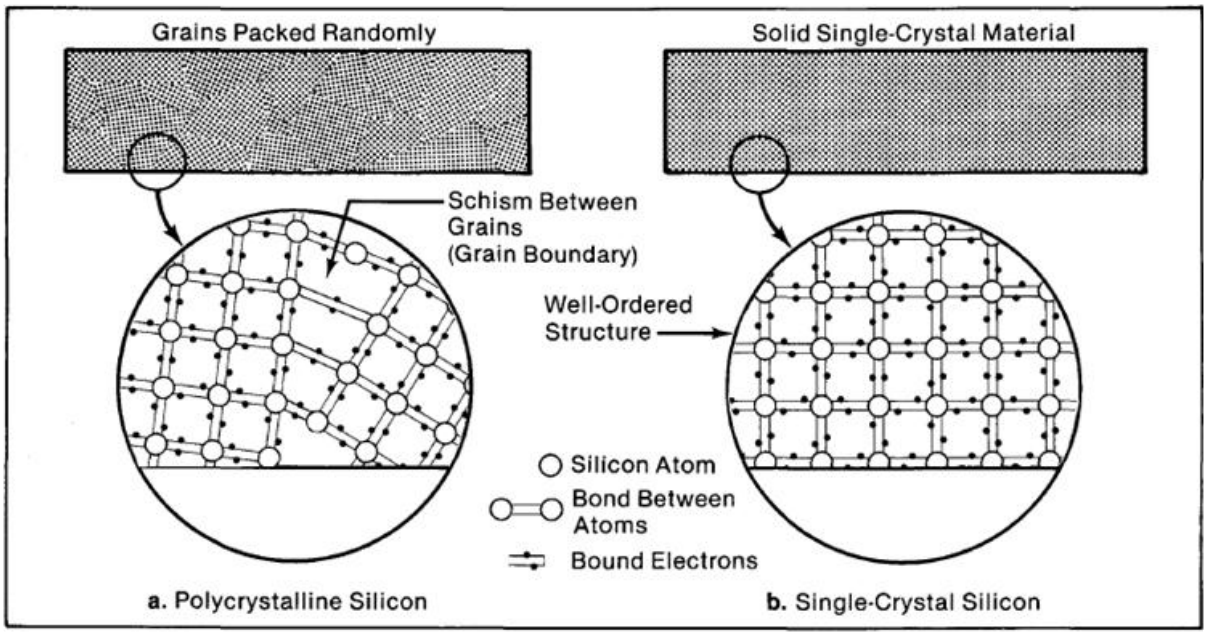

Figure 2.6: *An illustration of the difference between polycrystalline and single crystalline silicon (Si). Taken from reference [6].*

It is important to identify factors that affect diffusion before discussing diffusion mechanisms, these factors include: diffusing species, temperature, microstructure and host atoms.

2.4 Diffusion mechanisms in crystalline materials

2.4.1 Interstitial Mechanism

In interstitial diffusion mechanism, considerably smaller impurity atoms are incorporated into interstitial sites of the lattice host forming an interstitial solid solution. An interstitial impurity can jump from one interstitial site to a neighbouring interstitial site, this phenomenon is shown in Figure 2.7. Interstitial diffusion is generally faster since it is not assisted by any defect in mediating a direct interstitial jump, thus the interstitial atom does not need to wait for a defect in order to perform a jump. No permanent displacement of host atoms remains after a jump is completed. Interstitial mechanism is the simplest diffusion mechanism. Smaller atoms such as C, H, and O are preferred in this mechanism in metals and other materials [7].

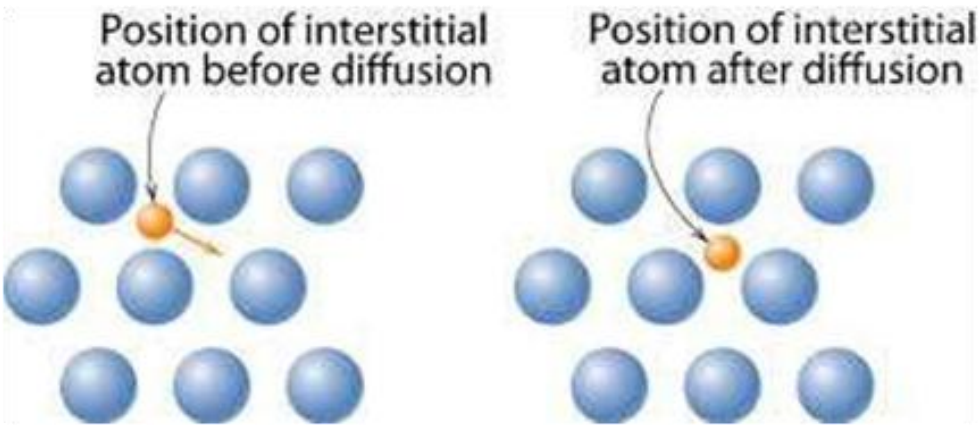

Figure 2.7: *Schematic representations of interstitial diffusion. Taken from reference [8].*

2.4.2 Vacancy Mechanism

In a vacancy mechanism, an atom diffuses by jumping from its lattice site into a neighbouring vacancy as demonstrated in Figure 2.8. To jump from one lattice site to another, an atom needs energy to break bonds with their neighbouring atoms. The energy normally comes from the thermal energy of atomic vibrations ($E_{av} \approx k_B T$). It was revealed that the dominant mechanism for diffusion of host atoms and of substitutional impurities in metals is the vacancy mechanism [2]. Thus vacancies are well known as the most important form of thermally induced atomic defects in materials. In this mechanism, the flow of atoms and the flow of vacancies are in opposite directions, thus the rate of diffusion is mainly dependent on the number of available vacancies. When all atoms exchanging positions are of the same type, the diffusion is termed self-diffusion which mostly takes place when there are vacancies present [7].

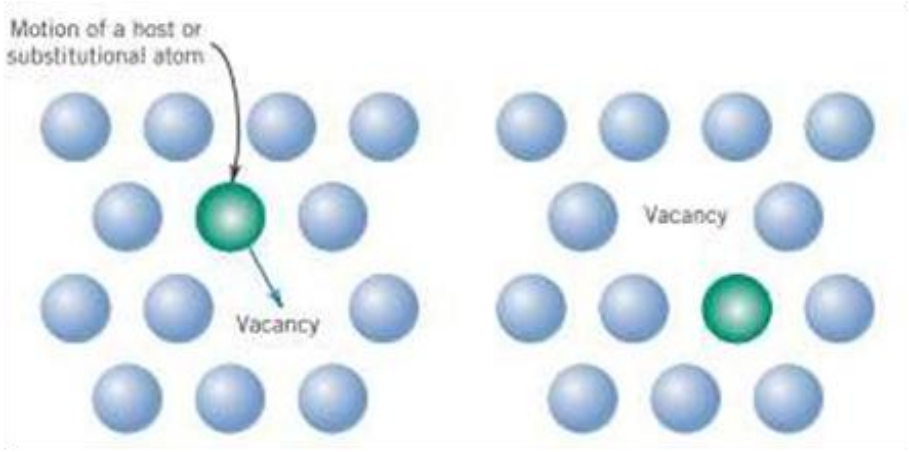

Figure 2.8: *A schematic representation of vacancy diffusion mechanism, i.e. movement of an atom from a lattice point to a vacant site. Taken from reference [8].*

2.4.3 Interstitialcy Mechanism

Diffusion may occur by interstitialcy mechanism when the interstitial impurity atom is approximately the same size as the host atoms. Figure 2.9 illustrates interstitialcy diffusion mechanism. A self-interstitial replaces an atom on a substitutional site, which also replaces a neighbouring lattice atom from its lattice position. At least two atoms move simultaneously in interstitialcy mechanism, thus it is also a collective mechanism. The interstitialcy mechanism is important in radiation damage enhanced diffusion [2]. In thermal diffusion the interstitialcy mechanism is negligible because the self-interstitials have fairly high formation enthalpies compared to vacancies [9, 10]. In case of larger impurity atoms residing in interstitial positions, larger amounts of energy will be required to overcome the potential barrier associated with the large distortion to enhance an interstitial jump.

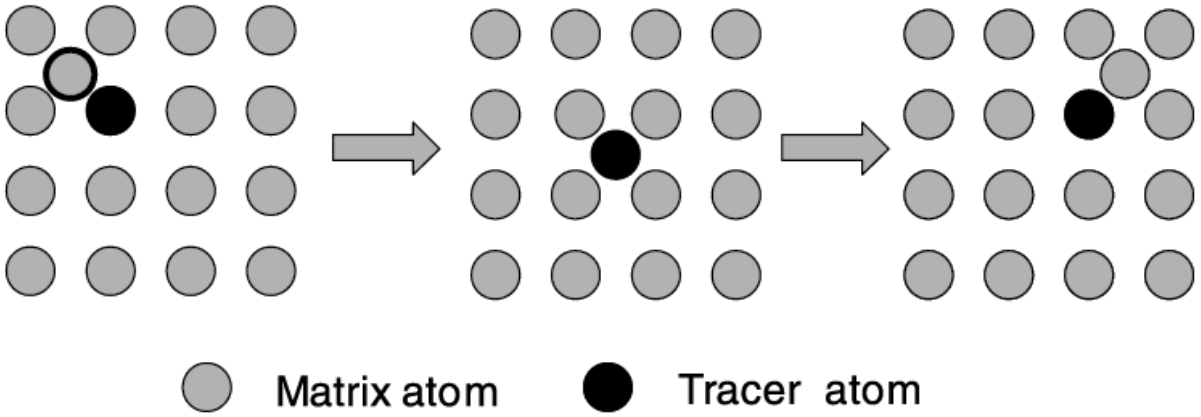

Figure 2.9: *Interstitialcy diffusion mechanism (collinear jumps).Taken from reference [2].*

2.5 Diffusion in polycrystalline materials

There are a number of diffusion kinetics observable, depending on the annealing temperature range and time, lattice and grain boundary parameters [2]. In order to be able to interpret the results of any diffusion study, it is important to understand each of the diffusion kinetics/regimes. A widely used classification of diffusion kinetics for polycrystals was introduced by Harrisons [11]. The three regimes of the diffusion kinetics are classified as type A, B, and C and figure 2.10 shows the schematic representation of the three regimes.

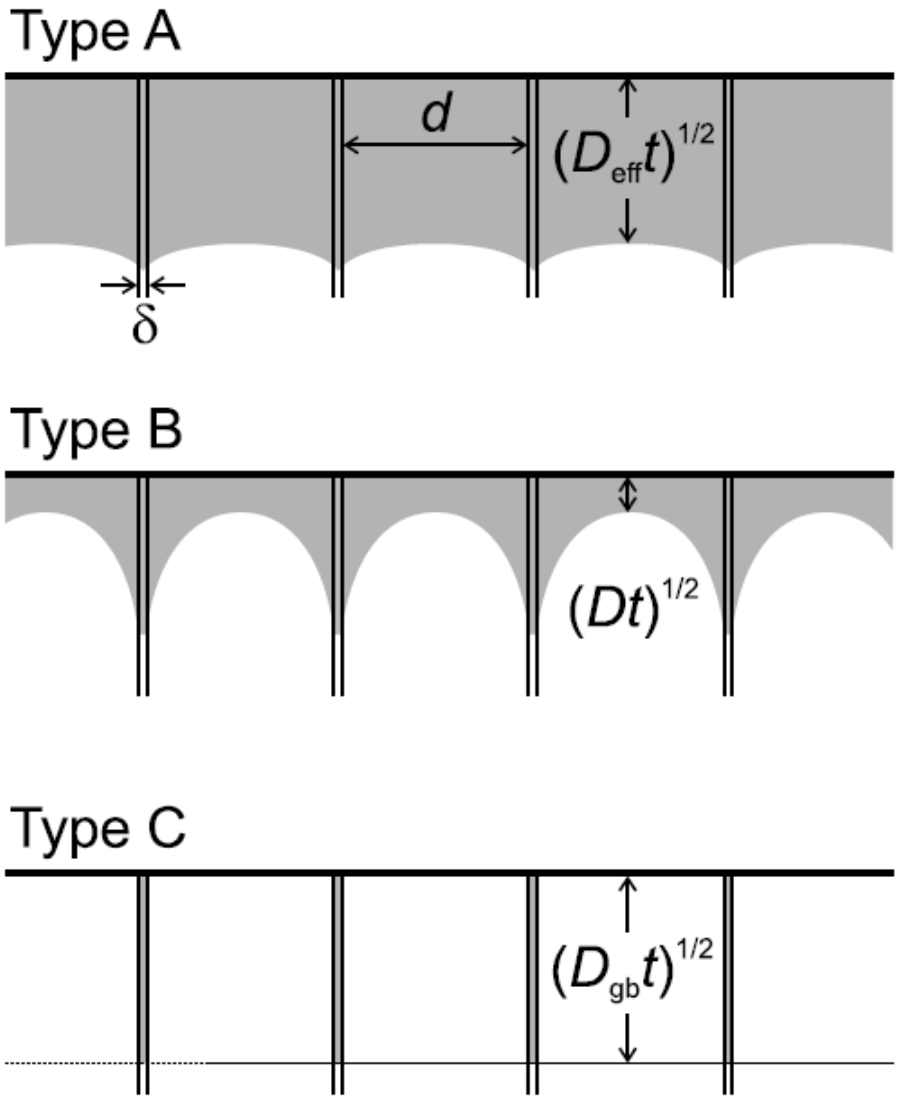

Figure 2.10: *Illustration of the type A, B, and C diffusion regimes in a polycrystal according to Harrisons classification. D is the lattice diffusivitty, d is the grain size, δ is the grain boundary width and the variable t correspond to time. Taken from reference [2].*

2.5.1 Type A kinetics Regime

This kind of diffusion kinetics is observed at high annealing temperatures, or long annealing times, or in materials with small grain size, or any combination of these. The lattice diffusion length, $\sqrt{Dt}$ only needs to be a little bit greater than the grain size *d* for a diffusing atom to be able to visit a number of grains and grain boundaries during a diffusion experiment [12], thus:

$$\sqrt{Dt} \geq d/0.8 \qquad (2.17)$$

From a macroscopic point of view, a polycrystal obeys Fick's law for a homogeneous medium with an effective diffusion coefficient D_{eff}. An approximate expression for the effective diffusivity in polycrystals is given by [2]:

$$D_{eff} = gD_{gb} + (1-g)D \tag{2.18}$$

where g is the fraction of atomic sites in the grain boundary of polycrystalline material, given by:

$$g = \frac{q\delta}{d} \tag{2.19}$$

where q is a numerical factor that depends on the grain size ($q= 1$ represents parallel grain boundaries and $q = 3$ represents cubic grains) and δ is the grain-boundary width. Usually $D_{gb} >> D$ and the only quantity determined from the diffusion profile is the effective diffusivity [2]. Thus, diffusion coefficients measured on polycrystalline materials can be larger than diffusion coefficients measured on single crystalline samples.

In the case of fine-grained polycrystalline materials in which d is so small, or segregation is strong so that $d << s\delta/2$, the effective diffusivity [2, 13, 14 - 15] is given by:

$$D_{eff} \approx sgD_{gb} + D \tag{2.20}$$

where s is the segregation factor of the diffuser.

2.5.2 Type B kinetics Regime

This type of diffusion kinetics emerges with annealing at lower temperatures, or with shorter annealing times, or in materials with large grain size, or with any combination of all these. In these conditions, the lattice diffusion length, $\sqrt{Dt}$, can be very much smaller than d, at the same time, the width of the grain-boundary fringes can be larger than the grain-boundary width δ. An effective width, $s\delta$ must be considered in the case of solute diffusion with segregation. The condition for type B kinetics is [2]:

$$s\delta << \sqrt{Dt} << d \tag{2.21}$$

For self-diffusion, the product, δD_{gb}, and for solute diffusion, the triple product, $s\delta D_{gb}$, can be determined using the procedure described in [2].

2.5.3 Type C kinetics Regime

This type of diffusion kinetics correspond to conditions where lattice diffusion is not noticeable. Diffusion takes place only along grain boundaries without essential leakage into adjacent grains [2]. This diffusion kinetics can emerge at sufficiently low annealing temperatures, or very short diffusion times, or a combination of these. The conditions for type C kinetics include:

$$\sqrt{Dt} << s\delta \tag{2.22}$$

The grain boundary diffusion studies in this regime are difficult, since the small amount of the diffuser has to be detected inside the boundaries. The grain-boundary diffusivity D_{gb} can be determined if type C kinetics profiles are measured in polycrystals.

In polycrystalline materials, diffusion can involve short circuit mechanisms such as: some crystalline defects and along the grain boundaries. The model for diffusion uses an effective diffusion coefficient (D_{eff}) by combining the lattice and grain boundary diffusion coefficients [16]. Grain boundary diffusion in metals at lower temperatures is faster than lattice diffusion [2]. Due to a smaller activation enthalpy for grain boundary diffusion, the difference between the two diffusion mechanisms (thus, lattice and grain boundary) increases with decreasing temperature [2, 17]. The grain boundary diffusivity applicable to measurements with temperatures below 500 K [2], is given by:

$$D_{gb} = D_{gb}^{0} \exp\left(-\frac{\Delta H_{gb}}{k_B T}\right) \tag{2.23}$$

where ΔH_{gb} is the activation enthalpy and D_{gb}^{0} is a pre-exponential factor.

It appears that the grain boundary diffusion is a complex process involving direct lattice diffusion from the source, lattice diffusion into fringes around the grain boundary, diffusion along the grain boundary and leakage of the diffusion from the grain boundary [2]. All these possibilities in diffusion make diffusion in polycrystalline materials more complex.

References

[1] People.virginia.edu. 2020. [online] Available at: <http://people.virginia.edu/~lz2n/mse209/Chapter5.pdf> [Accessed 24 July 2020].

[2] Mehrer, H., 2007. *Diffusion in solids*. Dordrecht: Springer.

[3] Malherbe, J. B., Selyshchev, P., Odutemowo, O., Theron, C. C., Njoroge, E. G., Langa, D. and Hlatshwayo, T. T., 2017. Diffusion of a mono-energetic implanted species with a Gaussian profile. *Nuclear Instruments and Methods in Physics Research Section B: Beam Interactions with Materials and Atoms*, 406, pp.708-713.

[4] Boltaks, B., 1963. *Diffusion in semiconductors*. London: Academic Press, p.Chapter 4.

[5] fdocuments.in. n.d. *Chapter 7 Diffusion in solids - [Download PDF]*. [online] Available at: <https://fdocuments.in/download/chapter-7-diffusion-in-solids> [Accessed 25 July 2020].

[6] Thomas, V. C., 1981. *Basic photovoltaic principles and methods | energy-models.com*. [online] Energy-models.com. Available at: <http://energy-models.com/basic-photovoltaic-principles-and-methods> [Accessed 25 July 2020].

[7] People.virginia.edu. n.d. [online] Available at: <http://people.virginia.edu/~lz2n/mse209/Chapter5.pdf> [Accessed 27 July 2020].

[8] Callister, W. and Rethwisch, D. (2011). *Materials science and engineering*. 8th ed. USA: John Wiley & Sons.

[9] Cahn, R. and Haasen, P., 1996. *Physical metallurgy*. 4th ed. Amsterdam: North-Holland.

[10] Ullmaier, H. and Ehrhart, P., 1991. *Atomic Defects in metals*. Berlin and Heidelberg: Springer.

[11] Harrison, L., 1961. Influence of dislocations on diffusion kinetics in solids with particular reference to the alkali halides. *Transactions of the Faraday Society*, 57, p.1191.

[12] V. Belova, G. E. Murch, I., 2001. The transition from Harrison type-B to type-A kinetics in grain-boundary tracer diffusion. *Philosophical Magazine A*, 81(10), pp.2447-2455.

[13] Kaur, I., Mishin, Y. and Gust, W., 1995. *Fundamentals of grain and interphase boundary diffusion*. Chichester [etc.]: Wiley.

[14] Mortlock, A., 1960. The effect of segregation on the solute diffusion enhancement due to the presence of dislocations. *Acta Metallurgica*, 8(2), pp.132-134.

[15] Belova, I. and Murch, G., 2004. In: D. Beke, ed., *Nanodiffusion*. Zurich, Switzerland: Trans Tech Publications Ltd, p.23.

[16] Belova, I. and Murch, G., 2004. Analysis of the effective diffusivity in nanocrystalline materials. *Journal of Metastable and Nanocrystalline Materials*, 19, pp.25-34.

[17] Shewmon, P., 1989. *Diffusion in solids*. USA, p.57.

CHAPTER 3

ION IMPLANTATION

Ion implantation is a process whereby energetic ions impinging a target material interact with the target atoms resulting in energy loss, until they come to rest at a certain depth inside the target material. As they penetrate the material, they undergo collisions with target atoms displacing them from their lattice positions resulting in lattice disorder or defects. Some of the target atoms can gain enough energy to overcome all forces holding it together with neighbouring atoms and as a result, this knocked off atom may continue to collide with neighbouring atoms (collision cascade) creating more defects in the material. Too many collisions and displacements of atoms may result in a complete disarrangement of atoms in the material. When the long-range periodicity of atoms is lost in a material, the material is said to be amorphous (complete disorder) [1]. This chapter discuses the process of ion implantation and the interaction of accelerated ions with the atoms of the target material.

3.1 Ion interaction

In ion implantation, an ion with a certain energy is normally accelerated towards a target of interest, where it interacts with the target atoms until it comes to rest. It is a process which is used mostly to dope semiconductors to either n-type or p-type based on the ideal properties of a particular semiconductor [2]. Implantation or doping of materials is capable of converting a non-conductive material into a conductive one. It is also used to introduce a controlled amount of atoms into a target material for a specific purpose. For instance, in this study, Eu^{+} ions of 270 keV were implanted into polycrystalline and 6H-SiC silicon carbide to study the migration behaviour of Eu in SiC substrates due to radiation damage introduced.

During ion implantation, ions interact with atoms of target material which results in scattering events (a process in which the penetrating ions are forced to deviate from their original straight path due to localized non-uniformity in the medium being traversed). These interactions slow down the penetrating ions and reduce their energy until they stop. Depending on the energy of the projectile ion, the ion energy will continue to be reduced and it will eventually stop somewhere beyond the surface layers due to the total loss of its energy.

For example, the use of 3 to 500 keV energy for boron, phosphorus or arsenic dopant ions is sufficient to implant the ions from 100 to 10000Å below a silicon surface [3]. The average penetration depth depends on the nature of the ion being accelerated, the acceleration energy and the target material. Ion distributions with average depths from 10 nm to 10 μm can be achieved with implantation energies ranging from hundreds to several million electron volts. Fluences can range from 10^{11} atoms/cm^2 for threshold adjustment, to 10^{18} atoms/cm^2 for buried dielectric formation [4]. In this study, a fluence of 10^{16} atoms/cm^2 of Eu^+ was used.

3.2 Energy loss of ions

It is of the fundamental importance to understand the mechanics of ions traversing matter in ion beam analysis of material. The depth scales follow directly from the energy lost by the penetrating particles and the energy loss affects both compositional and quantitative analysis. Different scientific books have varying definitions of the concept of energy loss. We define the energy loss per unit length as dE/dx in this study:

$$\lim_{\Delta x \to 0} \frac{\Delta E}{\Delta x} = \frac{dE}{dx}(E) \tag{3.1}$$

where ΔE denotes the amount of energy lost per distance traversed, Δx. The relative importance of the various interaction processes between the ion and the target medium depends heavily on the energy/velocity of the ion and on the the ion charge state as well as target atoms. As the ion velocity increases, the nuclear energy loss (section 3.3) diminishes. The electronic energy loss (section 3.4), i.e. inelastic collisions with the atomic electrons, is usually the main mechanism through which ions lose their energy when they have larger incident energy. The total energy loss of an ion is obtained as a sum of the nuclear and electronic contributions as shown in equation (3.2).

As mentioned earlier, an energetic ion penetrating material, interacts with the atoms of material which result in a number of collisions between ion and host atoms. Figure 3.1 shows a series of collisions of ions-host atoms until they come to rest.

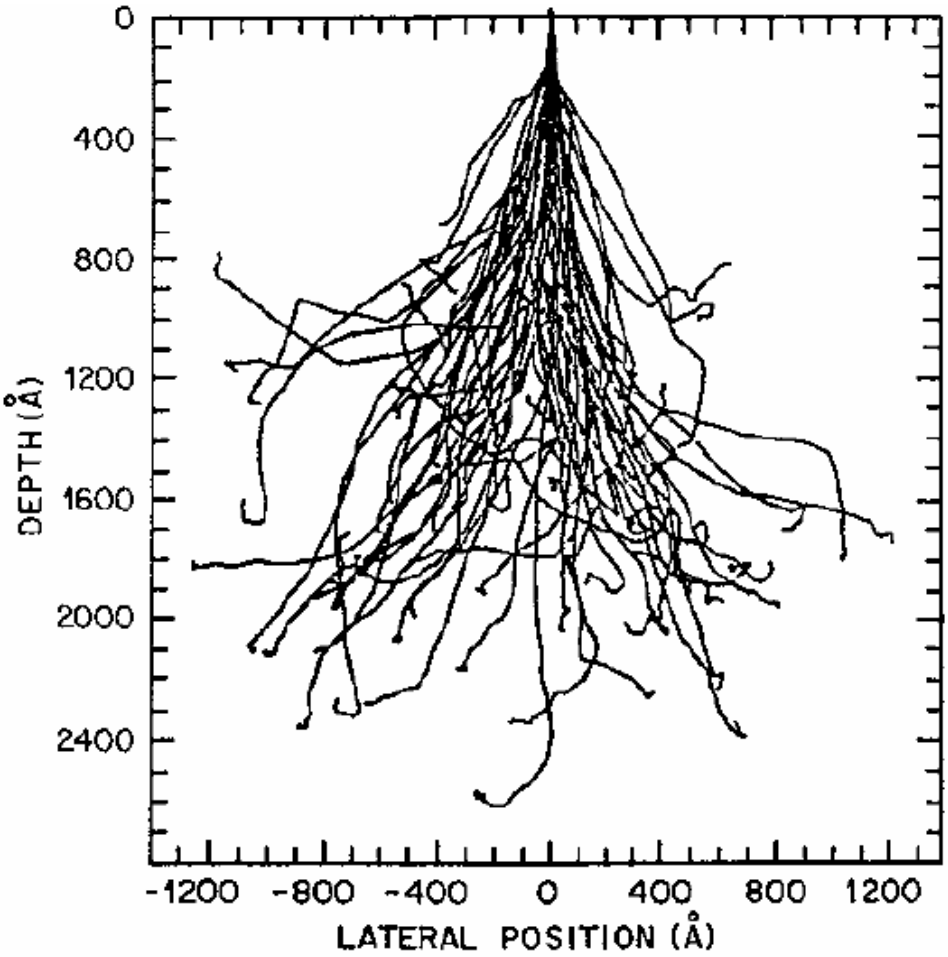

Figure 3.1: *Monte Carlo calculation of 128 ion trajectories for 50 keV boron implanted into silicon. Taken from reference [4]*

Electronic stopping and the nuclear stopping are the two key mechanisms through which ions lose their energy when impinging a material. Figure 3.2 shows nuclear and electronic stopping as a function of ion's velocity. The region I in Figure 3.2 is the low energy region. In this region the nuclear stopping dominates. The region in the middle (II) with intermediate energies is dominated by electronic stopping. The electronic stopping reaches its maximum and then we enter a region of even higher energies called a Bethe-Bloch region (III) where only electronic stopping dominates. Typical energies for ion implantation (10 to 200 *keV*), fall within region I in the figure, which is dominated by nuclear stopping [4].

The total stopping power *S* of the target, defined by the energy loss (*E*) per unit length (*x*) of the ion, is given as:

$$S = \left(\frac{dE}{dx}\right)_{nuclear} + \left(\frac{dE}{dx}\right)_{electronic} = S_n + S_e \qquad (3.2)$$

where S_n and S_e are the nuclear stopping factor and electronic stopping factor respectively.

A frequently used quantity is the stopping cross section (ε), which can also be divided into electronic stopping cross-section which includes all the processes in which the particle transfers its energy to the target electrons, and the nuclear stopping cross-section which takes into account energy transfers from the incident particle to the target nuclei. The ε can be defined by:

$$\varepsilon = \frac{1}{N}\left(\frac{dE}{dx}\right) \tag{3.3}$$

where N is the target density.

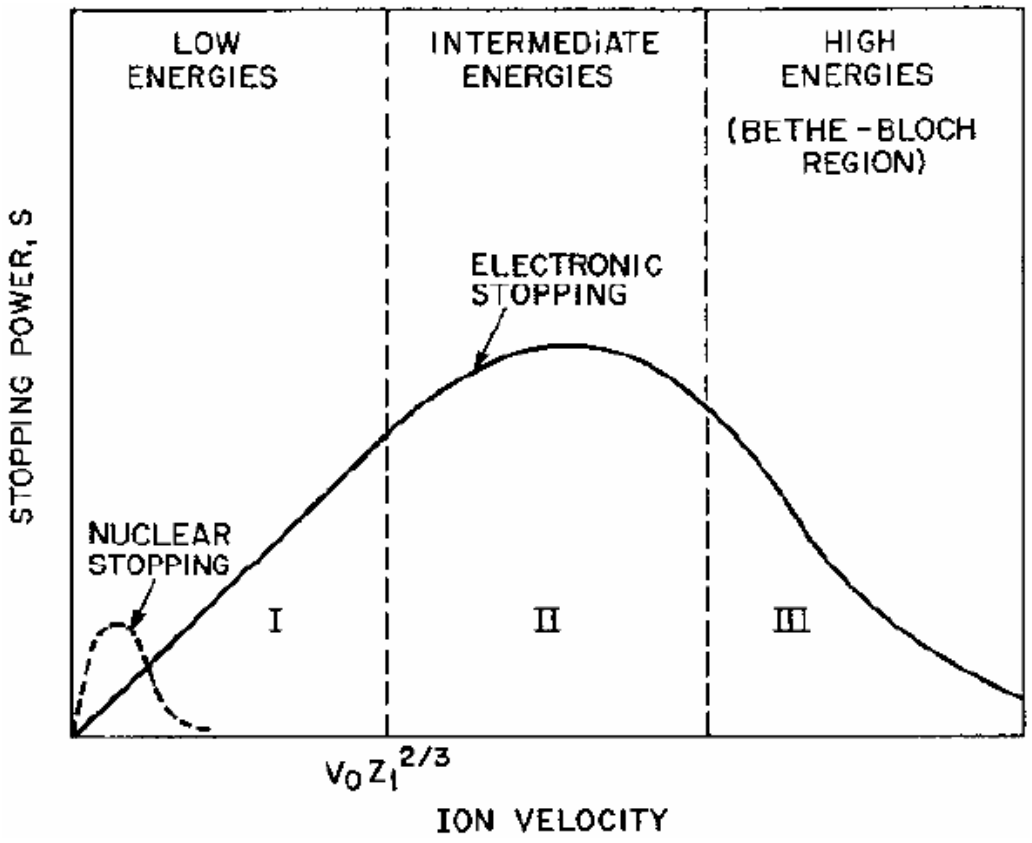

Figure 3.2: *A representation of the contribution of electronic stopping and nuclear stopping to the stopping power S as a function of ion velocity. Taken from reference [4].*

Region I is the nuclear stopping section discussed in section 3.3. A free electron gas with a density ρ is assumed, in the calculation of the electronic stopping for this region of low energy [5, 6]. The ion's electronic stopping cross section ε_e is then given by [7]:

$$\varepsilon_e = \int I(v,\rho)(Z_1(v))^2 \rho dV \tag{3.4}$$

where I is the stopping interaction function of an ion of unit charge with velocity v, Z_1 is the charge of the ion, ρ is the electron density of the charge and the integral is performed over each volume element of the target dV

In region II, the ion is partly ionized and has a velocity approximately equal to the Bohr velocity, the electronic stopping reaches its maximum. Electronic energy loss dominates at higher ion velocities (about $10^5 m/s$ and higher). The ion is stripped of its electrons at these high velocities.

In region III, corresponding to higher energies in Figure 3.2., the velocity of the ion is much higher than the Bohr velocity and therefore it is stripped of all its electrons. This region is known as Bethe-Bloch, the pair who found that the energy loss in this region is proportional to Z_1^2, where Z_1 is the atomic number of the ion [8]. Electronic stopping in this region is given by Bethe-Bloch equation [8][9]:

$$\varepsilon_e = \frac{4\pi Z_1^{\,2} Z_2 e^4}{m_e v_1^{\,2}} \left[\ln\left(\frac{2m_e v_1^{\,2}}{I} \right) + \ln\left(\frac{1}{1-\beta^2} \right) - \beta^2 - \frac{C}{Z_2} \right] \tag{3.5}$$

where m_e is the electron mass, v_1 is the velocity of the projectile, $\beta = v/c$ where c is the speed of light, I is the average ionization potential and c/Z_2 is the shell correction. The average ionization potential is defined by [10]:

$$\ln I = \sum_n f_n \ln(E_n - E_0) \tag{3.6}$$

where f_n is the dipole oscillator, E_o is the ground state energy and E_n is the excited state energy.

3.3. Nuclear Stopping

Nuclear energy loss dominates at lower energies, a region where the ion velocity (v_1) is less than $v_0 Z^{2/3}$ i.e. $v_1 < v_0 Z^{2/3}$, where v_0 is the Bohr velocity given by $v_0 = e^2/\hbar$, e is electron charge, $\hbar$ is Planck's constant and Z is the ion atomic number. In this process, ions collide with the target atoms and the positively charged ions are repelled by positive cores of the substrate lattice atoms.

Figure 3.3. shows an incident ion with mass M_1 interacting with nucleus with mass M_2 of a stationary atom. A scattering angle θ depends on masses M_1, M_2 and on b (impact parameter), and maximum energy is transferred when $b = 0$.

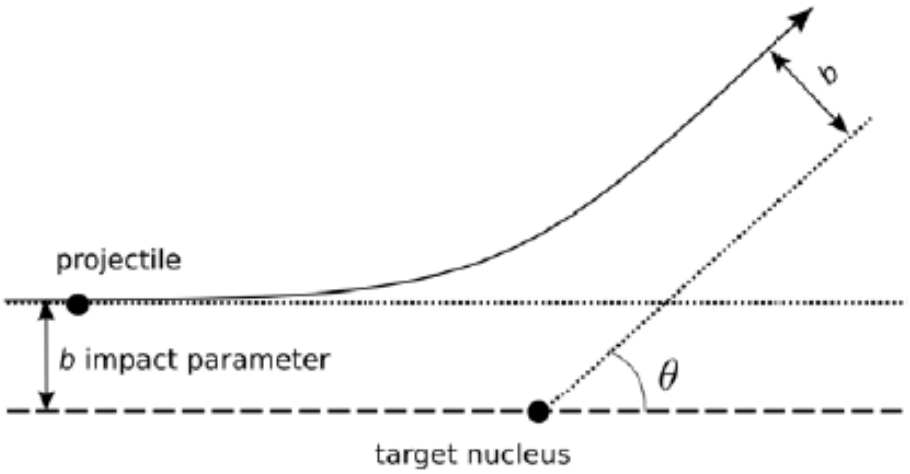

Figure 3.3: *Schematic of a nuclear scattering event between an ion of energy E_1, mass M_1 and a stationary target atom of mass M_2; b is the impact parameter. Taken from reference [11].*

Assuming that the atoms were bare nuclei, the Coulombic potential between them, at a separation r, would be [4];

$$V_c(r) = \frac{q^2 Z_1 Z_2}{4\pi\varepsilon_0 r} \tag{3.7}$$

where q is the electronic charge, ε_0 is permittivity, Z_1 and Z_2 is the atomic number of the accelerated ion and target atom respectively. Practically, the electrons screen the nuclear charge, and a screening function, $\Phi(r/a)$ [12], must be included so that the interatomic potential V(r), with the aid of Hartree-Fock and density-functional theory, is given by [13]:

$$V(r) = V_c(r)\Phi\left(\frac{r}{a}\right) \tag{3.8}$$

A collision between two atoms can be described as follows in mathematical terms: If an inelastic collision is assumed between ion of mass M_1 (with an incident energy E_0) and a stationary atom of mass M_2 (which is initially stationary), we can determine the energy transferred from the projectile to the stationary atom using the conservation of energy and momentum. The energy transferred to the atom depends on the scattering angle θ. Conservation of energy and momentum in the center of mass frame give the energy transferred T as [13]:

$$T = E_0 \frac{4M_1M_2}{(M_1+M_2)^2}\sin^2\left(\frac{\theta}{2}\right) = T_{\max}\sin^2\left(\frac{\theta}{2}\right) \tag{3.9}$$

Equation 3.6 shows that during a head-on collision, i.e. $\theta=\pi$, maximum energy is transferred to the target atom.

For an incident ion penetrating through a path length in a target with N atoms per unit volume, the rate of energy loss to nuclear collisions per unit length can be calculated by summing the energy loss multiplied by the probability of a collision happening [4]. If the maximum total energy transferred to the target atoms in a collision is T_{max}, then;

$$S_n = \left(\frac{dE}{dx}\right)_{nuclear} = N\int_0^{T_{\max}} T d\sigma \tag{3.10}$$

3.4 Electronic stopping

Electronic stopping refers to the slowing down of energetic ions due to the inelastic collisions between electrons in the medium and the ions penetrating through it. When ions with high energies (velocity greater than $v_0Z^{2/3}$) penetrate a material, they experience a drag due to free electrons. When an ion passes through an electron cloud, it attracts the electrons and causes internal electronic transitions. The processes for the transfer of kinetic energy from ion to target electrons can include; electron-electron collisions, excitation, ionization or electron capture of the ion etc. [13]. Only those electrons in energy states close to Fermi level are involved in the energy loss.

As seen from Figure 3.2, the stopping power vs ion energy/ion velocity function is divided into three regions where the ion velocity is compared to Bohr velocity in each region i.e.

region I ($v_1 < v_0 Z^{2/3}$), II ($v_1 \approx v_0 Z^{2/3}$) and III ($v_1 >> v_0 Z^{2/3}$) respectively. An hydrogen atom of energy 25 keV is assumed to be moving with the same velocity as its orbital electron, and a helium atom will move at the same velocity as its orbital electrons at 252 keV. Therefore, the ion's initial energy with velocity equal to its orbital velocity, can be written as a product of the ion's mass and its atomic number as:

$$E = Z_1^{4/3} A_1 25 keV \tag{3.11}$$

For europium ions, $v_0 Z^{2/3}$ is $5.51 \times 10^8 m/s$ with v_0 calculated from the Eu initial energy given by equation 3.11. With initial ion energy of 270 *keV*, europium ions have an initial velocity of $5.86 \times 10^5 m/s$, which is less than $v_0 Z^{2/3}$.

3.5 Energy loss in compounds

So far, the stopping cross sections have been discussed for a single elemental material. In this study, a material consisting of more than one element was used, i.e. SiC, the stopping cross sections in compound materials need to be discussed.

The summation of pure element stopping cross sections gives a simplest approximation of the stopping in compound materials. According to Bragg's rule, for a compound material $A_n B_m$ with the elemental stopping cross section S_A and S_B, the stopping cross section can be written as [14]:

$$S_{A_n B_m} = nS_A + mS_B \tag{3.12}$$

where n and m are the relative molar fractions of the compound materials. Depending on the chemical as well as physical state of the material, the energy loss often deviates from Bragg's rule. For example, for oxides and hydrocarbons, deviations of up to 40% are observed with increasing amount of covalent bonding in the compound [14]. Stopping data can be found in the Stopping and Range of Ions in Matter (SRIM) package for a number of compounds [15].

3.6 Energy straggling

An accelerated particle that moves through a medium loses energy through a number of individual encounters, causing statistical fluctuations in the energy. Different reasons exist for energy loss fluctuations, which are partly connected to the statistical nature of the collisions which result in energy loss. Due to these fluctuations, identical energetic particles with the same initial velocity do not possess the same energy after passing through a thickness Δx of the same medium [16]. The energy distribution of an ion beam is broadened after traversing a medium of thickness Δx. This phenomenon is known as energy straggling and is shown in Figure. 3.4;

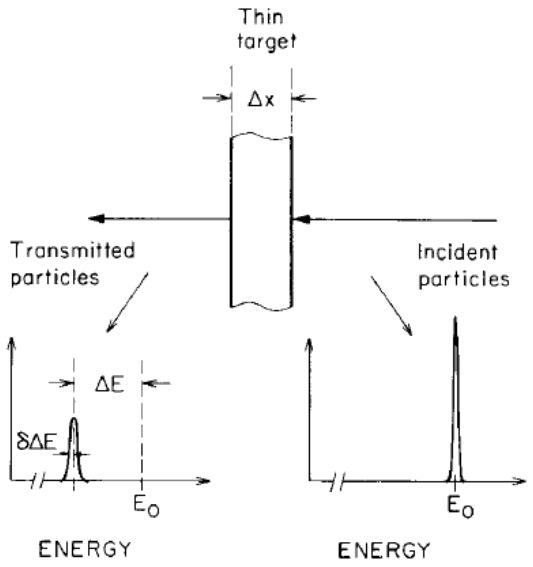

Figure 3.4: *A monoenergetic beam of energy E_0 loses energy ΔE in traversing a thin film of thickness Δx. Simultaneously, energy straggling broadens the energy profile. Taken from reference [16].*

The value Ω_B^2, which is known as the Bohr value of energy straggling, was first derived from the Bethe-Bloch equation for the case of collision between a high velocity ion and an electron of a target medium [17]. For a sheet of thickness $t = \Delta x$, Bohr straggling is given by:

$$\Omega_B^2 = 4\pi\left(Z_1 e^2\right)^2 N Z_2 \Delta x \tag{3.13}$$

where Z_1 is the atomic number of the ion, Z_2 is the atomic number of the target atom and N is the atomic density of the target medium. Equation (3.13) is the variance of the average energy loss of a projectile travelling through a medium of thickness Δx. For an approximately Gaussian distribution, the full width at half maximum (FWHM) of energy loss distribution is

given by $FWHM = 2\Omega_B\sqrt{2\ln 2}$. The Bohr theory has been updated and a correction term has been included for energies where the Bohr assumptions may not be valid [18, 17].

3.7 Range and Range straggling

Range along the ion path is defined as the total distance traversed by the ion along the trajectory within the target [19]. Using equation 3.14, the range calculation which involves the contributions from both ion stopping cross sections(electronic and nuclear stopping) is given as:

$$R = \int_0^R dx = \frac{1}{N}\int_0^{E_0} \frac{dE}{S_n(E) + S_e(E)} \tag{3.14}$$

where N is the number of atoms per unit volume, E_0 is the initial energy of the projectile, S_n and S_e are the nuclear and electronic stopping cross section respectively.

The projected range (R_p) is the average depth of the implanted ions, and can be estimated by the position of the peak height of the Gaussian distribution of the implanted profile. The standard deviation of the distribution of the implanted ions (which can be approximated as Gaussian distribution) gives the so called "range straggle" ΔR_p. An ion penetrating a substrate and finally coming to stop at projected range R_p is illustrated in Figure 3.5.

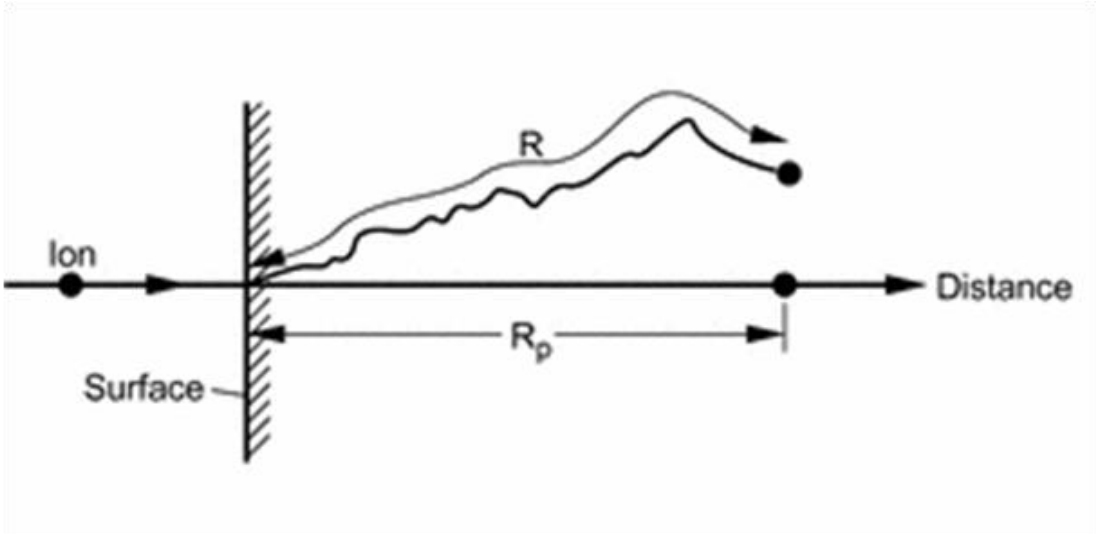

Figure 3.5: *An ion incident on a semiconductor penetrate with a total path length R giving a projected range R_p. Taken from reference [20].*

A Gaussian distribution of Eu ions (270*keV*) implanted into polycrystalline SiC indicating the projected range and the range straggling is shown in Figure 3.6,

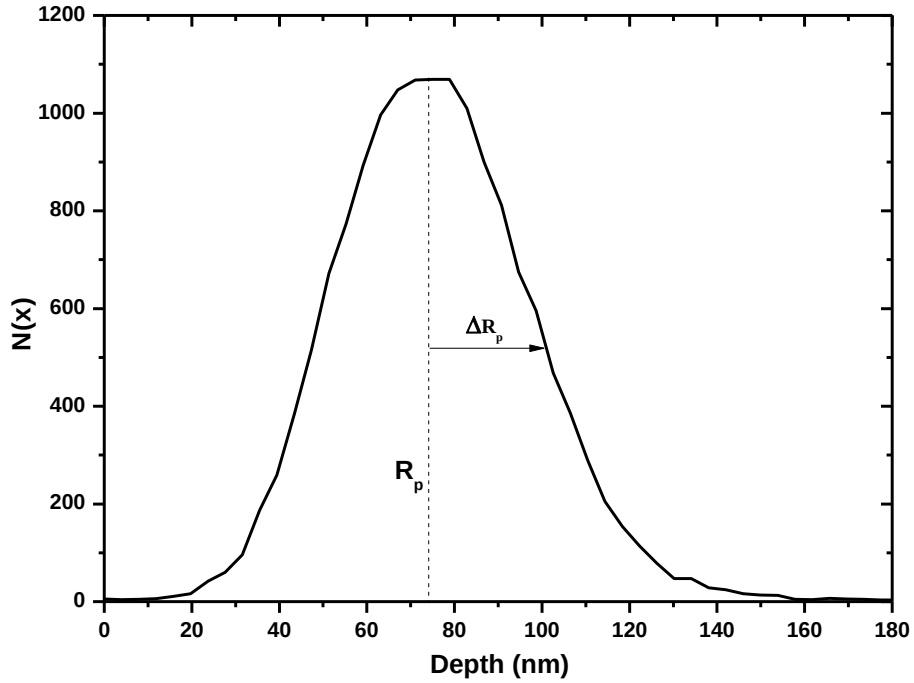

Figure 3.6: *Range distributions for Eu ion implanted into poly-SiC. N(x) is the number of ions and the Depth represents the distance into the solid. The projected range is also indicated in the figure.*

3.8 Simulation of ion implantation

A simulation of ions implanted into a certain material is necessary to predict the shape and depth of the expected profiles. A Monte Carlo computer program is used to calculate the range distributions of a variety of ion/target combinations. In this study a TRIM program was used to simulate implantation of 270 keV Eu ions into both polycrystalline and 6H-SiC. When performing the calculations, TRIM assumes the following:

- That the interaction of ion and target is a binary collision, ignoring the influence of the surrounding atoms.
- Recombination of atoms with vacancies is neglected.
- The interatomic potential as a universal form which is an averaging fit to quantum mechanical calculations using experimental data.

Even with these assumptions in place TRIM still maintains moderate accuracy with a percent error of about 5-10%. Figure. 3.7 shows the TRIM results of a 270 keV Eu ions implanted in polycrystalline SiC, experimental results for a polycrystalline SiC implanted at RT are

included for comparison. Due to the reasons stated above, the actual experimental profile is broader than the simulated profile.

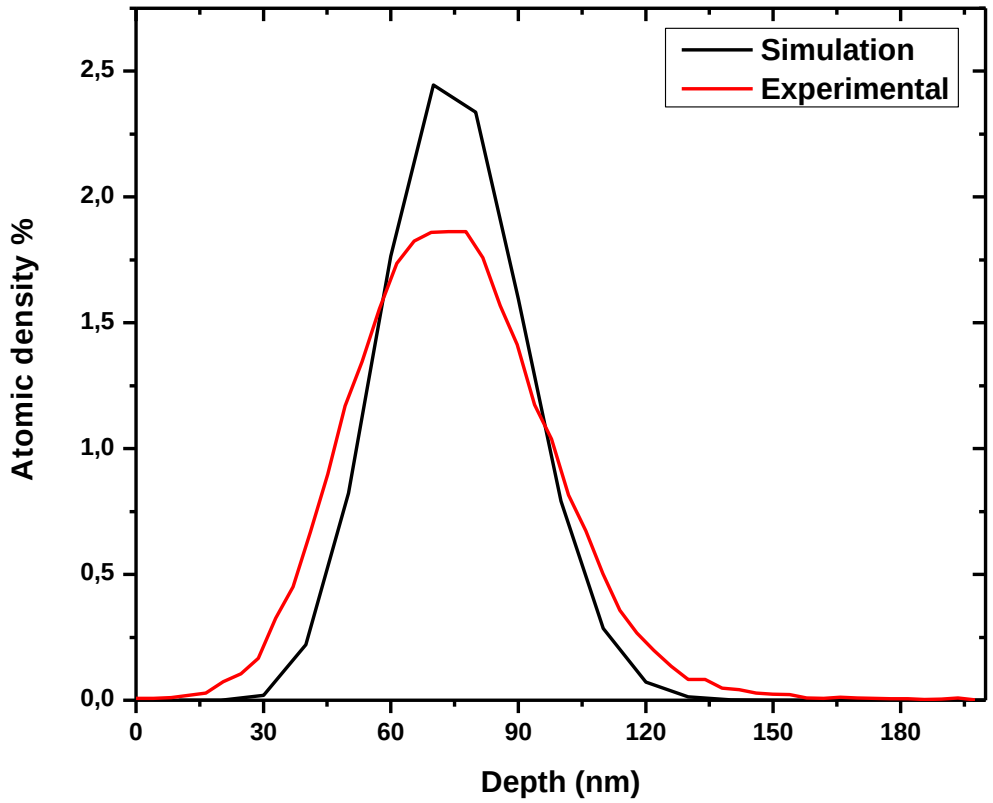

Figure 3.7: *A TRIM simulation of 270 keV Eu ions implanted into SiC, with an experimental profile of Eu implanted in polycrystalline SiC at RT.*

References

[1] Xu, R., Xu, Y. and Huo, Q., 2011. *Modern inorganic synthetic chemistry*. Netherland: Elsevier.

[2] Rubin, L. and Poate, J., 2020. *Ion implantation in silicon technology*. [online] Axcelis.com. Available at: <https://www.axcelis.com/wp-content/uploads/2019/02/Ion_Implantation_in_Silicon_Technology.pdf> [Accessed 10 August 2020].

[3] Muttaqin, A. and Idris, I., 2020. *Implanted layer characterization*. [online] Media.neliti.com. Available at: <https://media.neliti.com/media/publications/59272-EN-implanted-layer-characterization.pdf> [Accessed 10 August 2020].

[4] Cityu.edu.hk. 2020. *CHAPTER 9: Ion implantation*. [online] Available at: <http://www.cityu.edu.hk/phy/appkchu/AP6120/9.PDF> [Accessed 10 August 2020].

[5] Lindhard, J., Scharff, M. and Dan, K., 1953. Stopping power of heavier substances. *Matematisk-fysiske Meddelelserudgivet af Det Kongelige Danske Videnskabernes Selskab*, 33(15), p.128.

[6] Lindhard, J. and Scharff, M., 1961. Energy dissipation by ions in the kev region. *Physical Review*, 124(1), pp.128-130.

[7] Ziegler, J. and Manoyan, J., 1988. The stopping of ions in compounds. *Nuclear Instruments and Methods in Physics Research Section B: Beam Interactions with Materials and Atoms*, 35(3-4), pp.215-228.

[8] Andersen, H. and Ziegler, J. (1977). *Hydrogen*. 1st ed. New York: Pergamon.

[9] Leung, P.T. (1989). Bethe stopping-power theory for heavy-target atoms. *PhysicalReview A*, 40(9), pp.5417-5419.

[10] Kamaratos, E., 1984. The mean excitation energy for stopping power I, the Bragg rule, and chemical and phase effects. Application of a statistical treatment to the determination of I for chemically bound particles. *Chemical Reviews*, 84(6), pp.561-576.

[11] Backman, M., 2020. *Effects of nuclear and electronic stopping power on ion irradiation of silicon-based compounds*. [online] Core.ac.uk. Available at: <https://core.ac.uk/download/pdf/14926238.pdf> [Accessed 11 August 2020].

[12] Gnaser, H., 1999. *Low-energy ion irradiation of solid surfaces*. Berlin: Springer.

[13] Ziegler, J., Littmark, U. and Biersack, J., 1985. *The stopping and range of ions in solids*. New York: Pergamon.

[14] Möller, W., 2021. [online] Hzdr.de. Available at: <https://www.hzdr.de/FWI/GENERAL/Fundam_ISI.pdf> [Accessed 3 January 2021].

[15] Srim.org. 2021. *James Ziegler - SRIM & TRIM*. [online] Available at: <http://www.srim.org/> [Accessed 3 January 2021].

[16] Chu, W., Mayer, J. and Nicolet, M., 1978. *Backscattering spectrometry*. California: Academic Press, INC.

[17] Bohr, N., 1948. The penetration of atomic particles through matter. *Mathematisk-fysiske Meddelelser*, [online] 24(19). Available at: <http://fr2.fisica.edu.uy/vip/BOHR-INT-MATERIA.pdf> [Accessed 17 August 2020].

[18] Lindhard, J., Scharff, M. and SCHIØTT, H., 1963. Range conceptsand heavy ion ranges. *Det Kongelige Danske Videnskabernes Selskab, Matematisk-fysiske Meddelelser*, 33(14).

[19] Tesma, J.R and Nastasi, M. (1995). *Handbook of modern ion beam materials analysis*. 1st ed. Pennsylvania: Materials Research Society, pp.15-16.

[20] Nastasi, M. and Mayer, J.W. (2006). *Ion implantation and synthesis of materials*. 1st ed. Berlin: Spinger, pp.63-76.

CHAPTER 4

ANALYTICAL TECHNIQUES

Several analysis techniques were used in this study, these included; Rutherford backscattering spectrometry (RBS), scanning electron microscopy (SEM), X-ray photoelectron spectroscopy (XPS) and Raman spectroscopy. This chapter discusses the experimental techniques used in this study.

4.1 Rutherford Backscattering Spectrometry (RBS)

RBS is an analytical technique that is used to determine the structure and elemental composition in materials by measuring the backscattered beam of particles impinging the substrate. RBS consists mainly of five parts namely; the accelerator (Van de Graaff generator in this study), the beam line, analysis chamber, the detector and the data acquisition set-up.

4.1.1 The Van de Graaff Accelerator

In this study, helium ions (He^{+}) were produced in an ion source and accelerated to energies of 1.4 and 1.6 M*eV* by a Van De Graaff accelerator. This beam of particles was used in the analysis of polycrystalline SiC and 6H-SiC implanted with Eu ions.

Helium (He) gas is ionized by a radiofrequency (RF) signal. The ionized gas results in a He gas plasma. A positive potential is then applied to the anode. Positive ions from the plasma are then repelled through the exit of the bottle into the acceleration path of the accelerator. A typical RF ion source with electrodes and exit channel is shown in Figure 4.1

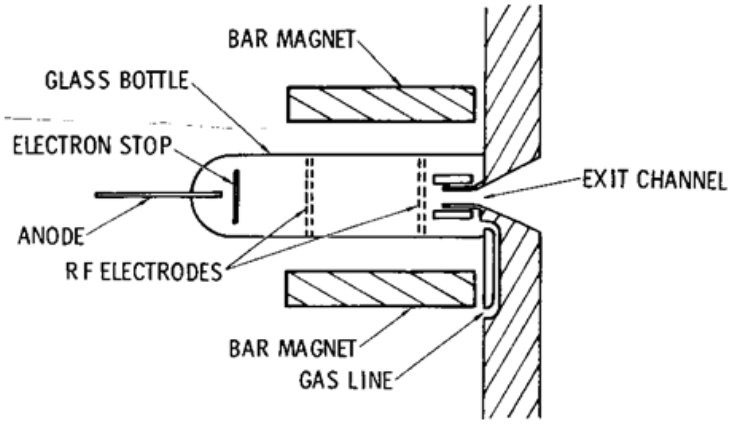

Figure 4.1: *Schematic representation of a RF ion source. Taken from reference [1].*

In a Van de Graaff Accelerator, an insulating belt is driven by a pulley with sharply pointed metal comb which has been given a positive charge (charging screen) by a power supply [2]. Another comb at the top (collection screen) removes the positively charged ions from the belt. The net positive charge thus spread onto the terminal shell. The belt accumulates electric charge on the terminal shell producing high voltage on it. This high potential is used to accelerate the positive ions (He^{+}) in the beam line. Figure 4.2 represents a typical schematic of a Van De Graaff accelerator.

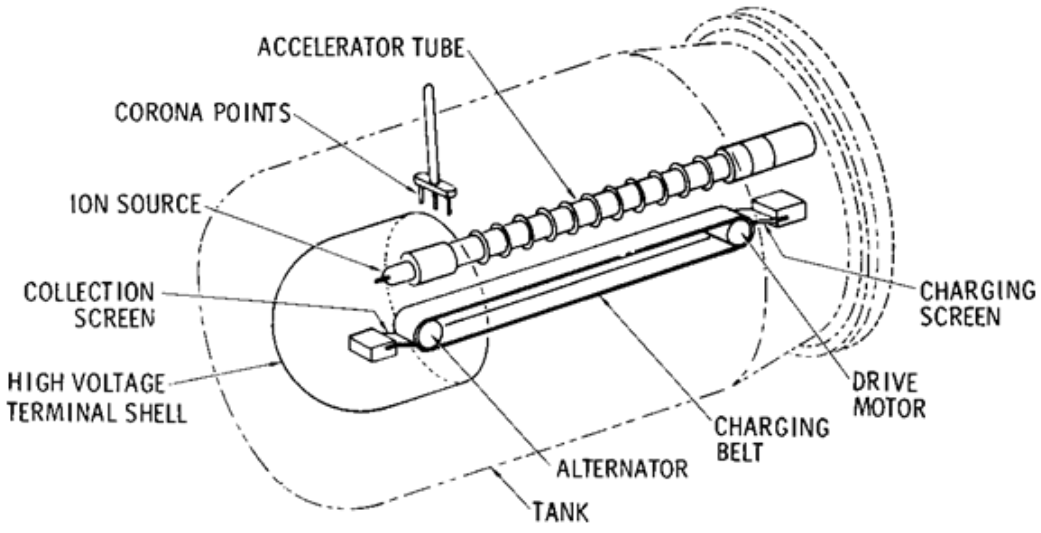

Figure 4.2: *Schematic diagram of a Van De Graaff accelerator. Taken from reference [1].*

The acceleration tube is highly evacuated to normal operating pressures of 10^{-6}*mbar* to minimize collisions between the accelerated ions and the particles inside the tube. The tube pressure in the accelerator used at university of Pretoria (UP) is normally kept at about 10^{-8} mbar. A voltage breakdown can occur if the pressure rises to about 10^{-4} mbar. Both the terminal shell and the accelerating tube are covered by a tank which is normally filled with dry gases such as N_2, CO_2, or SF_6 to prevent sparking of the high voltage to the terminal which is at ground potential [1]. Before filling the tank with the gases, it is first evacuated. A mixture of N_2 and CO_2 was used in the accelerator tube used in this study.

4.1.2 The beam-line

A high-energy beam of ions is accelerated through a beam-line that is maintained at low pressures towards the target material. A vacuum of between 10^{-5} mbar and 10^{-7} mbar is usually sufficient to minimize collision probability between ions and residual gas molecules. The beam-line is kept at 10^{-6} mbar. It is important that the beam have a uniform distribution along the appropriately shaped cross section for the analysis of the sample. The shape of the beam cross section is defined by collimators. They are typically circular holes of diameter ranging from less than 1mm up to 1cm. A 1 mm collimator was used in this study.

4.1.3 Target and analysis chamber

The target is fitted in a chamber and aligned in front of the beam where it can interact with the beam. The chamber is also evacuated to lower pressures of about 10^{-6} mbar. A mechanical pump is used to bring down the pressure in the chamber to about 10^{-2} mbar, which is the starting pressure for the turbo-molecular pump. A turbo pump is then used to pump down to even lower pressures of about 10^{-6} mbar. After analysing the sample, the chamber is vented to the atmospheric pressure.

The beam current is measured directly at the sample. The secondary electrons (from the interactions of the beam with the target) which may falsify the current measurement are suppressed by applying a negative suppression voltage of approximately -100 V on the suppressor plates (located in front of the target).

A controlled beam of ions hit the sample placed in a sample holder at a certain angle (ion incident angle), the incident angle used in this study was 0^o with respect to sample normal. A detector located at a scattering angle of 165^o with respect to the incident angle is used to detect the backscattered ions.

4.1.4 The detector and data acquisition

The RBS available at the UP is fitted with a Si-surface-barrier-solid state detector for the detection of backscattered ions. A typical solid-state detector which uses an Au-surface barrier particle detector is shown in Figure 4.3.

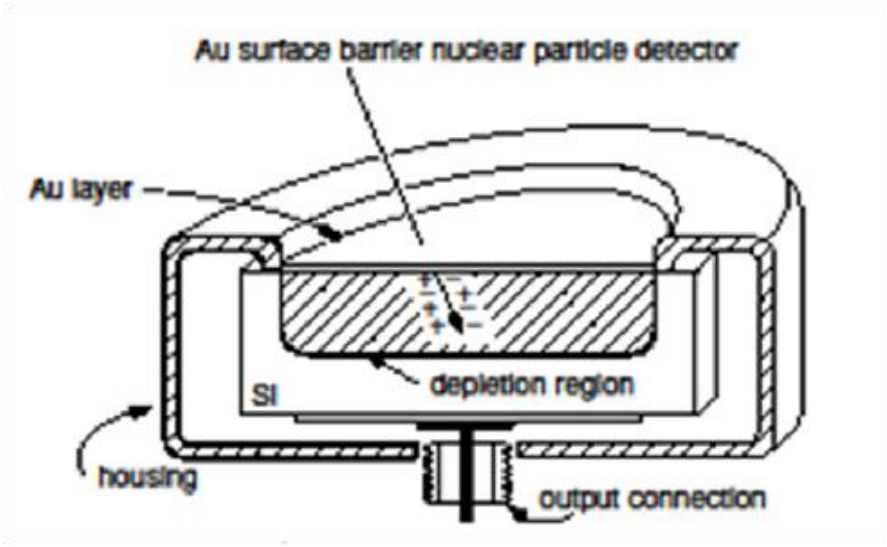

Figure 4.3: *Schematic representation of a gold-surface barrier nuclear particle detector. Taken from reference [3].*

When a backscattered ion with a certain backscattered energy passes through the depletion region, an electron-hole pair are created. The number of electron-hole created is proportional to the energy of the backscattered particle. The electrons-holes are detected by applying the biased voltage of about 40 V to the detector. For each incident ion, a pulse is generated by a preamplifier which is connected to the detector . The height of the pulse is proportional to the energy of the detected particle. The generated pulse is amplified in the amplifier. The amplified analog signal is then digitalized in a multichannel analyser (MCA) [4]. The

digitized data is displayed on a computer screen in XY plane of counts vs channel number, where the counts and channel number are equivalent to concentration and backscattered energy respectively. Figure 4.4 shows a typical RBS spectrum of SiC implanted with Eu. The surface positions of the elements are indicated by arrows.

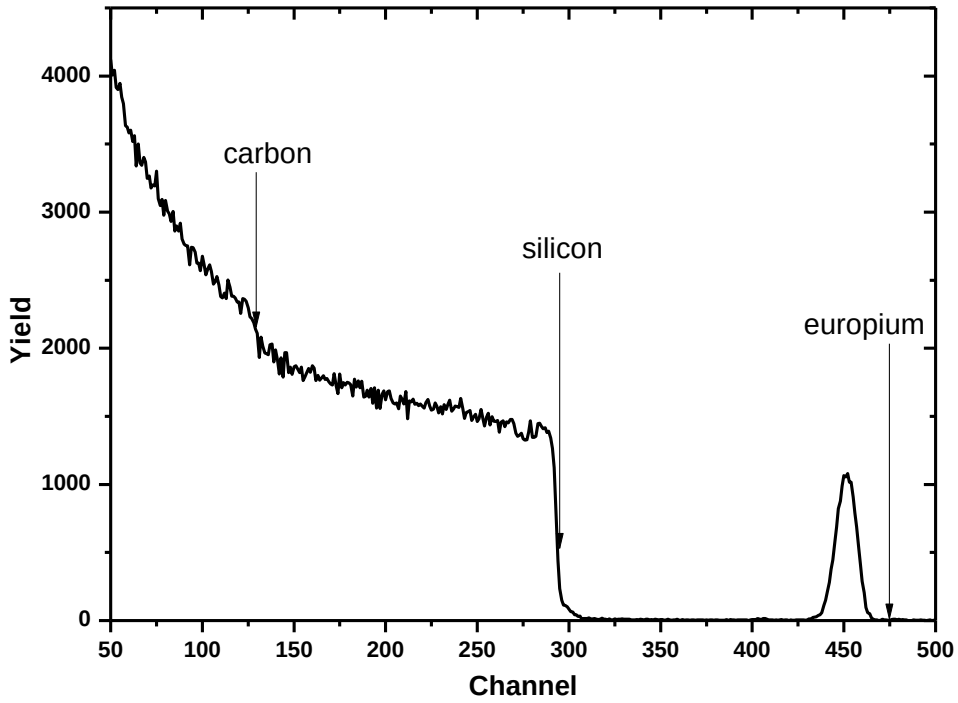

Figure 4.4: *A typical RBS spectrum of polycrystalline SiC implanted with Eu, arrows indicate surface positions of elements.*

4.1.5 The kinematic factor

In RBS analysis, a target is probed by energetic particles (M_1) with initial energy (E_0) and velocity v_0. A collision between the accelerated particles and a stationary target (M_2) occurs, the target atom recoils with energy E_2 and velocity v_2. The projectile backscatters with energy E_1 as shown in Figure 4.5.

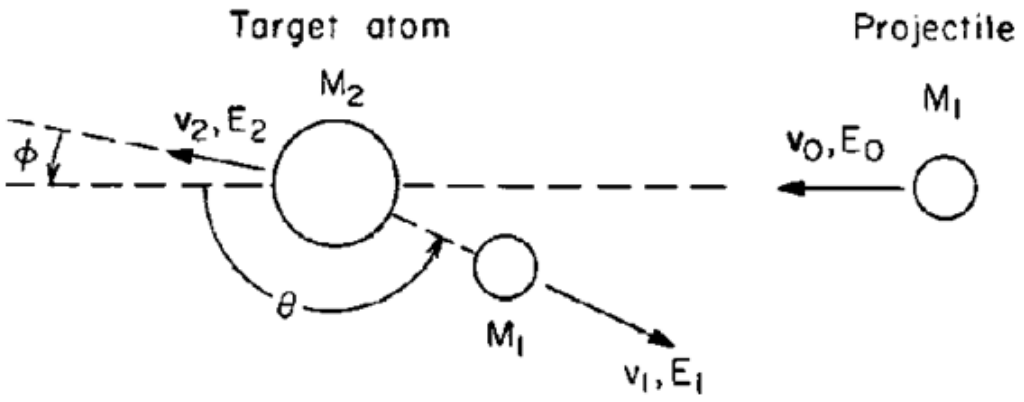

Figure 4.5: *A schematic representation of an elastic collision of a projectile of mass M_1, velocity v_0, incident energy E_0 and a stationary target atom of mass M_2. After the collision the projectile has energy E_1, and velocity v_1, the target atom has energy E_2 and velocity v_2. θ is a backscattering angle. Taken from reference [1].*

The energy of backscattered particle E_1 can be found by applying the principles of conservation of energy and momentum [1]. The ratio of the projectile energy before collision to that of the projectile after collision (backscattered particle) is denoted as the kinematic factor K:

$$E_1 = KE_0 \tag{4.1}$$

Applying conservation of energy and momentum, K is found to be [1]:

$$K = \frac{M_1^{\,2}}{(M_1 + M_2)^2}\left\{\cos\theta \pm \left[\left(\frac{M_2}{M_1}\right)^2 - \sin^2\theta\right]^{1/2}\right\}^2 \tag{4.2}$$

The energy E_1 can be calculated using equation 4.1 for the particles backscattered from known elements. If $M_1 < M_2$ the positive sign is considered in equation 4.2, while there will be two solutions for equation 4.2 if $M_1 > M_2$, and the maximum possible scattering angle θ_{max} would be given by [5]:

$$\theta_{\max} = \arcsin\left(\frac{M_2}{M_1}\right) \tag{4.3}$$

In this study, $M_1 < M_2$ and $\theta = 165^{o}$.

4.1.6 Depth Scaling

Not all incident particles are backscattered from the surface. Some of the particles penetrate the sample, and they lose energy as a result of interactions with various atomic elements comprising the substrate. Some of the penetrating ions backscatter inside the sample after losing some energy and they further lose energy on the way back to the sample surface. Figure 4.6 shows an illustration of such a process.

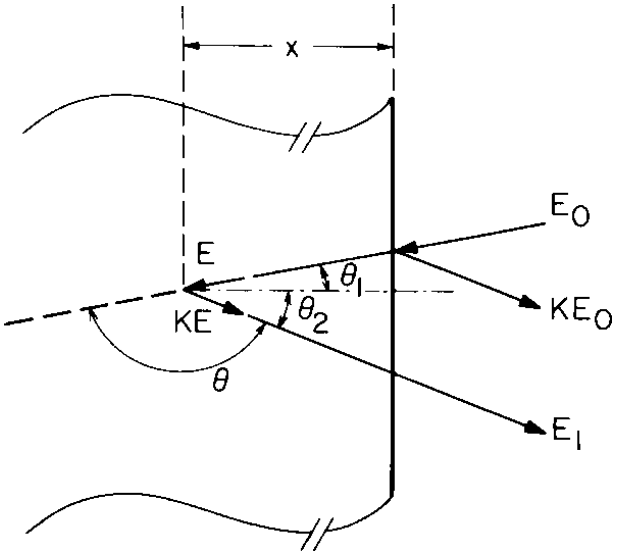

Figure 4.6: *A schematic representation of a backscattering event in a sample consisting of one element, bombarded with particles of energy E_0. Taken from reference [1].*

An ion of initial energy E_0, backscatters on the surface with an energy of KE_o. The penetrating ion loses some of its energy before backscattering at depth x from the surface. The ion has energy E before backscattering at x and has energy KE after backscattering. The particle backscattered at x also lose energy on its way to the surface. E_1 is the energy of the particle emerging from the surface after backscattering at depth x. The scattering angle θ is given by $\theta=180^o- \theta_1- \theta_2$, where θ_1 and θ_2 are the angles between the sample normal and the direction of the incident beam and of the scattered particle, respectively.

The energy difference of a particle backscattered at the surface and a particle backscattered at depth x is denoted by:

$$\Delta E = KE_0 - E_1 \tag{4.4}$$

where KE_0- E_1 is given as a function of x by[1]:

$$\Delta E = KE_0 - E_1 = \left[\frac{K}{\cos\theta_1} \frac{dE}{dx}\bigg|_{in} + \frac{1}{\cos\theta_2} \frac{dE}{dx}\bigg|_{out} \right] x \tag{4.5}$$

$\frac{dE}{dx}\Big|_{in}$ and $\frac{dE}{dx}\Big|_{out}$ are the energy loss values (usually approximated as constant) along the inward and outward paths of the traversing ion. If the energy loss factor in square brackets in equation 4.5 is replaced by S, thus equation 4.5 can be written as:

$$\Delta E = [S]x \tag{4.6}$$

In terms of stopping cross sections, equation 4.6 can be rewritten as:

$$\Delta E = [\varepsilon]Nx \tag{4.7}$$

For a single element material, ε is the stopping cross section factor given by:

$$[\varepsilon] = \left[\frac{K}{\cos\theta_1} \varepsilon_{in} + \frac{1}{\cos\theta_2} \varepsilon_{out} \right] \tag{4.8}$$

For a material consisting of more than one element i.e. A_mB_n, a stopping cross section factor is given by Bragg's rule:

$$\varepsilon_{AB} = m\varepsilon_A + n\varepsilon_B \tag{4.9}$$

Consequently, the total energy loss is given by:

$$\Delta E_{AB} = \varepsilon_{AB} Nx \tag{4.10}$$

where N is the molar density.

4.1.7 Differential cross section

A differential cross section explains the likelihood of a backscattering event to occur. The probability of a backscattering event to occur for an elastic collision in the laboratory frame of reference is given as [1]:

$$\frac{d\sigma}{d\Omega} = \left(\frac{Z_1 Z_2 e^2}{4E} \right)^2 \frac{4}{\sin^2 \theta} \frac{\left\{ \left[1 - \left((M_1 / M_2) \sin \theta \right)^2 \right]^{1/2} + \cos \theta \right\}^2}{\left[1 - \left((M_1 / M_2) \sin \theta \right)^2 \right]^{1/2}} \tag{4.11}$$

where Z_1 is the atomic number of the incident atom with mass M_1, Z_2 is the atomic number of the target atom with mass M_2, e is the electronic charge and E is the energy of projectile ion. The direct proportionality of $d\sigma/d\Omega$ to Z_1 and Z_2 explains the higher sensitivity of the Rutherford backscattering spectrometry to elements with larger mass than for the ones with smaller mass. The inverse proportionality of $d\sigma/d\Omega$ to the square of the projectile energy E^2 explains the higher backscattering yield for ions backscattering with low energy than for high energy ions.

The total number of detected particles can be written as:

$$A = \sigma \Omega Q N t \tag{4.12}$$

where Ω is a solid angle, Q is the total number of incident particles, Nt is the number of target atoms per unit area perpendicular to the beam and σ is the differential cross section. If we know σ and Ω, we can determine the number of atoms per unit area in the target.

4.2 Scanning Electron Microscopy (SEM)

SEM was used to monitor the changes in sample's surfaces before implanted, after implantation and annealing. SEM is a technique used to generate surface images of specimen by scanning the sample surface with a beam of electrons in the x- and y-directions along the sample plane. The main components found in a typical SEM are shown in Figure 4.7.

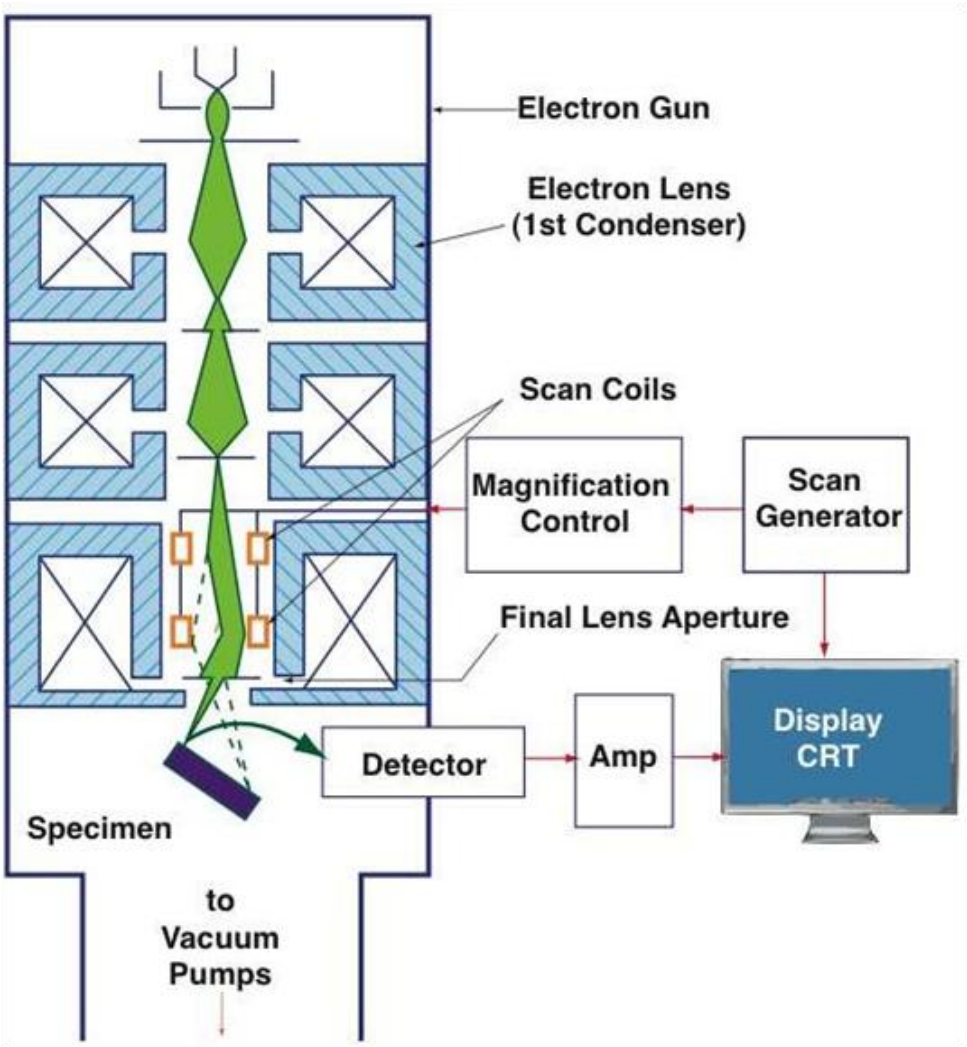

Figure 4.7: *Schematic representation of scanning electron microscopy. Taken from reference [7].*

Free electrons are generated in the electron gun and accelerated to energies in the range of 1-40 *keV*. An electron beam of energy 2 *keV* was used in all measurements in this study. The electromagnetic lenses create a small focused electron spot on the sample. The scanning coils scan the electron beam across the surface of the sample and focuses it into a fine spot to produce images. The electron column environment is evacuated to allow the electron beam to travel freely, minimizing interactions with the gaseous molecules that are present at pressures close to atmospheric pressure.

When a sample is bombarded with electrons, different signals are emitted in the form of electromagnetic radiation as shown in Figure 4.8. These signals, mostly the secondary electrons (SE) and backscattered electrons (BSE), are collected by detectors and amplified for final display on a computer screen. Secondary electrons (SE) are low energy electrons with

energy of approximately 5 *eV* [7], they are weakly bonded electrons ejected from the surface of the sample as a result of inelastic scattering interactions of the incident electron beam. Backscattered electrons (BSE) are high energy electrons of energies approximately the same as the energy of the incident electrons [7]. These electrons result from collisions with atoms in the specimen. BSE and SE can be used for image formation. SE images show mainly the topography of the sample surface, and BSEs are used to obtain elemental contrast imaging, their signal intensity increases with increasing atomic number in the sample. Therefore, heavy elements appear brighter than lighter elements in the image. Auger electrons are ejected from atoms as a result of a downward transition by an electron from higher energy state to lower energy state. The downward transition results in an emitted photon or an X-ray signal. These signals can be used for chemical analyses of the sample (e.g. the composition of the sample, etc).

The electron lenses in SEM are used to produce a uniform electron beam with desired diameter and to limit the amount of current in the beam. The final lens aperture controls the aberrations and the resolution of the image. The detector detects the radiation signals emitted during interaction of electron beam with the sample. Figure 4.9 shows the types of signals emitted during interaction of electron with specimen in SEM.

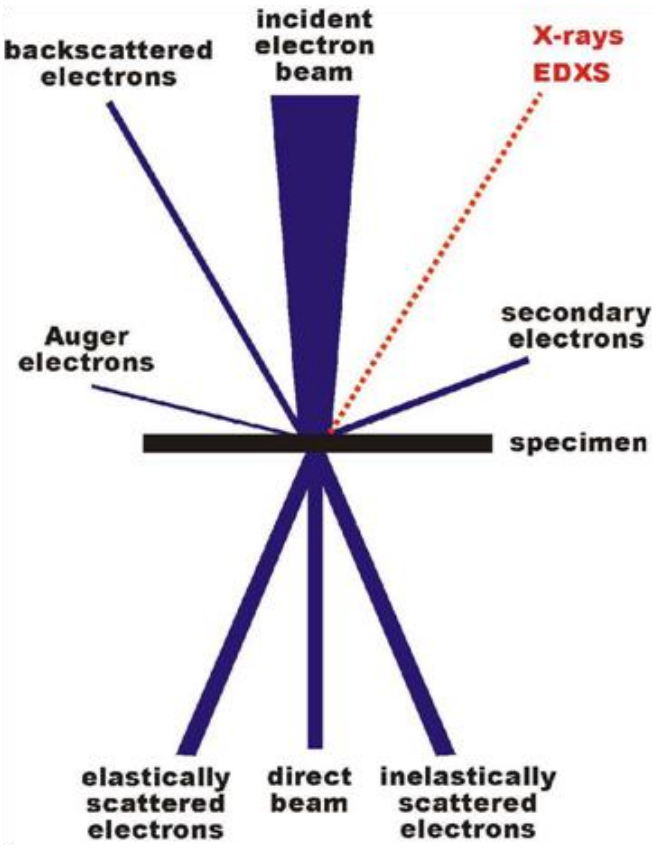

Figure 4.8: *Schematic of electron-matter interactions arising from the impact of an electron beam onto a sample. Taken from reference [8].*

A field emission scanning electron microscope (FEG-SEM) was utilized in this study. This microscope is a Zeiss Ultra 55 fitted with SE (secondary electron), BSE (backscattered electron) and an in-lens detectors. The in-lens detector detects the secondary electrons and BSE, due to its high surface sensitivity, it is used to obtain high resolution images. The in-lens SE detector was used for the analysis of the samples and the results are reported in the results chapter.

The image details and resolution in the SEM are determined by the size and characteristics of the interaction volume. The electron beam interacts and penetrates the sample to a depth determined by the electron energy. The elastic scattering (no loss of energy of the incident electrons) and inelastic scattering (loss of energy of the incident electrons due to electron interaction within the sample) of electrons control the penetrating depth of the electron beam in the solid. This forms an interaction volume from which different signals emerge. A schematic of an interaction volume is shown in Figure 4.9.

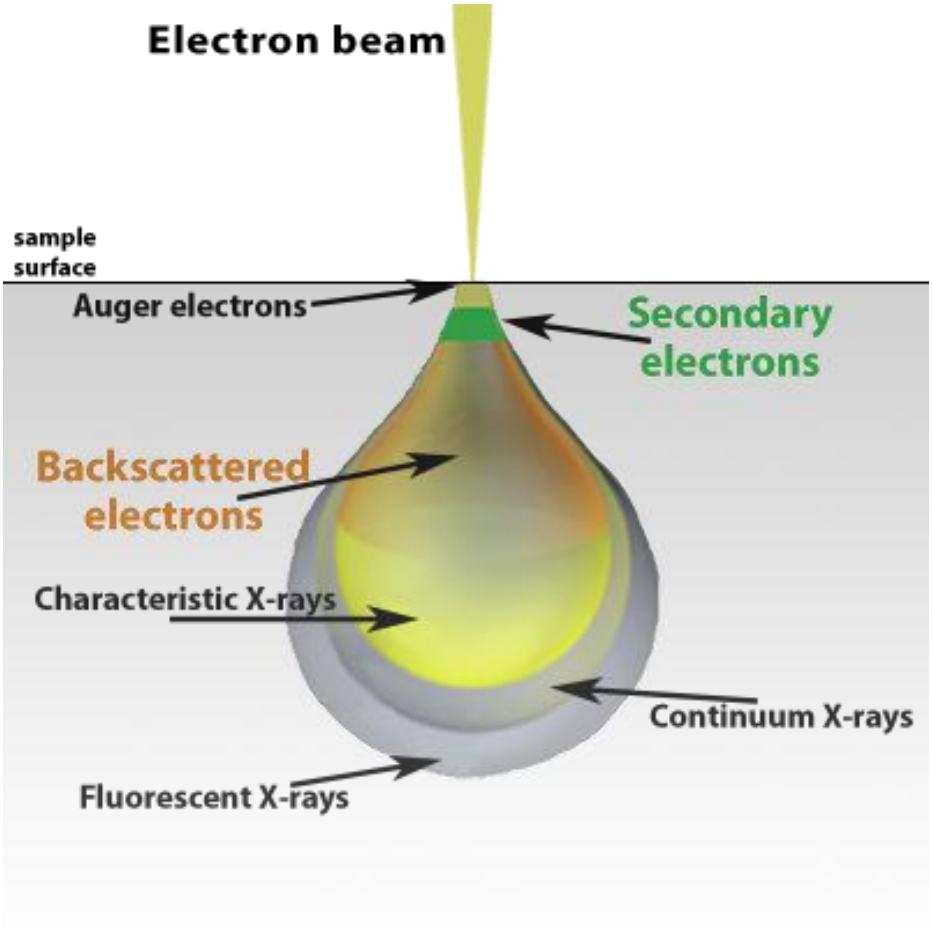

Figure 4.9: *A schematic diagram of a beam interaction with sample and the corresponding emitted signals at different depths. Taken from reference [9].*

The interaction volume determines the nature of imaging in SEM. It increases with increasing energy of electron beam and decreases with atomic number of the atoms in the sample. Samples are required to be clean and compatible with high vacuum environment. This is necessary since SEM operates in a high vacuum (~ $10^{-5}mbar$) environment.

4.3 Raman Spectroscopy

Raman spectroscopy is a non-destructive analysis technique that provides detailed information about molecular structure and the bonding nature of materials. When light interacts with matter, the oscillatory electromagnetic field of the light perturbs the charge distribution in matter leading to an exchange of energy and momentum [10]. This usually leaves matter in a modified state. Electronic excitations, molecular/rotational-vibrations and

optical phonons in liquids, gases and solids are examples of modified state of matter [11]. When an incident photon interacts with matter, it can either be scattered elastically or inelastically. The scattering process is referred to as Rayleigh scattering when light is scattered elastically while the inelastic scattering of light by matter is referred to as Raman effect [12, 13, 14].

The following equation is used to describe the shift in angular frequency of scattered light [10]:

$$\omega_{scat} = \omega_p \pm \omega_{osc} \tag{4.13}$$

where ω_{scat} denotes the frequency of the scattered light, ω_p is the frequency of the incident photon, ω_{osc} denotes the lattice or molecular vibration frequency and (±) denotes the lower and higher frequency shift and is determined by energy conservation [10].

When the energy of the scattered photons is lower than the energy of the incident photon, the process is called Stokes Raman scattering and when the energy of the scattered photon is higher than that of incident photon, it is known as anti-Stokes Raman scattering. The conservation of momentum in a wave vector form is expressed as [10]:

$$\bar{k}_{scat} = \bar{k}_p \pm \bar{q} \tag{4.14}$$

where $\bar{k}_{scat}$, $\bar{k}_p$ and $\bar{q}$ are the wave vectors of the scattered light, the incident light and the phonon or molecular vibration, respectively.

The theory of classical electrodynamics states that the existence of the Raman effect is associated with the modulation of the polarizability (for molecular vibrations/rotations) or di-electric susceptibility (for crystal lattice vibrations) due to the oscillatory nature of inter-atomic displacement [14, 15]. The polarization vector of the material $\bar{P}$, for crystal lattice vibrations is described as [10,16]:

$$P_j^{(1)} = \varepsilon_0 \chi_{jk}^{(1)} E_k \tag{4.15}$$

where ε_0 is the permittivity of free space, χ_{jk} is the dielectric susceptibility of the material, the superscript (1) signifies the first-order contribution to polarization [10]. The subscript j and k represent the vector components in the *x*, *y* and *z* directions, and the j^{th} component of $\bar{P}$ is related to the electric field vector $\bar{E}$ of the light by equation (4.15).

The polarizability tensor is a function of the nuclear coordinates, which means that it will depend on the rotational/vibrational frequency. With respect to the coordinates of vibration, the dependence can be expressed in a Taylor series, if one assumes the modulation to be small, equation 4.16 is obtained [10]:

$$\chi_{jk}^{(1)}\left(\bar{k}_p,\omega_p\right)=\chi_{jk}^{(1)}\left(\bar{k}_p,\omega_p\right)_{\bar{u}=0}+u_l\left(\frac{\partial\chi_{jk}^{(1)}\left(\bar{k}_p,\omega_p\right)}{\partial u_l}\right)_{\bar{u}=0} + u_l u_m\left(\frac{\partial^2\chi_{jk}^{(1)}\left(\bar{k}_p,\omega_p\right)}{\partial u_l\partial u_m}\right)_{\bar{u}=0}+\ldots, \tag{4.16}$$

where $\bar{u}$ is the nuclear displacement vector, *j*, *k*, *l* and *m* represent spatial coordinates with repeated indices in any of the terms implying the summation of the coordinates of that specific index.

If the electric field associated with the light is written as [10]:

$$\bar{E}\left(\bar{r},t\right)=\bar{E}\left(\bar{k}_p;\omega_p\right)\cos\left(\bar{k}_p\bullet\bar{r}-\omega_p t\right) \tag{4.17}$$

and the nuclear displacement written as:

$$\bar{u}\left(\bar{r},t\right)=\bar{u}\left(\bar{q},\omega_{osc}\right)\cos\left(\bar{q}\bullet\bar{r}-\omega_{osc}t\right) \tag{4.18}$$

an explicit expression for time dependence of $P_j^{(1)}$ can be found with the two equations of monochromatic light and displacement. The term which pertains to the first-order Raman scattering is given in equation (4.19), the details of the derivation can be found in [10]:

$$P_j\left(\bar{r},t,\bar{u}\right)=\frac{1}{2}\varepsilon_0\left(\frac{\partial\chi_{jk}{}^{(1)}\left(\bar{k}_p,\omega_p\right)}{\partial u_l}\right)_{\bar{u}=0}u_l\left(\bar{q},\omega_{osc}\right)E_k\left(\bar{k}_p,\omega_p\right) \times\left\{\cos\left[\left(\bar{k}_p+\bar{q}\right)\bullet\bar{r}-\left(\omega_p+\omega_{osc}\right)t\right]+\cos\left[\left(\bar{k}_p-\bar{q}\right)\bullet\bar{r}-\left(\omega_p-\omega_{osc}\right)t\right]\right\} \tag{4.19}$$

The anti-Stokes and Stokes frequencies are contained in the term (equation 4.19).

The quantum mechanics theory approach of the Raman process states that the rotational /vibrational energy of the molecules are discrete quanta (quantized).

Raman scattering is generally considered a very weak process, it is estimated that only one in every 10^8 phonons is estimated to undergo Raman scattering spontaneously [14]. The weakness of the process limits the intensity of the obtainable Raman signal. Surface-Enhanced Raman scattering proposed two mechanisms to explain the increase in Raman

signal. The first mechanism is the electromagnetic enhancements which can increase Raman generation by a factor of 10^8 to 10^{11} [17, 18 - 21]. The second one is chemical enhancement which can enhance Raman scattering by a factor of 10^2 to 10^3 [17, 22 - 24].

4.4 X-Ray photoelectron spectroscopy

X-ray photoelectron spectroscopy (XPS) is a surface analysis technique that is used on a variety of materials to give important information about the quantitative and chemical state of materials. An XPS instrument can achieve an average depth of analysis of about 5 nm [25], hence it is a good technique for the identification of surface elemental composition and also on ultra-thin layers [25]. In XPS analysis, the sample is illuminated with X-rays that have enough energy to excite and eject an electron from the atom as shown in Figure 4.10. The ejected electrons are commonly known as photo electrons, hence X-ray photoelectron spectroscopy. The electrons emitted from the sample have a certain kinetic energy, this particular energy carries the characteristics of a particular element from which the photoelectron originated on the sample.

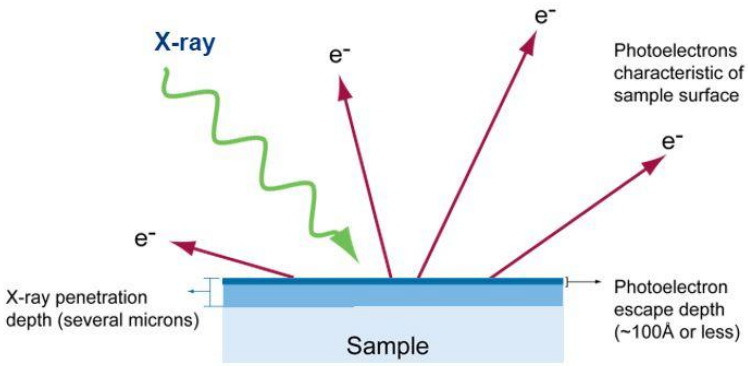

Figure 4.10: *A schematic representation of XPS process with X-rays penetrating the sample and forcing electrons out from the sample. Taken from reference [26].*

The binding energy (BE) of a photoelectron is affected by the chemical environment of an atom which results in a change in the kinetic energy (KE) measured. The following equation relates the BE to the KE of the photoelectron [27]:

$$BE = h\upsilon - KE \tag{4.20}$$

where h is Plank's constant and υ is the frequency of the radiation (Hz), thus hυ is the photon (X-ray) energy. The chemical/bonding information of the elements is obtained from the chemical shifts (changes in measured KE). The position (BE in (eV)) and the intensity (number of electrons) of the peaks in an XPS energy spectrum provides the chemical state and quantitative information about the elements on the surface.

The X-ray excitation sources that are commonly used includes Al Kα (1486,6 eV) and Mg Kα (1253,6 eV) [28]. However, an interest in using higher energy X-ray excitation sources has recently grown with excitation sources such as Ag Lα (2984,2 eV), Cr Kα (5414,9 eV) or Ga (9252 eV) [27].

Reference

[1] Chu, W., Mayer, J.W. and Nicolet, M.A. (1978). *Backscattering spectrometry*. 1st ed. New York: Academic Press.

[2] Hyperphysics.phy-astr.gsu.edu. n.d. *Van De Graaff Generator*. [online] Available at: <http://hyperphysics.phy-astr.gsu.edu/hbase/electric/vandeg.html> [Accessed 6 September 2020].

[3] Alford, T.L., Feldman, L.C. and Mayer, J.W. (2007). *Fundamentals of nanoscale film analysis*. 1st ed. New York City: Springer, p.15.

[4] Pászti, F., Kótai, A. and Fazinic, S. (2000). Instrumentation for pixe and rbs. *International Atomic Energy Agency*.

[5] Mayer, M. (2003). *Rutherford backscattering spectrometry (RBS)*.

[6] Hyperphysics.phy-astr.gsu.edu. n.d. *Van De Graaff Generator*. [online] Available at: <http://hyperphysics.phy-astr.gsu.edu/hbase/electric/vandeg.html> [Accessed 6 September 2020].

[7] Sameer, G., 2016. *Introduction of scanning electron microscope*. [online] Available at: <https://www.researchgate.net/publication/318819221_Introduction_of_Scanning_Electron_Microscope> [Accessed 6 September 2020].

[8] Krumeich, F., n.d. *Properties of electrons, their interactions with matter and applications in electron microscopy*. [online] Microscopy.ethz.ch. Available at: <https://www.microscopy.ethz.ch/downloads/Interactions.pdf> [Accessed 6 September 2020].

[9] Nanoscience Instruments. n.d. *Components in a SEM - nanoscience instruments*. [online] Available at: <https://www.nanoscience.com/techniques/scanning-electron-microscopy/components/> [Accessed 6 September 2020].

[10] Jones, R., Hooper, D., Zhang, L., Wolverson, D. and Valev, V., 2019. Raman techniques: Fundamentals and frontiers. *Nanoscale Research Letters*, 14(1).

[11] DeCusatis, C., Enoch, J., Lakshminarayanan, V., Li, G., MacDonald, C., Mahajan, V. and Stryland, E., 2009. *Handbook of optics, third edition volume IV*. McGraw-Hill Publishing.

[12] Long, D., 2002. *The Raman effect*. Chichester: Wiley.

[13] Das, R. S. and Agrawal, Y. K., 2011. Raman spectroscopy: Recent advancements, techniques and applications. *Vibrational Spectroscopy*, 57(2), pp.163-176.

[14] Gardiner, D., Graves, P. and Bowley, H., 1989. *Practical Raman spectroscopy*. Berlin: Springer-Vlg.

[15] Wolverson, D 2008, Raman Spectroscopy. in C Lamberti (ed.), *Characterization of semiconductor heterostructures and nanostructures*. Elsevier, Amsterdam, pp. 249-288

[16] Boyd, R., 2003. *Nonlinear optics*. Elsevier.

[17] Verma, P., 2017. Tip-Enhanced Raman spectroscopy: Technique and recent advances. *Chemical Reviews*, 117(9), pp.6447-6466.

[18] McFarland, A., Young, M., Dieringer, J. and Van Duyne, R., 2005. Wavelength-scanned surface-enhanced raman excitation spectroscopy. *The Journal of Physical Chemistry B*, 109(22), pp.11279-11285.

[19] Metiu, H. and Das, P., 1984. The electromagnetic theory of surface enhanced spectroscopy. *Annual Review of Physical Chemistry*, 35(1), pp.507-536.

[20] Xu, H., Bjerneld, E., Käll, M. and Börjesson, L., 1999. Spectroscopy of single hemoglobin molecules by surface enhanced raman scattering. *Physical Review Letters*, 83(21), pp.4357-4360.

[21] Moskovits, M., 1985. Surface-enhanced spectroscopy. *Reviews of Modern Physics*, 57(3), pp.783-826.

[22] Osawa, M., Matsuda, N., Yoshii, K. and Uchida, I., 1994. Charge transfer resonance Raman process in surface-enhanced Raman scattering from p-aminothiophenol adsorbed on silver: Herzberg-Teller contribution. *The Journal of Physical Chemistry*, 98(48), pp.12702-12707.

[23] Otto, A., Mrozek, I., Grabhorn, H. and Akemann, W., 1992. Surface-enhanced Raman scattering. *Journal of Physics: Condensed Matter*, 4(5), pp.1143-1212.

[24] Xia, L., Chen, M., Zhao, X., Zhang, Z., Xia, J., Xu, H. and Sun, M., 2014. Visualized method of chemical enhancement mechanism on SERS and TERS. *Journal of Raman Spectroscopy*, 45(7), pp.533-540.

[25] Phi.com. 2020. *X-Ray photoelectron spectroscopy (XPS) surface analysis technique*. [online] Available at: <https://www.phi.com/surface-analysis-techniques/xps-esca.html> [Accessed 23 September 2020].

[26] EAG Laboratories. 2020. *XPS Spectroscopy | X-Ray Photoelectron Spectroscopy | XPS-ESCA*. [online] Available at: <https://www.eag.com/techniques/spectroscopy/x-ray-photoelectron-spectroscopy-xps-esca/> [Accessed 13 October 2020].

[27] Kratos.com. n.d. *X-Ray photoelectron spectroscopy (XPS) - The Technique In Brief*. [online] Available at: <https://www.kratos.com/applications/techniques/x-ray-photoelectron-spectroscopy> [Accessed 23 September 2020].

[28] Aif.ncsu.edu. 2016. [online] Available at: <https://www.aif.ncsu.edu/wp-content/uploads/sites/25/2016/07/XPS-Technique-Descriotion-071216.pdf> [Accessed 23 September 2020].

Chapter 5

Methodology

This chapter outlines the experimental procedure from implantation of the samples to analysis. A clear procedure on sample preparation, cutting of samples annealing and analysing is given together with all parameters and specifications.

5.1 Implantation of samples

A set of single crystalline silicon carbide (6H-SiC) wafers and polycrystalline SiC wafers from Valley design Corporation, USA, were used as substrates in this study. The Eu ions of 270 keV energy were implanted separately to a fluence of 1×10^{16} cm^{-2} at room temperature (RT), 350 ^{o}C and 600 ^{o}C. Implantations were performed at the Institut fur Festkorperphysik, Friedrich-Schiller-Universitat, Jena, Germany. During implantations, the 6H-SiC wafers were tilted 7^{o} relative to the normal incident to prevent ion channelling and the flux was kept below
10^{13} $cm^{-2}s^{-1}$ to reduce the possibility of annealing of radiation damage during implantation. The wafers were cleaned in acetone and then deionised water, this was done before and after implantation with Eu.

The implanted specimens were cut into 1 cm × 1 cm pieces to allow for analysis withRBS and SEM. A diamond scriber with diamond tip was used as a cutting tool for the samples [1].

To remove any possible contamination during the handling and cutting of samples, the samples were cleaned in acetone followed by deionised water in a ultrasonic shaker for 10 minutes in each cleaning agent. After ultrasonic rinse with water the samples were dried in an oven at 100 ^{o}C for 1 hour to remove any water molecules/particles from the sample. Some of the implanted samples were then annealed.

5.2 Annealing system

The cleaned samples were placed in a glassy carbon crucible and annealed in a computer-controlled high temperature vacuum graphite furnace Webb 77.

5.2.1 Webb 77 Graphite furnace

The Webb furnace is capable of reaching a maximum temperature of about 2000 ^{o}C. The temperature in the oven is controlled by a Eurotherm 2704 controller, which is connected to two temperature reading devices. (1) The thermocouple which is used for temperature readings below 1475 ^{o}C and (2) a pyrometer which reads temperatures above 1525 ^{o}C [2]. In between the two temperatures (1475 and 1525 ^{o}C), the average of the two readings from the two readers is taken. The accuracy of temperature reading in this oven is ± 15 ^{o}C.

The sample was put inside a graphite crucible with a lid on top and then loaded into the oven. This was done in every annealing cycle, and the reason for that is to avoid the contamination of the annealed sample by other elemental residues that may be stuck in the furnace walls. This kind of contamination is very possible since the furnace is used by many researchers for different studies with different samples.The oven was always evacuated to lower pressure of about 10^{-6} mbar after loading the sample. The oven was then degassed at 100 °C for 3 hours before starting with the annealing process. This ensures that the maximum pressure during annealing is kept at 10^{-5} mbar and the pumping time is reduced.

During the heating process the vacuum pressure increases from 10^{-6} to 10^{-5} mbar. The heating rate of this machine was kept at around 20 °C/min. The heating element heats up to a selected temperature level and then stays there for 5 hours. At the end of the annealing duration, the current is switched off and the system cools down. The vacuum is brought down by switching off the turbo pump and then the vacuum is finally broken completely by letting argon gas into the chamber to bring the pressure to atmospheric pressure. A sample is removed and then analyzed. A typical heating/cooling curve of the furnace for the 5 hours annealing time at a temperature of 1100 ^{o}C is presented in Figure. 5.1.

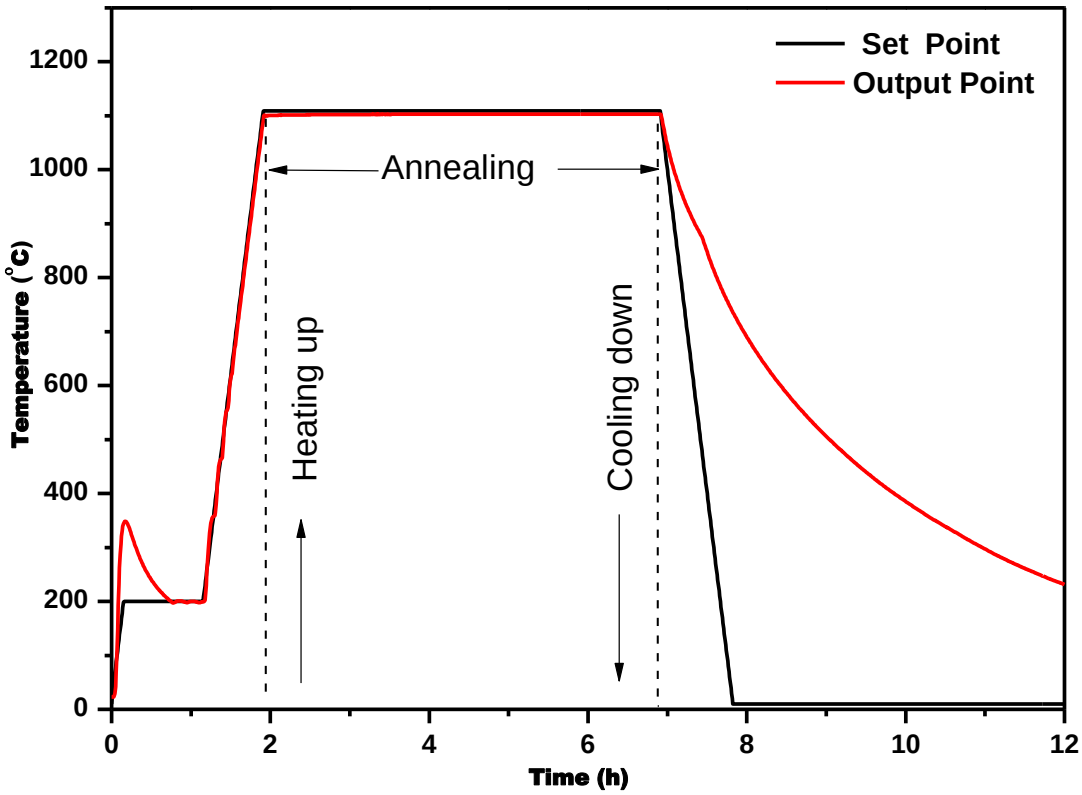

Figure 5.1: *Heating and cooling curves for the annealing process at 1100 ^{o}C for 5 hours. The black curve represents the heating and cooling of the simulation program used in the annealing system and the red curve represents the heating and cooling of the furnace as read by the thermocouple.*

The cooling of the oven can be described mathematically by the following equation from Newton's cooling law [3]:

$$T(t) = F\exp(-Zt) \tag{5.1}$$

where T is the temperature, t is the time and F and Z are constants. The differentiation of the above equation with respect to time gives the cooling rate, and can be written as:

$$\frac{dT}{dt} = -FZ\exp(-Zt) \tag{5.2}$$

5.3 Rutherford backscattering spectrometry (RBS) Analysis

The RBS profiles of Eu implanted in SiC were obtained at room temperature by production of a collimated beam of particles with energy of 1.4 and 1.6 MeV at a scattering angle of 165^{o} using the accelerator at UP. The analysing beam was collimated to a spot of 1mm in diameter and the current was kept below 15 nA to avoid pile-up and over-heating of the target sample. To suppress secondary electrons, an electrode was kept at a negative potential of 100 V in front of the target. An integrated charge of 8 μC was collected to ensure sufficient counting statistics.

A surface barrier detector telescope was placed at a scattering angle of 165^{o} for the detection of backscattered particles. The spectra were collected during rotation of the sample about an axis tilted by approximately 5^{o} relative to the channelling direction. The backscattered energy in channels were converted into depth (in nm) using the energy loss data and the density of pristine SiC i.e. 3.21 $g.cm^{-3}$.

5.4 Scanning electron microscopy (SEM) Analysis

The sample's surface morphological changes were monitored before and after implantation as well as before and after every annealing step using a field emission scanning electron microscopy (FEG-SEM) employing a Zeiss Ultra 55 instrument fitted with in-lens detector. An analysing electron beam of 2 keV energy was used. The beam was focused on different areas of the sample to check the uniformity of the features on the sample. Images were recorded at low and high magnifications.

5.5 Raman Analysis

The structural changes were monitored by Raman spectroscopy, T64000 series II triple spectrometer system from HORIBA scientific, Jobin Yvon Technology, using a 514.5 nm laser line of coherent Innova 70C series Ar^{+} laser (spot size ~ 2mm) at a power of 1.7 mW with resolution of 2 cm^{-1}. The spectra were recorded in the 200 to 1800 cm^{-1} range. The Raman analysis was performed after every annealing cycle, including the as-implanted and the un-implanted samples. The laser beam was focused on the samples through the

magnifying objective lens. Measurements were performed in a dark room with tinted windows to avoid interference of the beam with light coming from outside.

5.6 X-ray photoelectron spectrometer (XPS) analysis

The elements/compounds present on the surface of the sample after annealing at 1000 ^{o}C were identified using X-ray photoelectron spectrometer (XPS). The XPS measurements were performed at Joint Institute for Nuclear Research (JINR), Dubna, Russia using an X-ray excitation source; Thermo SCIENTIFIC K- Alpha X-ray photoelectron spectrometer with monochromatic Al-Kα radiation.

References

[1] Diamond Tip Scribers, S., 2020. *About Us*. [online] Thomassci.com. Available at: <https://www.thomassci.com/scientific-supplies/Diamond-Tip-Scriber> [Accessed 30 September 2020].

[2] R.D. Webb Conpacy, operating manual Webb 77. 2006.

[3] Hlatshwayo, T., 2010. *Diffusion of silver in 6H-SiC*. PhD thesis. University of Pretoria.

Chapter 6

Results and discussion

The effects of radiation damage in the migration of Eu implanted into polycrystalline and single crystalline 6H-SiC were investigated using Raman spectroscopy, SEM, XPS and RBS. This chapter presents and discusses the findings. The rest of this chapter is organised as follows: section 6.1 presents and discusses the polycrystalline SiC results and section 6.2 presents and discusses the single-crystalline 6H-SiC results.

6.1 Polycrystalline SiC results

6.1.1 Radiation damage

Simulation of Eu implantation into SiC was performed using Stopping and Ion Range in Matter (SRIM 2013) [1]. The detailed full cascade calculation was used in the simulation with the displacement threshold energy of 35 eV for silicon and 20 eV for carbon [2, 3]. The ion fluence was converted into displacement per atom (dpa) using equation 6.1:

$$dpa = \frac{\frac{V_{ac}}{ion(cm)} \times \varphi(ions.cm^{-2})}{\rho_c(ions.cm^{-3})} \qquad (6.1)$$

where φ is the ion fluence, ρ_c is the theoretical atomic density of silicon carbide (9.641×10^{22}atm/cm^3) and $v_{ac}/ion(cm)$ is the vacancy per ion ratio obtained from SRIM 2013

Figure 6.1 shows the simulated together with experimental results of Eu implanted into SiC at RT, 350 and 600 ^{o}C with energy of 270 keV. The projected range (Rp) of the measured Eu depth profiles are in agreement with the simulated one of about 75 nm. However, the measured profiles are broader than simulated profile. Furthermore the 600 ^{o}C implanted profile is even broader than the RT and 350 ^{o}C profiles. The broadness of 350 and 600 ^{o}C implanted profiles is probably due to radiation enhanced diffusion during implantation at these temperatures. The produced damage in displacement per atom (dpa) are closer to the

surface with about 19 dpa at the surface and 43 dpa at 50 nm below the surface. Assuming that 0.2 dpa is enough to amorphize SiC, about 160 nm of the RT implanted SiC will be amorphized [4]. Hence, the implanted Eu is embedded in the amorphous layer in the RT implanted samples. The integrated fluence was calculated from the RBS Eu profiles and found to be 1.064×10^{16}, 1.125×10^{16}, 1.096×10^{16} cm^{-2} for RT, 350 ^{o}C and 600 ^{o}C respectively. These fluences are comparable to targeted fluence of 1×10^{16} cm^{-2}

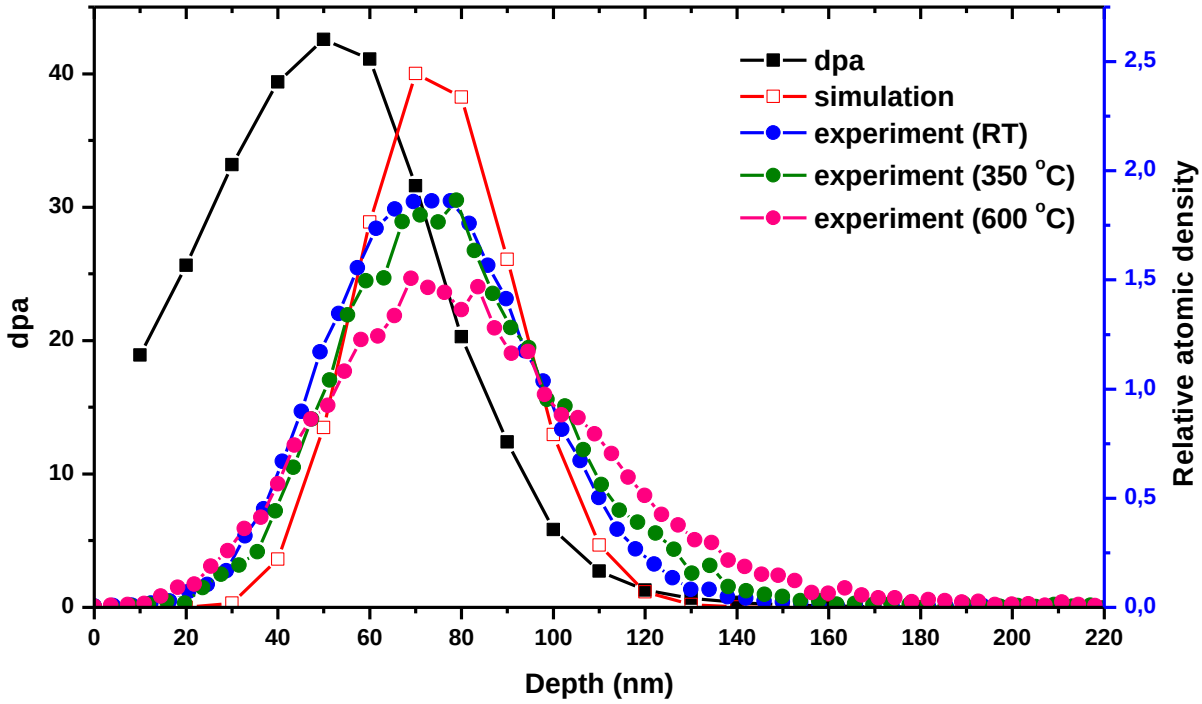

Figure 6.1: *The Eu profiles from RBS of Eu implanted into polycrystalline SiC at RT, 350 ^{o}C and 600 ^{o}C, SRIM 2013 simulated Eu depth profile and displacement per atom (dpa) are also included.*

Figure 6.2 shows the Raman spectra of as-implanted samples compared with un-implanted SiC spectrum. The virgin SiC Raman spectrum has TO and the LO modes at 795 and 965 cm^{-1}respectively and second order SiC bands around 1516 and 1712 cm^{-1}. The appearance of these bands indicates that the SiC substrate consists mainly of the cubic polytype structure [5]. The low intensity shoulder appearing at around 766 cm^{-1} indicates the presence of some 6H-SiC polytype [3]. According to S. Rohmfeld, the peak at 766 cm^{-1} disappears after annealing at temperatures greater than 1600 ^{o}C, indicating that it is related to the crystalline imperfections in 3C-SiC that still exist even after annealing at temperatures up to 1400 ^{o}C [6].

Implantation of Eu ions into SiC at room temperature resulted in reduction in intensities and broadening of SiC characteristic peaks accompanied by the appearance of small Si-Si peak around 530 cm^{-1} and C-C peak around 1430 cm^{-1} indicating the amorphous SiC structure consistent with critical amorphization dpa as predicted by SRIM [7, 8]. The appearance of Si-Si and C-C peaks with low intensity SiC peaks still present in the RT implanted SiC might indicate that the damaged layer was not fully amorphized. Using absorption coefficients of 514.5 nm laser in amorphous SiC, the laser penetration depth (d_p) was calculated using equation 6.2 [9], and was found to be about 43 nm. Comparing this penetration depth with the estimated amorphous layer of about 160 nm, it is quite clear that the damage layer was not fully amorphized.

$$d_p = -\frac{\ln 0.1}{2\alpha} = \frac{2.3}{2\alpha} \tag{6.2}$$

where α is the photoabsorption coefficient [10, 11].

Implantation at 350 and 600 ^oC resulted in a reduction in a relative intensities of the TO and LO Raman modes and slight appearance of the broad Si-Si peak at 530 cm^{-1}, indicating accumulation of defects without amorphization in the implanted samples. The relative intensities of the TO and LO Raman modes of 350 ^oC implanted SiC were significantly lower compared to the 600 ^oC implanted SiC indicating less defects retained in the latter samples. This is especially true since the critical implantation temperature to amorphize SiC is about 300 ^oC [12], hence the amount of damage decreases with increasing implantation temperature. This indicates the radiation hardness of SiC at elevated irradiation temperatures [12].

Annealing the room temperature implanted samples at 1000 ^oC (Figure 6.3 (a)) resulted in an almost disappearance of the Si-Si and C-C peaks and re-emergence of SiC characteristic Raman peaks indicating annealing/healing of defects. This increase in relative intensity of the TO and LO modes progressed with an increase in the annealing temperature up to 1400 ^oC. However, the TO and LO intensities of annealed samples is still less than the virgin SiC indicating some defects still remaining. This means that the defects in SiC needs higher temperatures (greater than 1400 ^oC) to anneal out. Similar results were obtained after annealing the 350 and 600 ^oC implanted SiC–Figure 6.3(b) and (c).

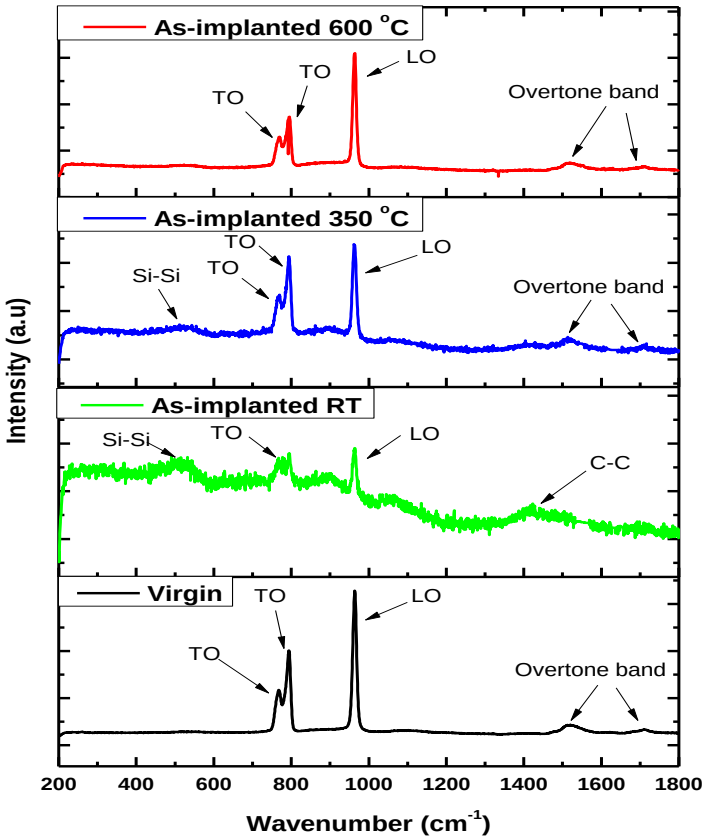

Figure 6.2: *Raman spectra of un-implanted polycrystalline SiC and the SiC implanted with Eu ions at RT, 350 °C and 600 °C.*

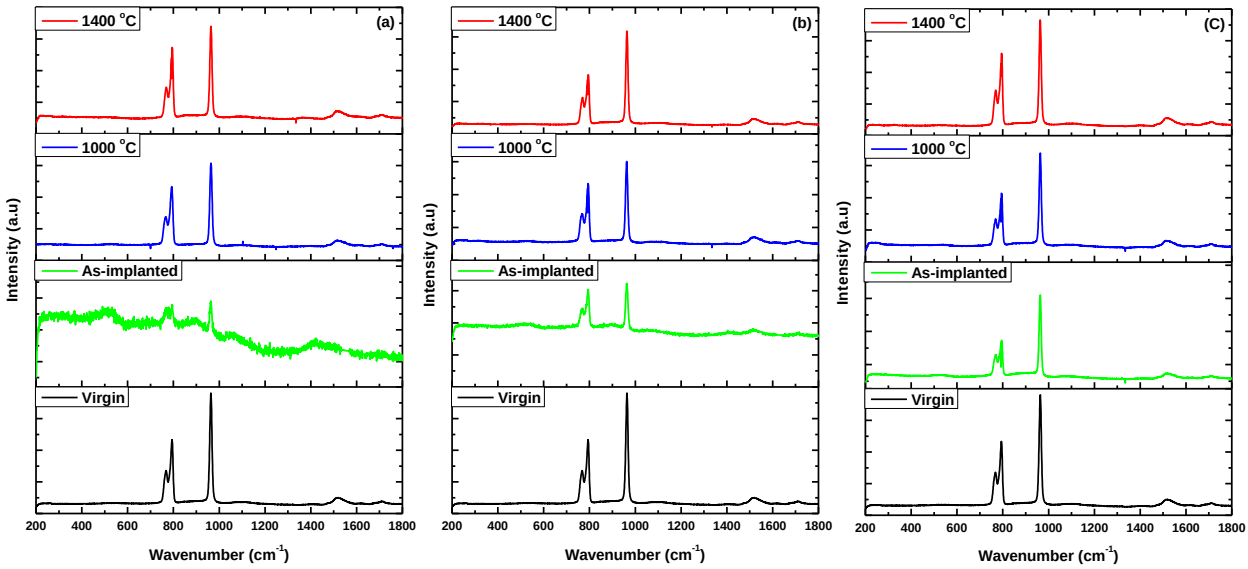

Figure 6.3: *Raman spectra of un-implanted, as-implanted and samples annealed at 1000 °C and 1400 °C (a) RT implantation, (b) 350 °C implantation and (c) 600 °C implantation.*

6.1.2 Surface morphological results

Figure 6.4 shows the SEM micrographs of the SiC samples implanted with Eu ions at RT, 350 ^{o}C and 600 ^{o}C. The virgin/un-implanted SEM micrograph is included for comparison. The surface of the as-received/virgin SiC has polishing marks from the manufacturing process. Implantation at room temperature resulted in the disappearance of the polishing marks on the SiC surface confirming amorphization of SiC in agreement with SRIM and Raman spectroscopy results. The disappearance of the polishing marks is caused by swelling of the surface layer of SiC due to the amorphization of SiC after implantation at RT, similar results were reported in the literature [13, 14]. Samples implanted at elevated temperatures retained the polishing marks, which can be attributed to the lack of amorphization in agreement with Raman results. Moreover, the sample implantation at 350 ^{o}C also resulted in the appearance of grain boundaries. The average grain size of about 3.8 µm was estimated using imageJ software. The appearance of grain boundaries in the 350 ^{o}C implanted samples might be due to higher defects initially present in the samples. Raman results indicated more defects in the 350 ^{o}C implanted sample compared to 600 ^{o}C implanted SiC.

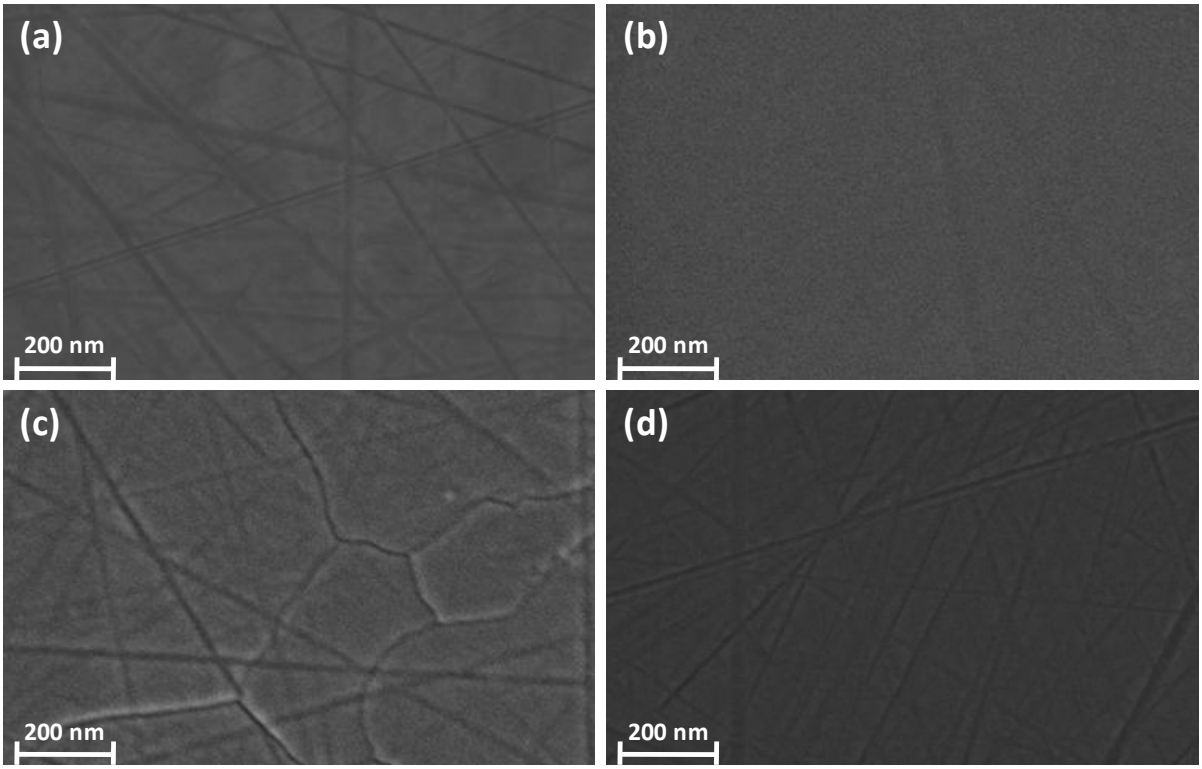

Figure 6.4: *SEM micrographs the (a) virgin/un-implanted polyscrystalline SiC compared to SiC implanted with 270 keV Eu+ ions at (b) RT, (c) 350 ^{o}C and (d) 600 ^{o}C.*

Figure 6.5 shows the SEM micrographs of SiC implanted at RT, SiC implanted at RT then sequentially annealed at 1000, 1100, 1200, 1300 and 1400 ^{o}C. Annealing at 1000 ^{o}C resulted in the formation of tiny crystallites, indicating some recrystallization of the initially amorphous microstructure of SiC taking place which was also confirmed by the disappearance of C-C and Si-Si modes in the Raman spectrum, Figure 6.3(a). Similar recrystallization results were reported in the literature [15, 16]. Some of these tiny crystallites increased in size resulting in appearance of pores after annealing at 1100 ^{o}C. Increasing annealing temperature further resulted in the combination of crystallites forming bigger particles. The average crystallite size increased to about 156 and 270 nm after annealing at 1200 and 1300 ^{o}C. Some bigger pores were observed after annealing at 1200 ^{o}C. The changes on the surface indicated the re-crystallization of the amorphous SiC layer. Annealing at 1400 ^{o}C resulted in average faceted crystallites of about 270 nm on the surface with fine crystallites still present.

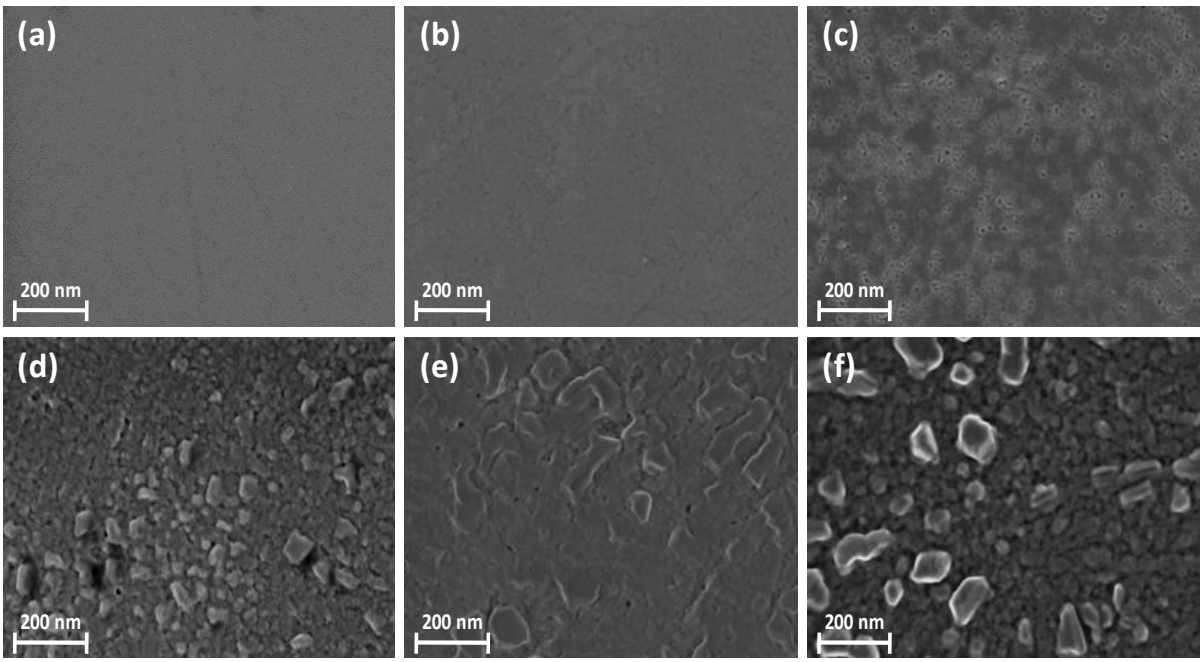

Figure 6.5: *SEM micrographs of SiC implanted with 270 keV Eu ions at RT before and after sequentially annealing: (a)the as-implanted sample, (b) annealed at 1000 ^{o}C, (c)annealed at 1100 ^{o}C, (d)annealed at 1200 ^{o}C, (e) annealed at 1300 ^{o}C and (f) annealed at 1400 ^{o}C.*

Figure 6.6 shows the SEM micrographs of SiC implanted with Eu at 350 ^{o}C and SiC implanted at 350 ^{o}C then sequentially annealed at 1000, 1100, 1200 1300 and 1400 ^{o}C.

Annealing at 1000 ^{o}C resulted in reduction of polishing marks on the surface due to sputtering on the surface layer, while annealing at 1100 ^{o}C caused the appearance of some pores along the grain boundaries. These pores became more pronounced in the sample annealed at 1200 ^{o}C. These pores were still visible and larger after annealing at 1300 ^{o}C. The pores connected and opened up along the grain boundaries after annealing at 1400 ^{o}C resulting in the widening up of the grain boundaries. The average width of grain boundary opening was about 14 nm in the as-implanted and about 130 nm in the samples annealed at 1400 ^{o}C. This could be an indication of some thermal etching which is more preferred on grain boundaries. The average grain size as estimated with ImageJ increased from 3.8 μm in the as-implanted samples to 5.5 μm in the 1400 ^{o}C annealed samples.

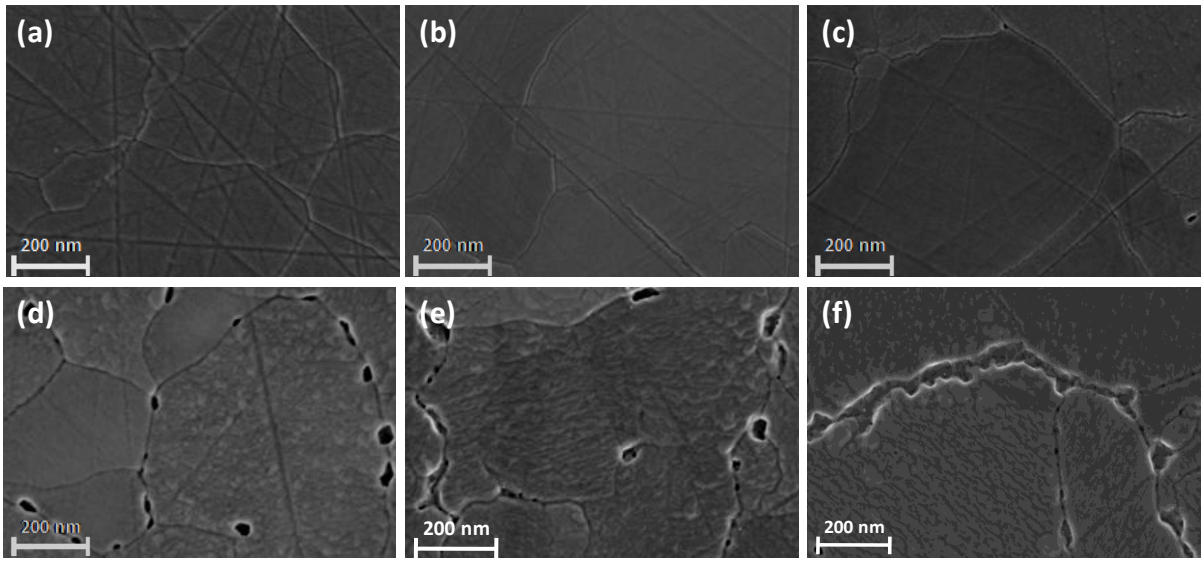

Figure 6.6: *SEM micrographs of SiC implanted with 270 keV Eu ions at 350 ^{o}C before and after isochronal annealing: (a) as-implanted sample, (b) 1000 ^{o}C annealed sample, (c) 1100 ^{o}C annealed sample, (d) 1200 ^{o}C annealed sample and (e) 1300 ^{o}C annealed sample and (f) 1400 ^{o}C.*

Figure 6.7 shows the SEM micrographs of SiC implanted with Eu at 600 ˚C and SiC implanted at 600 ^{o}C then sequentially annealed at 1000, 1100, 1200 1300 and 1400 ^{o}C. No major changes were observed after annealing at 1000 ^{o}C, however the polishing marks on the surface became more visible. Annealing at 1100 ^{o}C resulted in the appearance of big and small crystallites on the surface accompanied by clear appearance of grain boundaries. At 1200 ^{o}C the crystallites reduced in size with grain boundaries still visible. Annealing at 1300

^{o}C resulted in thermal etching on grain boundaries. The rather fine crystallites reappeared after annealing at 1400 ^{o}C with the grain boundaries still visible. The average grain sizes changed to about 3.5, 3.5, 2.7 and 2.7 μm after annealing at 1100, 1200, 1300 and 1400 ^{o}C respectively. The opening width of grain boundaries increased with increasing temperature of annealing

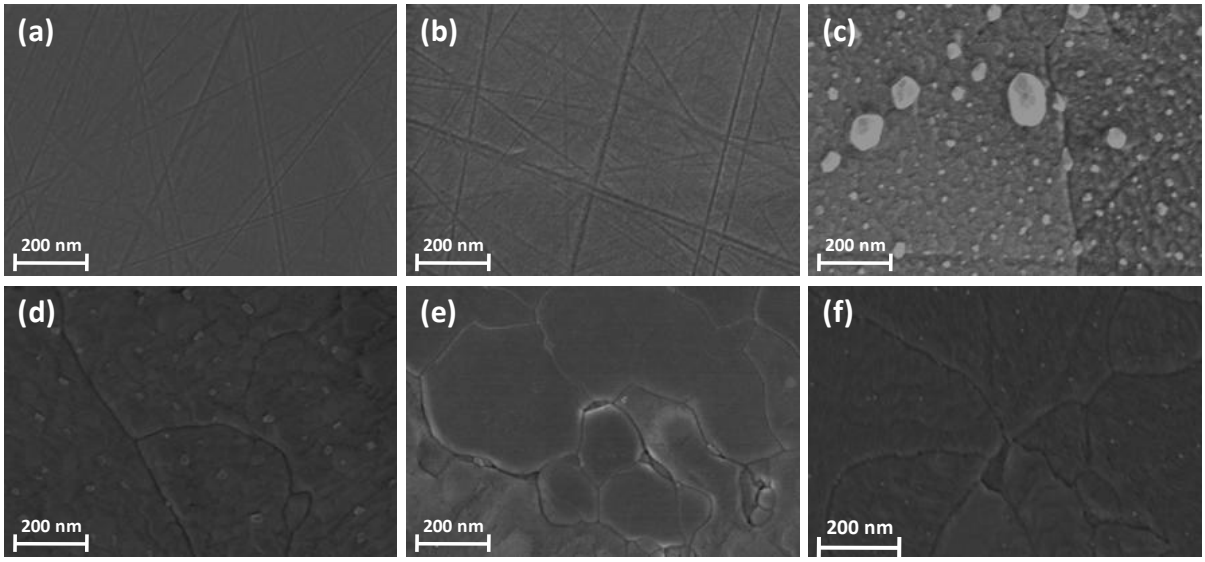

Figure 6.7: *SEM micrographs of SiC implanted with 270 keV Eu ions at 600 ˚C before and after isochronal annealing: (a) as-implanted sample, implanted then sequential annealed up to (b) 1000 ^{o}C, (c) 1100 ^{o}C, (d) 1200 ^{o}C and (e) 1300 ^{o}C and (f) 1400 ^{o}C.*

6.1.3 Migration results

The RBS depth profiles of Eu implanted into SiC at RT, 350 and 600 ^{o}C after sequentially annealed at temperatures from 1000 to 1400 ^{o}C in steps of 100 ^{o}C are shown in Figure 6.8. The as-implanted Eu profiles are included for comparison. The Eu retained ratios, squares of full width at half maximum (FWHM) and peak position as a function of annealing temperature are shown in Figure 6.9. The FWHM is an important parameter because the broadening of an implanted profile is an indication that diffusion has taken place [17].

Annealing the room temperature implanted sample at 1000 ^{o}C caused migration of Eu towards the surface resulting in the formation of an extra small (segregated) peak on the surface. No loss was observed at this temperature; however, the prominent Eu peak was broader (see Figure 6.9(b)) and skewed towards the surface indicating diffusion of Eu atoms

towards the surface. There can be two reasons for this segregation towards the surface. The segregation might be driven by the usual driving force for surface segregation, i.e. minimisation of the Gibbs free energy. The epitaxial re-growth of the bombardment-induced amorphous region from the crystalline bulk might also aid this process. The latter process is largely negated by the fact that implantation of SiC at temperatures higher than 350 ^{o}C does not amorphize SiC [18] and the samples implanted at 350 ^{o}C also exhibited this segregation – see Figure 6.8(b) Considering the Eu melting point of about 822 ^{o}C, Eu should have melted and evaporated at 1000 ^{o}C. Therefore, the Eu surface peak might be indicating an Eu oxide compound with higher melting point. This migration of Eu and segregation towards the surface resulted in a small shift of the peak position towards the surface. Annealing the RT implanted sample at 1100 ^{o}C resulted in the disappearance of the Eu surface peak and a loss of about 25% of the implanted Eu. Figure 6.9(b) shows that no further broadening of Eu peak occurred. However, the profile became even more skewed towards the surface. The disappearance of the smaller Eu surface peak accompanied by loss of implanted Eu might be due to sublimation of Eu (or Eu compound) at this temperature (1100 ^{o}C). Asymmetric broadening accompanied by Eu loss was observed after annealing at 1200 ^{o}C and at 1300 ^{o}C. No peak shift was observed after annealing at these temperatures, see Figure 6.9(c). Also a more of tailing towards the bulk was observed after annealing at 1300 ^{o}C and 1400 ^{o}C. A total of about 60% of Eu was lost after annealing at 1400 ^{o}C which resulted in a further shift of the peak position towards the surface although there was no real difference in the surface sections of the 1300 and 1400 ^{o}C profiles beyond the (maximum) peak. Therefore, it is not possible to state with certainty whether there was further diffusion during annealing at 1400 ^{o}C. The Eu surface peak is found in both the RT and 350 ^{o}C implanted samples after annealing at 1000 ^{o}C, this indicates that Eu must have segregated to the surface and oxidized there on interaction with oxygen. This segregation is due to the damage in the surface layer of SiC and its dependent on the amount of radiation damage retained in the surface layer. Hence, more pronounced Eu surface peak in the RT implanted sample than in the 350 ^{o}C implanted sample.

Annealing the 350 ^{o}C implanted samples at 1000 ^{o}C resulted in a shift of the implanted Eu profile towards the surface and the formation of a smaller peak on the surface. However, the peak formed on the surface is much smaller than the one formed after annealing the room temperature implanted sample at 1000 ^{o}C – see Figure 6.8. There was no loss of implanted Eu

or broadening of the Eu profile after annealing at this temperature – Figure 6.9. Similar to the room temperature implanted samples, annealing at 1100 ^{o}C resulted in the disappearance of the smaller surface peak accompanied by some loss of implanted Eu. This loss of implanted Eu increased with annealing temperature. Unlike the room temperature samples, no significant broadening was observed after sequentially annealing at temperatures > 1000 ^{o}C, which proves that Eu migrated through grain boundaries shown in SEM images – see Figure 6.6.

Annealing the 600 ^{o}C implanted samples at 1000 ^{o}C caused no significant change in the implanted Eu profiles. Annealing at 1100 ^{o}C resulted in slight peak broadening accompanied by peak shift towards the surface with no Eu being lost. However, this broadening was again within the error limit of the RBS system and no reliable diffusion coefficient could be extracted. This was also the case for the samples annealed at the higher temperatures. In all these annealing temperatures, no significant loss was observed, indicating that Eu atoms were probably trapped within the SiC grains during the self–annealing of the polycrystalline SiC due to implantation at 600 ^{o}C. There are several examples (cf. the review by Malherbe [18]) where there is no volume diffusion in SiC but only grain boundary diffusion for a specific element. A well-known example is that of Ag in SiC with no (volume) diffusion in 6H-SiC [19], but there is a grain boundary diffusion in room temperature Ag implanted poly-crystalline 3C-SiC [20].

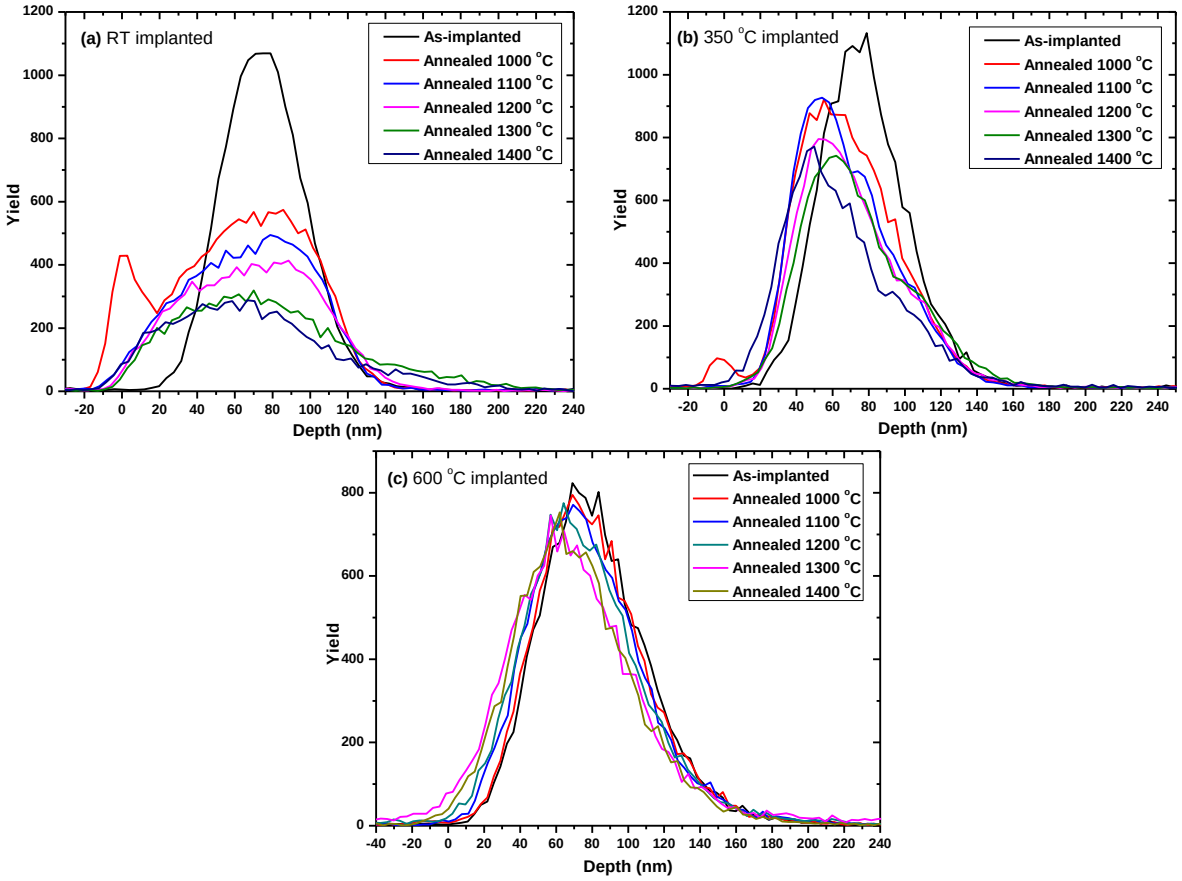

Figure 6.8: *Depth profiles of Eu implanted into SiC at (a) RT, (b) 350 and (c) 600 °C at 270 keV, and after isochronal annealing from 1000 to 1400 °C insteps of 100 °C for 5 hrs.*

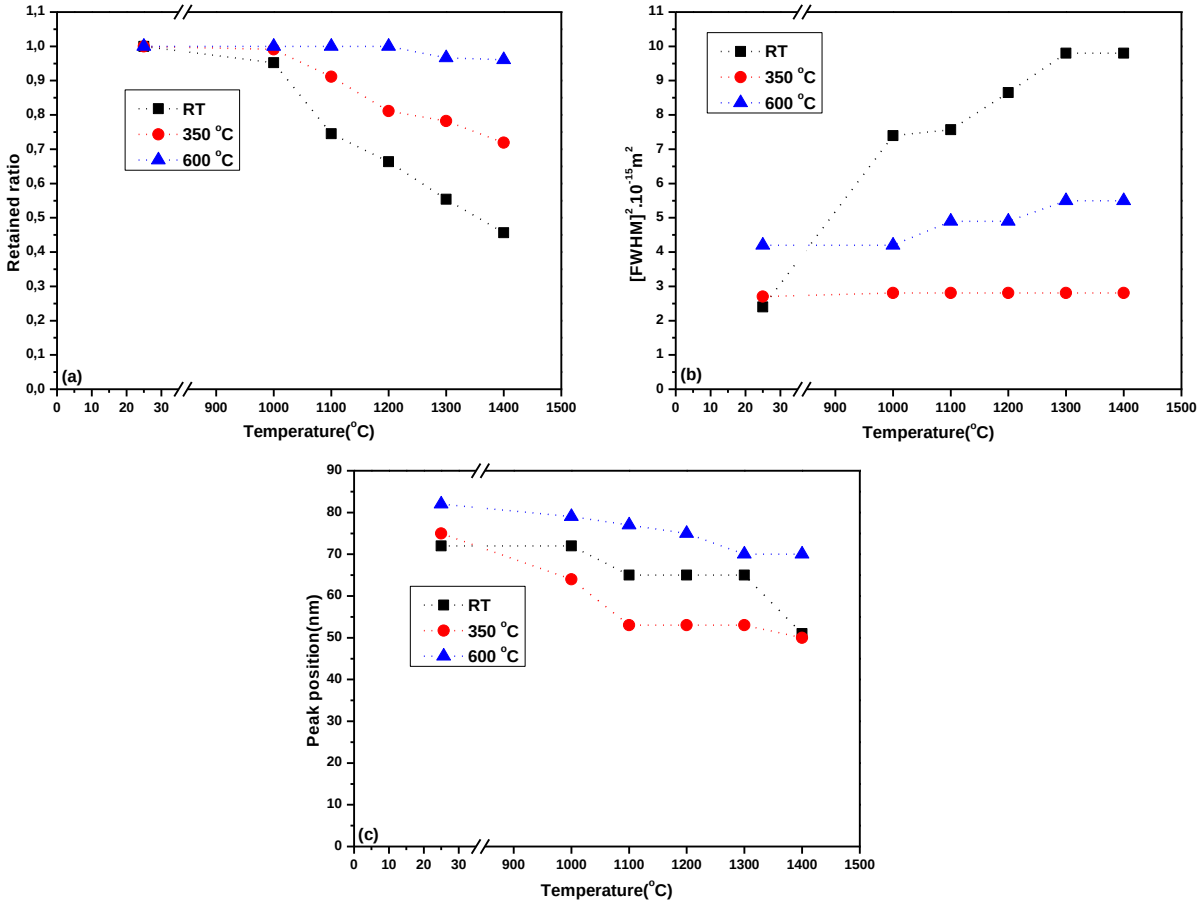

Figure 6.9: *Graphs of (a)retained ratio of Eu implanted into SiC at RT, 350 and 600 °C after isochronal annealing at 1000 to 1400 °C for 5hrs in steps of 100 °C, (b) full width at half maximum as a function of annealing temperature of Eu implanted into SiC at RT, 350 and 600 °C after isochronal annealing at 1000 to 1400 °C for 5hrs in steps of 100 °C and (c)peak position as a function of annealing temperature of Eu implanted into SiC at RT, 350 and 600 °C after isochronal annealing at 1000 to 1400 °C for 5hrs in steps of 100 °C.*

In order to gain more insight into the composition and chemical states of SiC implanted at RT and annealed at 1000 °C, XPS was performed on the samples annealed at 1000 °C. Figure. 6.10 shows a XPS survey scan of SiC implanted with Eu and annealed at 1000 °C. The XPS analysis was performed only on the 1000 °C annealed RT implanted sample to be able to examine the chemical state of the Eu surface peak that is evidently present on the surface of the sample. It is clear that the elements that are present on the surface of SiC are mainly silicon, carbon, oxygen and europium. The oxygen KLL signal appears at the binding energy 976.2 eV, which was interpreted by Demri et al. [21].

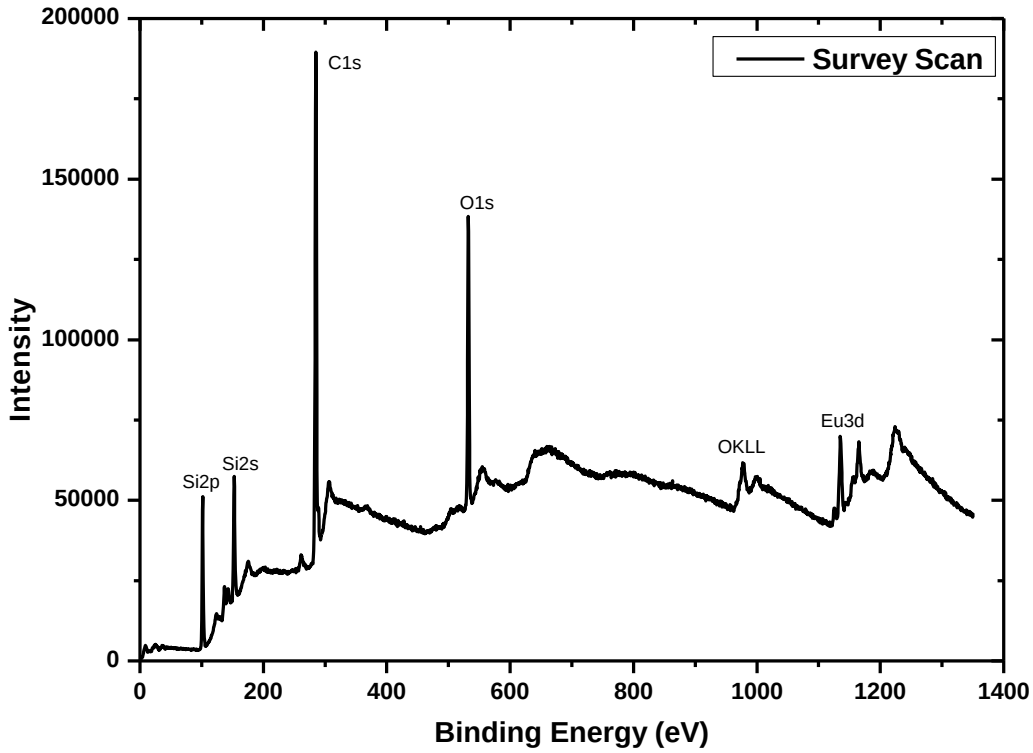

Figure 6.10: *XPS survey spectra of SiC implanted with Eu and annealed at 1000 ^{o}C.*

Figure 6.11 shows high resolution XPS spectra of (a) Si2p peak, (b) C1s peaks, (c) O1s peak and (d) Eu3d peaks for SiC implanted with Eu and annealed at 1000 ^{o}C. A Si2p spectrum has a peak at binding energy ≈ 101 eV attributed to SiC [22, 23, 24, 25, 26]. The Si2p peak is the only signal of Si2p in the current study. In other studies, the SiO_2 component of Si2p at the higher binding energy of 103 eV was observed [22, 27, 28, 26].

The C1s spectrum has a peak at binding energy of 283 eV which is due to crystalline SiC [22, 23, 24, 25, 26, 29] and a peak at binding energy of 285 eV is attributed to hydrocarbon or a contaminant carbon layer [24, 25, 28, 26]. It was also reported that the binding energy of C1s component obtained in the range 284.4 - 285.2 eV was associated with hydrocarbon [30]. A less intense C1s signal in the higher binding energy of 289.5 eV is also seen in Figure 6.11 (b) confirming the hydrocarbon which may be coming from the 6H-SiC impurities in the polycrystalline SiC as mentioned in [3].

The O1s signal is observed at the binding energy 532.22 eV. This signal is mostly observed in oxidized SiC materials [22, 29].

The $Eu3d_{5/2}$ spectrum consist of peaks at binding energies 1126.4, 1136.18, 1156 and 1165.8 eV. The peak at 1126.4 eV may be attributed to Eu(II) species (oxalates) while the peak at 1136.18 eV may be attributed to a shake-down satellite of Eu(II) as reported in literature by Uwamino at al [31]. The other two peaks at the higher binding energy location 1156 and 1165.8 eV are also attributed to Eu(II) [31]. Hence, the Eu surface peak that appears on the depth profile after annealing at 1000 ^{o}C is the Eu complex compound, most probably a Eu oxalate.

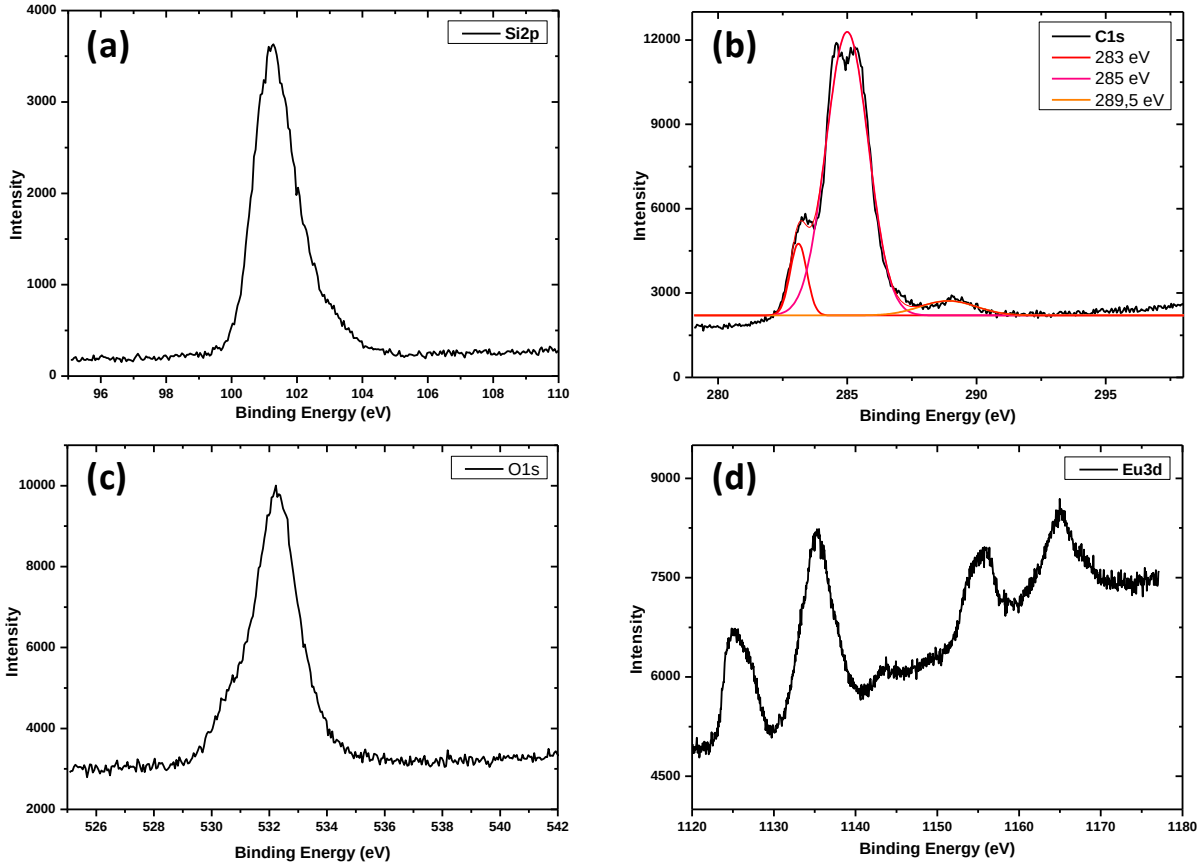

Figure 6.11: High resolution *XPS spectra of SiC implanted with Eu and then annealed at 1000 ^{o}C for (a) Si2p peak, (b) C1s peaks and fitted peaks, (c) O1s peak and (d) Eu3d peaks.*

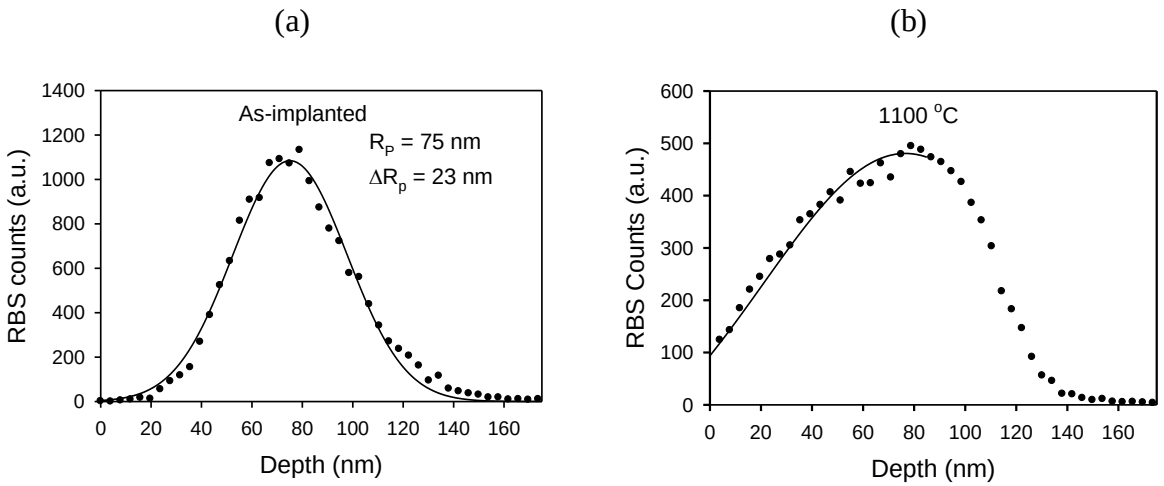

Figure 6.12: *Eu RBS depth profiles of the RT implanted samples (a) as-implanted sample and of (b) the sample vacuum-annealed at 1100 °C. The solid lines are least-square fits of a Gaussian function to the as-implanted data in (a) and of the Fick solution to only the surface half of the 1100 °C annealed profile in (b).*

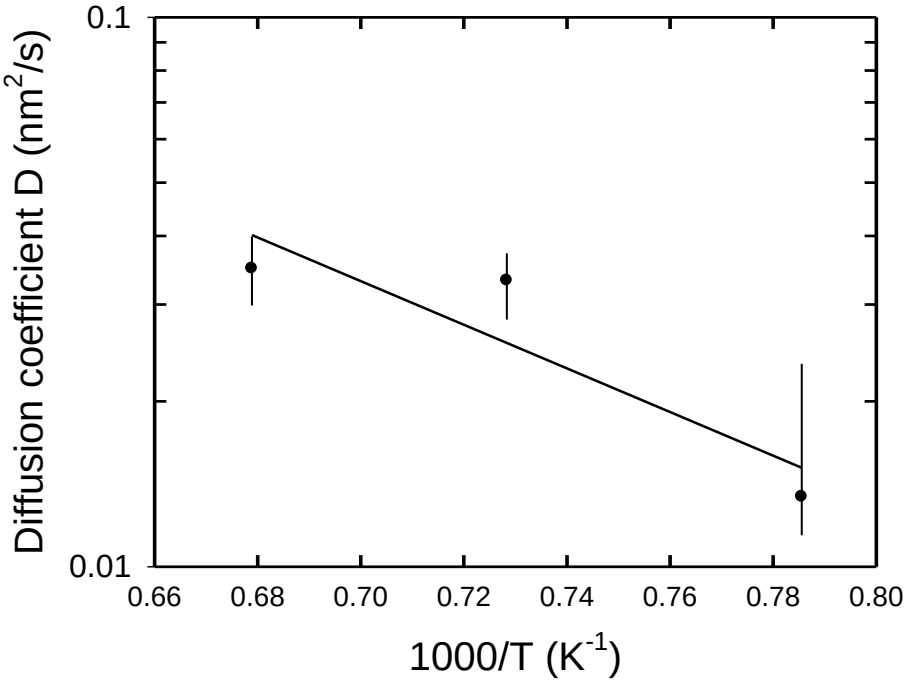

Figure 6.13: *Arrhenius plot of the diffusion coefficients of polycrystalline 3C-SiC implanted at room temperature with 270 keV europium ions and sequentially vacuum annealed for 5 h at 1000 °C, 1100 °C and 1200 °C.*

The RBS depth profiles of the RT implanted sample were least square fitted to the general solution of the Fick's differential diffusion equation for an initial Gaussian profile [17]. This was possible because the as-implanted profile fitted well to a Gaussian function – see Figure 6.12(a). As was discussed earlier in this section, the depth profiles of the annealed samples asymmetrically broadened towards the surface, i.e. the side where most of the damage due to the Eu ion implantation was retained– see Figure 6.1. Consequently, only the surface side of these depth profiles were fitted. The fitted depth profiles for RT implanted and the sample annealed at 1100 ^{o}C are shown in Figure 6.12(a) and (b) respectively. From such a fit the diffusion coefficient D, as discussed in chapter 2, can be determined. Because of the surface Eu peak, only a limited number of data points of the 1000 ^{o}C annealed sample could be fitted. Only a Gaussian function could be reliably fitted to this (limited) profile and the diffusion coefficient was determined from the broadening of the Gaussian function compared to the Gaussian fit of the as-implanted sample. Although the samples annealed at 1300 ^{o}C and 1400 ^{o}C exhibited some broadening, this broadening was within the error limit of the utilized RBS measurements. Consequently, no reliable diffusion coefficients could be determined for these two temperatures. The diffusion coefficients of 0.015, 0.033 and 0.035 nm^2/s were obtained for sequential 5 hours annealing of an as-implanted sample annealed at 1000 ^{o}C, 1100 ^{o}C and 1200 ^{o}C, respectively. From an Arrhenius plot, shown in Figure 6.13, a diffusion activation energy of 0.8 eV and 20 nm^2/s for D_o were obtained, where D_o is a pre-exponential factor as discussed in section 2.2. The error bars in Figure 6.13 were determined from fitting profiles with small differences within the RBS error limit.

6.1.4 Discussion

Implantation of Eu into SiC at room temperature resulted in amorphization of SiC layer while implantation at 350 and 600 ^{o}C retained defects, with more defects retained by the 350 ^{o}C implanted sample compared to the 600 ^{o}C implanted sample. The formation of defects without amorphization in the 350 and 600 ^{o}C implanted samples was expected as the implantation temperatures were higher than critical amorphization of SiC of about 300 ^{o}C.

Annealing the RT and 350 ^{o}C implanted samples at 1000 ^{o}C caused migration of Eu towards the surface accompanied by the appearance of the surface peak. This surface peak was more prominent in the annealed RT implanted sample which initially had more radiation defects. Hence, the migration of Eu towards the surface resulting in the formation of surface peak is radiation damage enhanced. This is especially true because the surface peak did not appear in the high temperature implanted sample(600 ^{o}C, which retained less damage) annealed at 1000 ^{o}C. The surface peak was found by using XPS, to be a europium oxalate compound which formed on the surface. The most loss of Eu took place after the disappearance of the Eu surface peak, i.e. after annealing the room temperature and 350 ^{o}C implanted samples at 1100 ^{o}C. Annealing at temperatures > 1100 ^{o}C resulted in the Eu loss through the surface in the 350 ^{o}C implanted sample as a result of pores that opened up on the surface. Annealing of the 600 ^{o}C implanted sample retained most of Eu throughout the annealing steps with small particles appearing on the surface after annealing at temperatures of up to 1200 ^{o}C and disappearing at annealing temperatures greater than 1200 ^{o}C. The retention of Eu in the 600 ^{o}C implanted sample can be associated with the ability of less damaged SiC to trap the implanted Eu. It was observed from Raman and SEM results that the migration/diffusion taking place in the room temperature implanted sample is mostly assisted by radiation damage. Consequently, it appears from the retained ratios in Figure 6.9 that the radiation damage enhanced diffusion/migration of Eu taking place in the room temperature implanted sample is more faster than the diffusion/migration of Eu taking place in the 350 ^{o}C sample.

Small activation energies for diffusion in the RT implanted samples are usually ascribed to grain boundary diffusion or another fast diffusion mechanism such as interstitial diffusion. The activation energy of about 0.8 eV in this study is similar to that predicted for Si interstitial diffusion in SiC [32]. The implantation depth of the Eu atoms is of the order of 100 nm while the average grain sizes of samples in this study are of the order of several microns. The small activation energy thus indicates that it is reasonable to assume that Eu diffused to the surface of the samples through interstitials. This would also explain why the Eu profiles were skewed towards the surface.

The lack of diffusion of Eu in the 350 ^{o}C implanted sample can be linked to the migration of Eu through the surface during the annealing process. The pores (SEM results) on the surface acted as preferred path for Eu to escape, this is also indicated by the peak position shifting more towards the surface in the depth profiles.

6.2 Single-crystalline 6H-SiC results

6.2.1 Radiation damage

Figure 6.14 shows the simulated results together with the experimental results of the 270 keV Eu ions implanted into 6H-SiC at RT and 350 ^{o}C. The difference in concentration in the measured profiles might be due to slight differences in the Eu ion fluences. The calculated fluences were 1.252 × 10^{16} and 1.140 × 10^{16} cm^{-2} for RT and 350 ^{o}C implanted samples respectively.

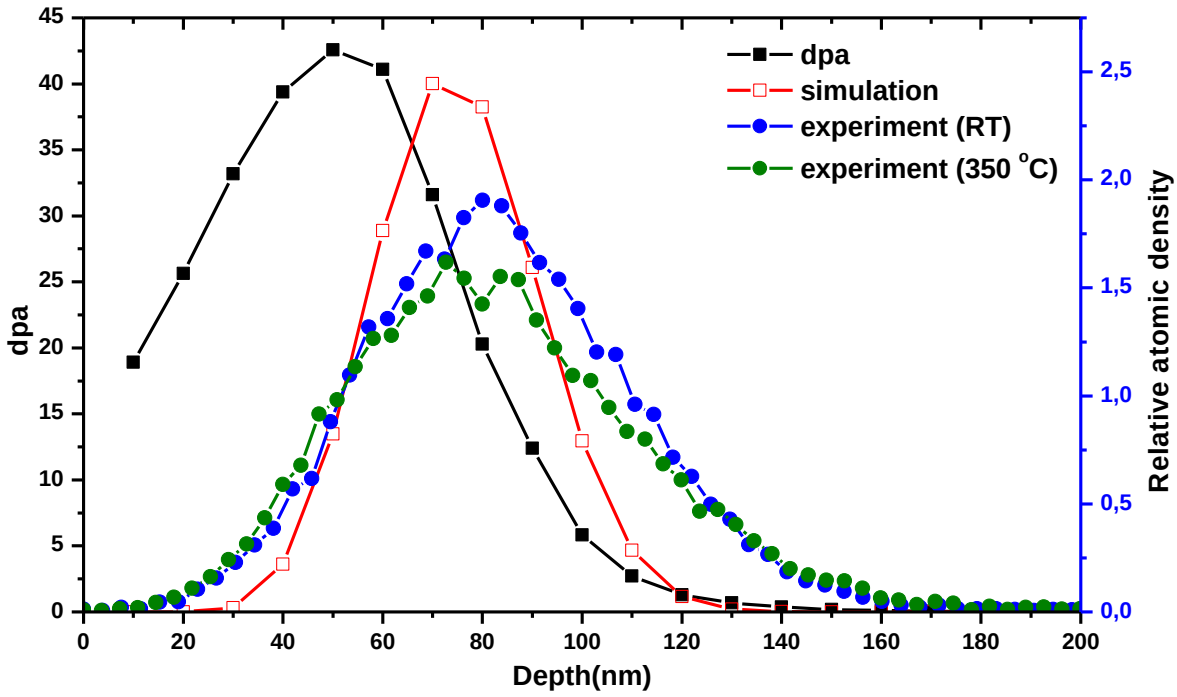

Figure 6.14: *The Eu depth profiles (from RBS) of Eu implanted into 6H-SiC at RT and 350 ^{o}C together with SRIM simulated Eu depth profile and displacement per atom (dpa).*

Figure 6.15 shows the Raman spectra of the un-implanted/virgin and implanted 6H-SiC samples. The Raman spectrum of virgin 6H-SiC has all the characteristic peaks of pristine

6H-SiC [33]: the 6H longitudinal acoustical (LA) mode at 505 cm^{-1}, the two-transverse optical (TO) modes at 766 and 789 $cm^{-1}$and the longitudinal optical (LO) mode at 965 cm^{-1}. The second order SiC peaks are also visible at 1513 and 1712 cm^{-1}. Both implantations resulted in reduction in intensities of SiC characteristic peaks. This reduction in intensities was more pronounced and accompanied by appearance of Si-Si and C-C peaks at 523 and 1430 cm^{-1} in the sample implanted at RT indicating amorphization of SiC implanted layer. The appearance of Si-Si and C-C peaks with broader SiC peaks still present in the RT implanted 6H-SiC might be indicating the penetration depth of the laser was deeper than the amorphized layer (of about 160 nm as predicted from SRIM simulation) or the damaged layer that is not fully amorphized. Using absorption coefficients of 514.5 nm laser in amorphous SiC [9], the penetration depth was estimated to be about 48 nm, as discussed in section 6.1. Hence, the broad SiC indicate that there is some crystalline SiC in the amorphous layer. Implantation at 350 ^{o}C resulted in a decrease in the peak intensities accompanied by broadening indicating defects were retained with no amorphization.

Annealing the RT implanted samples at 1000 ^{o}C resulted in the increase in the intensity of the 6H-SiC Raman characteristic peaks accompanied by the disappearance of the Si-Si and C-C peaks indicating recrystallization (-Figure 6.16(a)). This increase in intensity progressed with annealing temperature up to 1400 ^{o}C. However, the intensity of characteristic peaks of the RT implanted samples annealed up to 1400 ^{o}C was still lower than intensity of characteristic peaks of the virgin samples, indicating some defects remaining. Annealing of the 350 ^{o}C implanted samples recovered the initially damaged structure that had less defects-Figure 2.16(b).

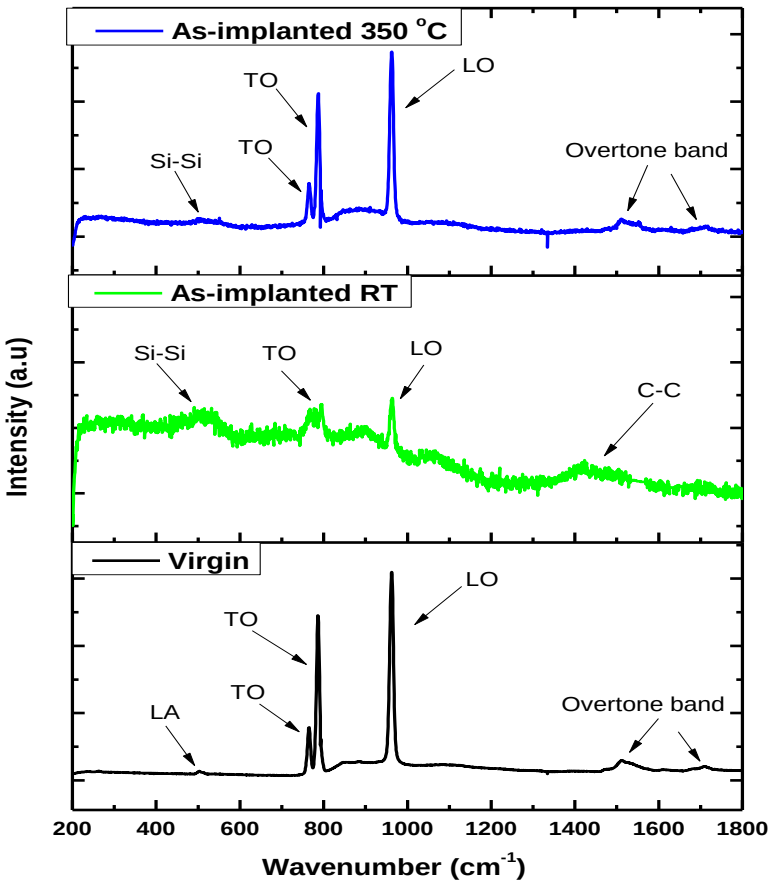

Figure 6.15: *Raman spectra of un-implanted single-crystalline 6H-SiC and 6H-SiC implanted with Eu ions at RT and 350 °C.*

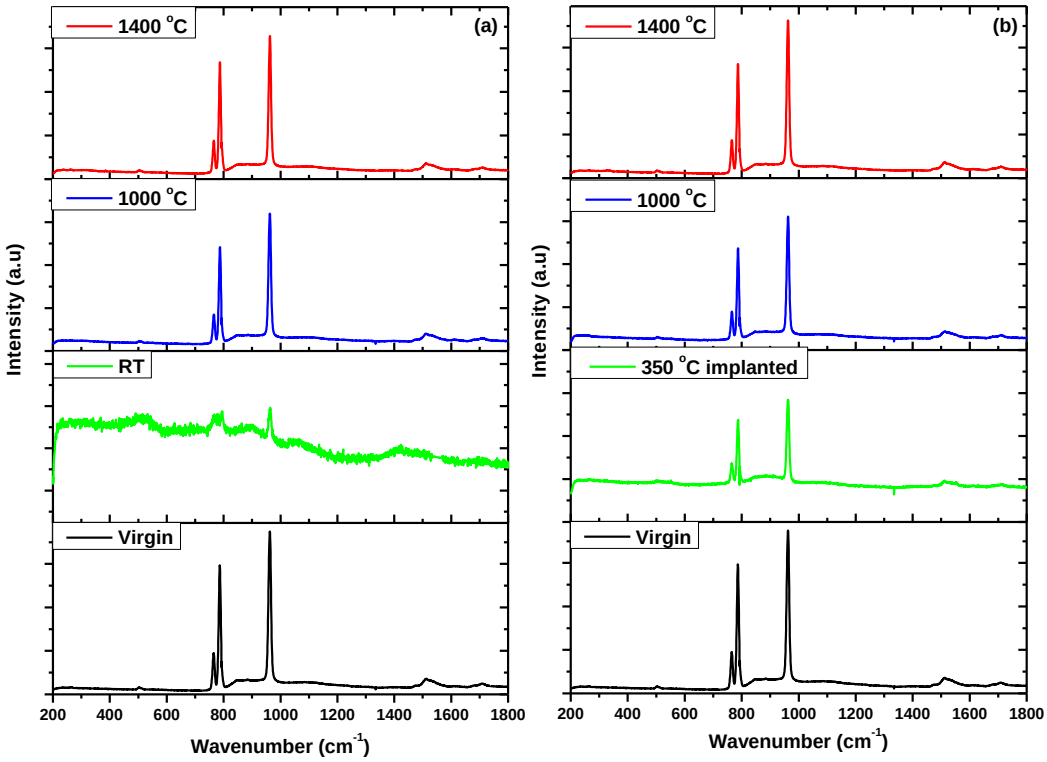

Figure 6.16: *Raman spectra of un-implanted, (a) as-implanted and RT implanted then annealed at 1000°C and 1400 °C (b) 350 °C implanted then annealed at 1000 °C and 1400 °C.*

6.2.2 Surface morphological results

Figure 6.17 shows the SEM micrographs of samples implanted at room temperature and 350 °C. The micrograph of virgin/un-implanted 6H-SiC is included for comparison. The un-implanted sample has a smooth surface. Implantation at room temperature resulted in no changes on the surface. However, implantation at 350 °C resulted in a clear appearance of polishing marks on the surface, suggesting the sputtering of weakly bound material on the surface at this temperature [34]. The polishing marks were not observed in the RT implanted samples due to some swelling in the amorphized 6H-SiC [14].

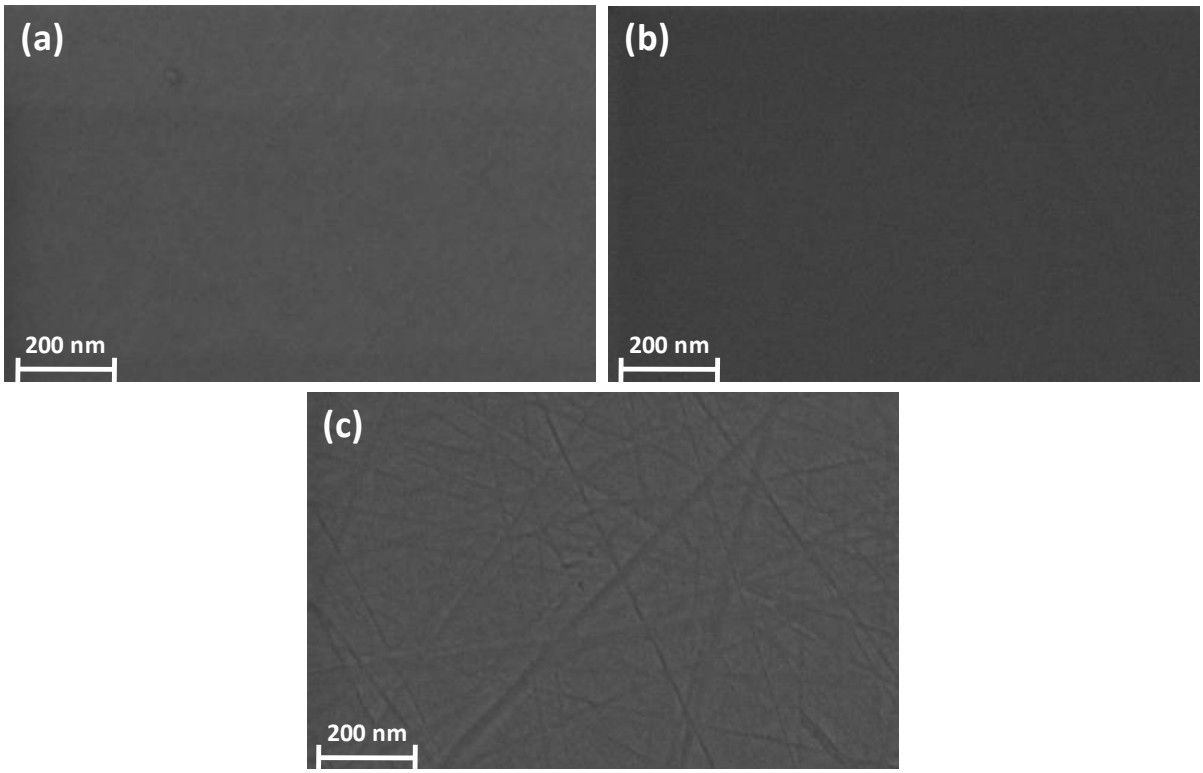

Figure 6.17: *SEM micrographs of the (a) virgin/un-implanted 6H-SiC compared with the samples implanted with 270 keV Eu ions at (b) RT and (c) 350 ^{o}C.*

Figure 6.18 shows SEM micrographs of 6H-SiC implanted at room temperature, implanted at room temperature then sequentially annealed at 1000, 1100, 1200, 1300 and 1400 ^{o}C. Annealing the RT implanted sample at 1000 ^{o}C resulted in the appearance of tiny crystallites on the surface indicating some recrystallization of the damaged 6H-SiC, in line with Raman spectroscopy results discussed earlier. Annealing at 1100 ^{o}C caused some of these tiny crystallites to grow in size. Further annealing at elevated temperatures caused further increase in size of the crystallites with some protruding from the surface. These crystallites became faceted after annealing at 1300 ^{o}C. Some pores between the crystallites can be seen indicating thermal etching occurred after annealing at 1400 ^{o}C. The average crystallite sizes of 29, 200, 373 and 409 nm were estimated by imageJ in the samples annealed at 1100, 1200, 1300 and 1400 ^{o}C respectively.

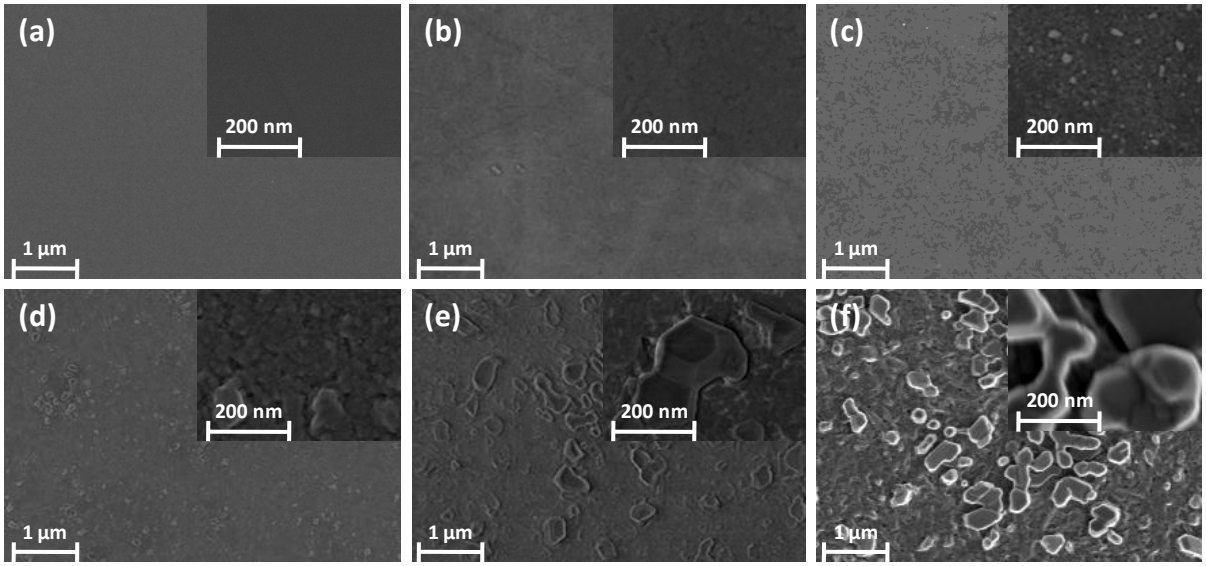

Figure 6.18: *SEM micrographs of 6H-SiC implanted with 270 keV Eu ions at RT before and after isochronal annealing, (a) the as-implanted sample, (b) annealed at 1000 ^{o}C, (c) annealed at 1100 ^{o}C, (d) annealed at 1200 ^{o}C, (e) annealed at 1300 ^{o}C and (f) annealed at 1400 ^{o}C.*

Figure 6.19 shows the SEM micrographs of 6H-SiC implanted at 350 ^{o}C and implanted at 350 ^{o}C then sequentially annealed at 1000, 1100, 1200, 1300 and 1400 ^{o}C. As mentioned before, implantation at 350 ^{o}C resulted in the appearance of polishing marks on the surface of 6H-SiC substrates. No major changes were observed on the surface after annealing the as-implanted sample at 1000 ^{o}C. However the Raman spectroscopy results indicated that the recovery of defects had taken place at this temperature. The polishing marks began to disappear after annealing at 1100 ^{o}C. Annealing at 1200 ^{o}C resulted in complete disappearance of the polishing marks, resulting in a fairly smooth surface with some crystallites appearing on the surface. Some up-lifted crystals appeared on the surface after annealing at 1300 ^{o}C and were clearly visible after annealing at 1400 ^{o}C. The appearance of the up-lifted crystals was due to thermal etching in the 6H-SiC. This thermal etching made the sample surface uneven. Similar uneven thermal etching has been reported in the 6H-SiC implanted with Ag at 600 ^{o}C then annealed at elevated temperatures [19].

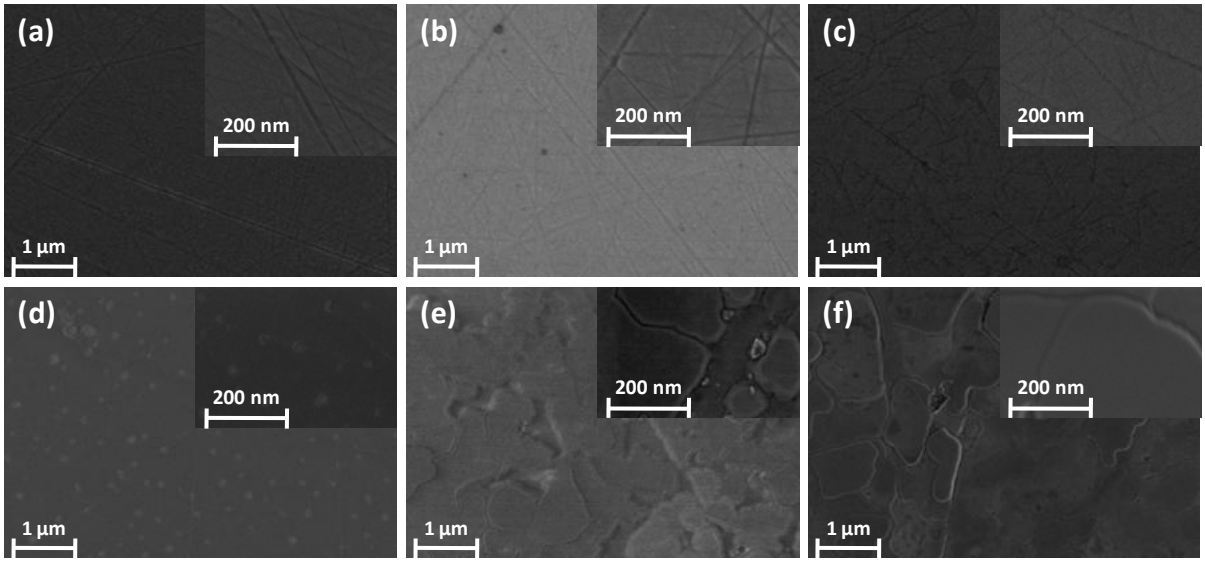

Figure 6.19: *SEM micrographs of 6H-SiC implanted with 270 keV Eu ions at 350 ^{o}C before and after annealing, (a) as-implanted sample, (b) 1000 ^{o}C annealed sample, (c) 1100 ^{o}C annealed sample, (d) 1200 ^{o}C annealed sample and (e) 1300 ^{o}C annealed sample and (f) 1400 ^{o}C.*

6.2.3 Migration results

Similar to the migration of implanted Eu into polycrystalline SiC, the migration of Eu implanted into 6H-SiC was monitored before and after each annealing step using RBS. The depth profiles of Eu implanted into 6H-SiC at RT and 350 ^{o}C after sequential annealing at temperatures from 1000 to 1400 ^{o}C in steps of 100 ^{o}C for 5 h are shown in Figure 6.20. The as-implanted Eu profiles are included for comparison. The Eu retained ratios, squares of full width at half maximum (FWHM) and peak positions as a function of annealing temperature are shown in Figure 6.21.

Annealing the room temperature implanted samples at 1000 ˚C caused migration of Eu towards the surface resulting in the formation of a small (segregated) peak on the surface of 6H-SiC, a diffusion of Eu to the bulk was also observed at this temperature. No Eu was lost at this temperature however the prominent Eu peak was broader and skewed towards the surface indicating more diffusion towards the surface compared to the diffusion towards the bulk. Similar surface peak was also observed in the Eu implanted into polycrystalline SiC at RT

annealed at 1000 ^{o}C. This surface peak was found to be due to a Eu complex compound as explained in section 6.1.3. A rather slight broadening of Eu depth profile was observed after annealing at 1100 ^{o}C compared to 1000 ^{o}C. At this temperature the broadening was accompanied by the disappearance of surface peak and about 30% loss of implanted Eu. A slight broadening accompanied by loss was further observed after annealing at 1200 ^{o}C accompanied by an additional loss of about 10%. No peak broadening was observed after annealing at 1300 ^{o}C compared to annealing at 1200 ^{o}C, however the Eu depth profile shifted towards the surface and a further 10% of Eu was lost. Annealing at 1400 ^{o}C resulted in a further peak shift towards the surface accompanied by an extra loss. A total of about 65 % of Eu implanted was lost at 1400 ^{o}C resulting in an asymmetric depth profile, and thus FWHM was not determined at this temperature.

Annealing the 350 ^{o}C implanted samples at 1000 ^{o}C resulted in no noticeable changes in the Eu depth profile. Annealing at 1100 ^{o}C resulted in a shift of Eu peak towards the surface accompanied by a narrowing of FWHM and no loss of Eu. This narrowing of FWHM of implanted Eu accompanied by no loss progressed with annealing up to 1400 ^{o}C. No significant shift towards the surface was observed after the entire annealing process. The narrowing of FWHM might be due to implanted Eu forming precipitates. Similar narrowing due to Ag forming precipitate was reported after annealing at 1100 and 1200 ^{o}C [35].

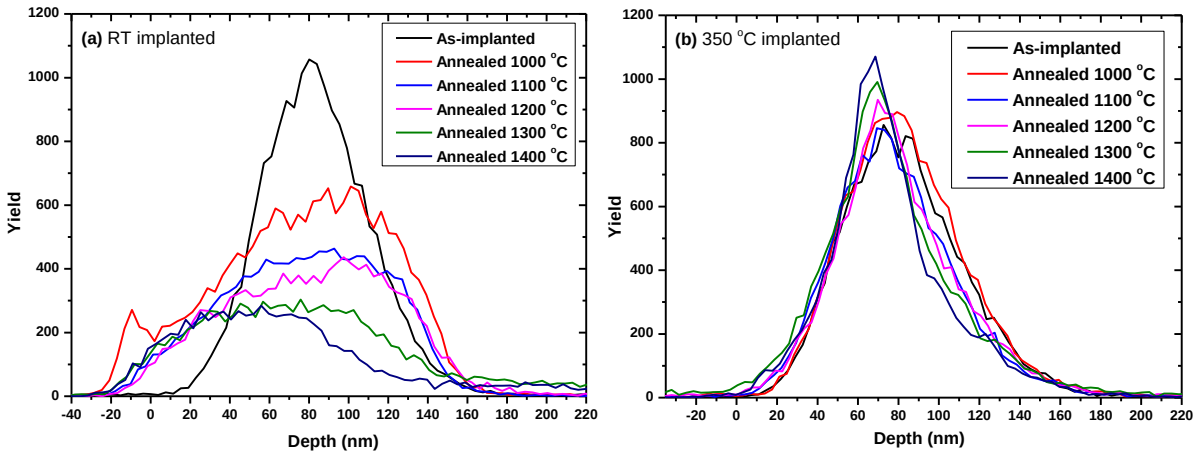

Figure 6.20: *Depth profiles of Eu (270 keV) implanted into 6H-SiC at RT and 350 ^{o}C, after isochronal annealing from 1000 to 1400 ^{o}C in steps of 100 ^{o}C for 5 hours.*

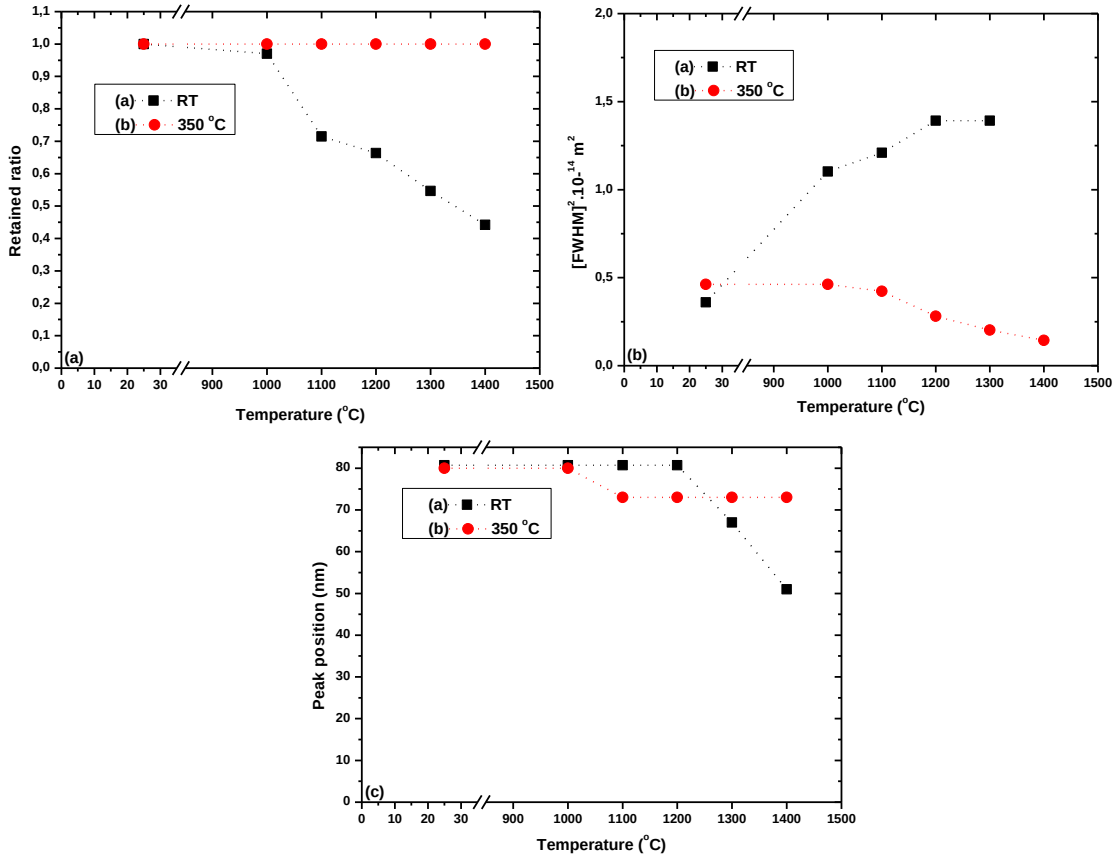

Figure 6.21: *(a) Retained ratios of Eu implanted into 6H-SiC at RT and 350 °C after isochronal annealing at 1000 to 1400 °C for 5 hours in steps of 100 °C, (b) peak shift as a function of annealing temperature and(c) full width at half maximum as a function of annealing temperature.*

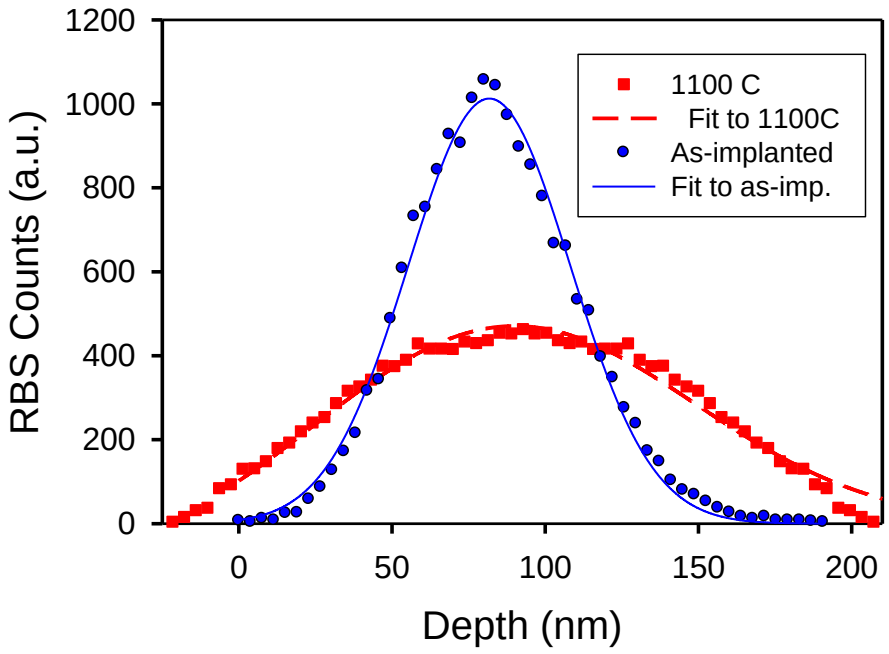

Figure 6.22: *Eu RBS depth profiles of an as-implanted sample and of the sample vacuum-annealed at 1100 ^{o}C. The solid line is least-squares fit of a Gaussian function to the as-implanted data and the broken line is the Fick solution to the 1100 ^{o}C annealed data.*

The depth profiles of the Eu implanted into 6H-SiC at room temperature and subsequently annealed (see Figure 6.20) were fitted to a general solution of Fick's differential diffusion equation for an initial Gaussian profile [17] to extract the diffusion coefficients. Figure 6.22 shows that the room temperature as-implanted Eu profile fitted well to a Gaussian function. In Figure 6.21(c) it can be seen that the peak position shifted for some of the profiles. Consequently, the peak position was one of the fitting parameters. As observed in Figure 6.20, the implanted profiles became skewed more towards the surface after annealing. The skewness increased with increasing annealing temperature while the shift towards the bulk remained unapparent. This indicates that diffusion only took place towards the surface of the 6H-SiC, i.e. the side where most of the damage due to the Eu ion implantation occurred – see Figure 6.14. This also occurred in room temperature Eu implanted poly-crystalline SiC and vacuum-annealed in the same temperature range. Consequently, only the surface side of the profiles were fitted to the above-mentioned solution of the Fick's equation. From Figure 6.20

it can also be seen that sample annealed at 1000 ^{o}C exhibited a Eu peak on the surface which is typical surface segregation, while the samples annealed at higher temperatures did not have this surface peak. This surface segregation peak distorted the diffusion profile. Consequently, in the fitting of the 1000 ^{o}C profile this surface segregation data points were not fitted. Diffusion coefficients of 0.017, 0.024 and 0.31 nm^2/s, respectively, were extracted for the 1000 ^{o}C, 1100 ^{o}C and 1200 ^{o}C profiles. However, for 1300 ^{o}C and 1400 ^{o}C annealed samples, no reliable diffusion coefficients could be extracted as the increased broadening of the Eu profile towards the surface were within the error limit of the RBS measurements. From the three diffusion coefficients an Arrhenius plot (see Figure 6.23) was made and a diffusion activation energy of 0.48 eV and a frequency factor D_o of 1.4 nm^2/s were obtained.

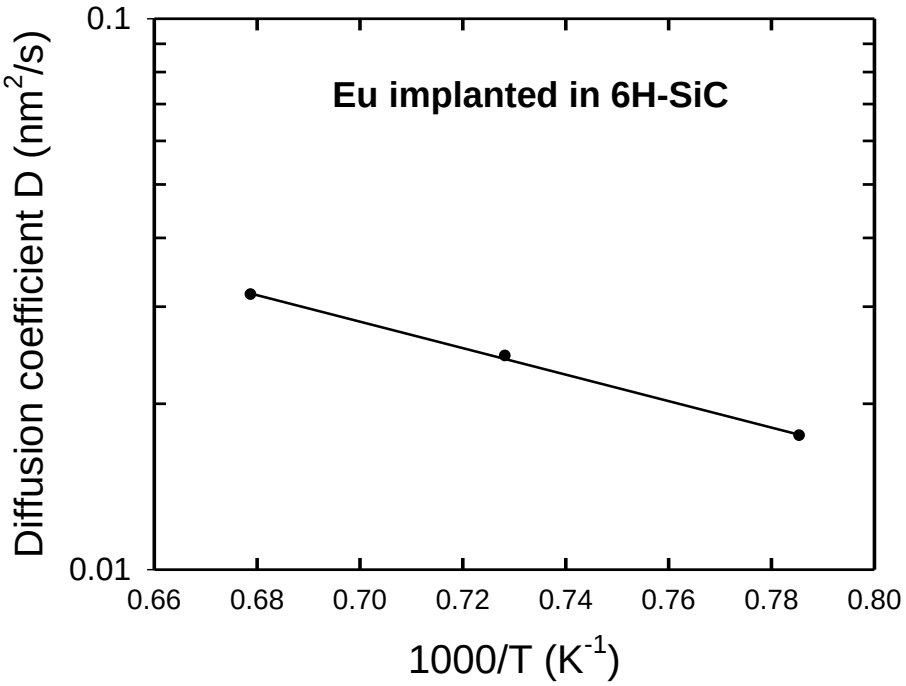

Figure 6.23: *Arrhenius plot of the diffusion coefficients of 6H-SiC implanted at room temperature with 270 keV europium ions and sequentially vacuum annealed for 5 h at 1000 ^{o}C, 1100 ^{o}C and 1200 ^{o}C, (error bars not included as the data points are all on the straight line).*

6.2.4 Discussion

These results largely agree with those of poly-crystalline 3C-SiC samples implanted at RT reported in section 6.1. The Eu implanted in poly-SiC also diffused only to the surface and there was also a Eu peak on the surface of the SiC for the sample annealed at 1000 ˚C. The values of the diffusion coefficients are also comparable. The activation energy of 0.48 eV is relatively near the 0.8 eV obtained for poly-SiC, this is not unexpected. During room temperature implantation the implanted layers of the 6H-SiC and polycrystalline SiC are amorphized. In other studies, at temperatures above 800 ˚C the amorphized layers recrystallized into polycrystalline SiC [36] [18]. The average size of the grains depend on the amount of impurities, i.e. Eu atoms, and also on the crystallinity of the substrate [37]. It is reasonable to expect that the differences in substrates, i.e. polycrystalline SiC versus single crystal 6H-SiC, will also result in different crystal sizes. The values for the average crystal sizes were measured and found to be between 29 and 409 nm for single crystalline material, as compared with the grain sizes between 100 and 270 nm for polycrystalline material presented in section 6.1 for annealing temperatures between 1000 and 1400 ^{o}C. In line with many other impurities in SiC, during the recrystallization process, implanted Eu atoms segregated to the grain boundaries where they had an easy diffusion path. The difference in the activation energies between the two sets of samples is probably due to the different stresses in the samples caused by the different amounts of implanted Eu atoms in the SiC grains, the difference in radiation-induced defects remaining in the samples and the difference in the average grain sizes, which influence the grain boundary widths. The first two factors are well known to influence diffusion [38][39] while the grain boundary diffusion model by Fisher [40] shows that grain boundary diffusion depends on the grain boundary width.

This difference in activation energies is not unusual for diffusion in SiC. The extensive review of diffusion measurements in SiC by Malherbe [18] showed that there is very large variation in the activation energies for the same diffusant between the different studies. Based on the potential barrier model for diffusion [38] the activation energy for grain boundary diffusion is usually lower than for volume diffusion. Based on this and the low solubility of Eu in SiC leading to segregation of implanted Eu atoms in the grain boundaries, the low activation energies for room temperature implanted Eu in 6H-SiC and poly-

crystalline SiC are an indication that in both cases the diffusion occurred via grain boundaries.

Dwaraknath *et al*. [41] determined both the volume and grain boundary diffusion coefficients of Eu in polycrystalline SiC in essentially the same annealing temperature range as used in this study. However, in their study they implanted FPs into a PyC which was placed between the high purity CVD β-SiC and a coating of plasma-enhanced CVD SiC which ensured that SiC was not directly implanted into SiC. They obtained activation energies of 5.5 eV and 4.7 eV for bulk and grain boundary diffusion respectively. These values are an order of magnitude higher than the ones reported in this thesis. The difference in sample microstructure, measurement and diffusion extraction techniques might be the reason for the differences. Dwaraknath *et al*. used ToF-SIMS with very low Eu concentrations while in this study, RBS was used with significantly higher Eu concentration. Higher impurity concentrations can influence the diffusion and its kinetics. The Fick's diffusion equations were derived for very low concentrations. The greatest source for the differences in the activation energies is probably the presence of high numbers of defects and grain sizes (small) in the samples of this study due to the implantation of Eu into the SiC. In another study using the same types of samples and techniques as in this study, Dwaraknath *et al*. [42] studied radiation-enhanced diffusion of Eu in poly-crystalline SiC. Their activation energies for bulk and for grain boundary diffusion were now significantly lower at 0.3 eV and 1.1 eV respectively, showing the effect of defects on diffusion. These latter values are approximately the same as what was measured in the 6H- and poly-SiC reported in this study, where the SiC contained many defects remaining from the implantation process.

The as-implanted Eu profile of 350 ^{o}C implanted 6H-SiC samples did not really differ from the room temperature implanted samples with R_p = 79 nm, ΔR_p = 29 nm compared to R_p = 82 nm, ΔR_p = 26 nm for the room temperature implantation. These two sets of values are within the error limits of the RBS measurements. However, the Eu profiles of the annealed samples implanted at the elevated temperatures were significantly different to those of the room temperature implanted ones. The profiles did not show normal diffusion behaviour, i.e. a broadening of the profiles. In fact, Figure 6.20(b) and Figure 6.21(b) show that the FWHM of the Eu profiles actually reduced slightly. As was discussed above, this difference was due to the differences in the number of defects remaining in the samples and perhaps the differences in the crystal sizes (and grain boundary widths in the polycrystalline SiC). It is known [18]

that implantation at room temperature leads to amorphization of SiC but that the SiC remains crystalline, albeit with many defects, for implantation at 350 ^{o}C. Furthermore, as was briefly discussed above the crystallite sizes between the two sets of samples will be different, also influencing the diffusion.

The results of single crystalline material implanted at 350 ^{o}C slightly agree with those of the poly-crystalline SiC implanted at 350 ^{o}C. However, in the latter sample, there was a Eu oxalate surface peak that formed on the surface after annealing at 1000 ^{o}C while this peak was not present in the single crystalline sample after annealing at the same temperature. This difference can be explained by the dissimilarities of the materials structures, the polycrystalline material has grain boundaries with defects while 6H-SiC only has radiation defects, hence Eu migrate via grain boundaries with defects.

References

[1] Ziegler, J. (2013). *SRIM Legal Disclaimer*. [online] Srim.org. Available at: http://www.srim.org/SRIM/SRIMLEGL.htm [Accessed 9 Mar. 2019].

[2] Weber, W. J. and Zhang, Y., 2019. Predicting damage production in monoatomic and multi-elemental targets using stopping and range of ions in matter code: Challenges and recommendations. *Current Opinion in Solid State and Materials Science*, 23(4), p.100757.

[3] Devanathan, R., Weber, W. and Gao, F. (2001). Atomic scale simulation of defect production in irradiated 3C-SiC. *Journal of Applied Physics*, 90(5), pp.2303-2309.

[4] Snead, L., Zinkle, S., Hay, J. and Osborne, M., 1998. Amorphization of SiC under ion and neutron irradiation. *Nuclear Instruments and Methods in Physics Research Section B: Beam Interactions with Materials and Atoms*, 141(1-4), pp.123-132.

[5] Perova, T., Wasyluk, J., Kukushkin, S., Osipov, A., Feoktistov, N. and Grudinkin, S. (2010). Micro-Raman mapping of 3C-SiC thin films grown by solid–gas phase epitaxy on Si (111). *Nanoscale Research Letters*, 5(9), pp.1507-1511.

[6] Rohmfeld, S., Hundhausen, M. and Ley, L. (1998). Raman scattering in polycrystalline3C−SiC: Influence of stacking faults. *Physical Review B*, 58(15), pp.9858-9862.

[7] Zinkle, S. and Snead, L., 1996. Influence of irradiation spectrum and implanted ions on the amorphization of ceramics. *Nuclear Instruments and Methods in Physics Research Section B: Beam Interactions with Materials and Atoms*, 116(1-4), pp.92-101.

[8] Costantini, J., Miro, S. and Pluchery, O., 2017. FTIR study of silicon carbide amorphization by heavy ion irradiations. *Journal of Physics D: Applied Physics*, 50(9), p.095301.

[9] Xu, Z., He, Z., Song, Y., Fu, X., Rommel, M., Luo, X., Hartmaier, A., Zhang, J. and Fang, F., 2018. Topic Review: Application of Raman spectroscopy characterization in micro/nano-machining. *Micromachines*, 9(7), p.361.

[10] Loudon, R. J., 1965. Theory of the resonance Raman effect in crystals. *Journal de Physique*, 26(11), pp.677-683.

[11] Morhange, J., Beserman, R. and Balkanski, M., 1974. Raman study of the vibrational properties of implanted silicon. *Physica Status Solidi (a)*, 23(2), pp.383-391.

[12] Wendler, E., Heft, A. and Wesch, W. (1998). Ion-beam induced damage and annealing behaviour in SiC.*Nuclear Instruments and Methods in Physics Research Section B: Beam Interactions with Materials and Atoms*, 141(1-4), pp.105-117.

[13] Snead, L., Nozawa, T., Katoh, Y., Byun, T., Kondo, S. and Petti, D. (2007). Handbook of SiC properties for fuel performance modeling. *Journal of Nuclear Materials*, 371(1-3), pp.329-377.

[14] Idris, M., Konishi, H., Imai, M., Yoshida, K. and Yano, T. (2015). Neutron irradiation swelling of sic and sicf/sic for advanced nuclear applications. *Energy Procedia*, 71, pp.328-336.

[15] Miro, S., Costantini, J., Sorieul, S., Gosmain, L. and Thomé, L. (2012). Recrystallization of amorphous ion-implanted silicon carbide after thermal annealing. *Philosophical Magazine Letters*, 92(11), pp.633-639.

[16] Ishimaru, M., Bae, I., Hirotsu, Y., Matsumura, S. and Sickafus, K. (2002). Structural relaxation of amorphous silicon carbide. *Physical Review Letters*, 89(5).

[17] Malherbe, J. B, Selyshchev, P., Odutemowo, O. S, Theron, C. C, Njoroge, E. G, Langa, D. F. and Hlatshwayo, T. T, 2017. Diffusion of a mono-energetic implanted species with a Gaussian profile. *Nuclear Instruments and Methods in Physics Research Section B: Beam Interactions with Materials and Atoms*, 406, pp.708-713.

[18] Malherbe, J. B, 2013. Topical review. Diffusion of fission products and radiation damage in SiC.*Journal of Physics D: Applied Physics*, 46(47), p.473001.

[19] Hlatshwayo, T. T, Malherbe, J. B, van der Berg, N. G, Botha, A. J. and Chakraborty, P., 2012. Effect of thermal annealing and neutron irradiation in 6H-SiC implanted with silver at 350°C and 600°C. *Nuclear Instruments and Methods in Physics Research Section B: Beam Interactions with Materials and Atoms*, 273, pp.61-64.

[20] Friedland, E., Malherbe, J. B, van der Berg, N. G, Hlatshwayo, T. T, Botha, A. J, Wendler, E. and Wesch, W. (2009). Study of silver diffusion in silicon carbide. *Journal of Nuclear Materials*, 389(2), pp.326-331.

[21] Demri, B. and Muster, D., 1995. XPS study of some calcium compounds. *Journal of Materials Processing Technology*, 55(3-4), pp.311-314.

[22] Sreemany, M., Ghosh, T., Pai, B. and Chakraborty, M., 1998. XPS Studies on the oxidation behavior of sic particles. *Materials Research Bulletin*, 33(2), pp.189-198.

[23] Bermudez, V., 1988. Growth and structure of aluminum films on (001) silicon carbide. *Journal of Applied Physics*, 63(10), pp.4951-4959.

[24] Miyoshi, K. and Buckley, D., 1982. XPS, AES and friction studies of single-crystal silicon carbide. *Applications of Surface Science*, 10(3), pp.357-376.

[25] Mizokawa, Y., Geib, K. and Wilmsen, C., 1986. Characterization of β-SiC surfaces and the Au/SiC interface. *Journal of Vacuum Science & Technology A: Vacuum, Surfaces, and Films*, 4(3), pp.1696-1700.

[26] Mizokawa, Y., Nakanishi, S., Komoda, O., Miyase, S., Diang, H., Wang, C., Li, N. and Jiang, C., 1990. Differences in Auger electron spectroscopy and x-ray photoelectron spectroscopy results on the bonding states of oxygen with β-SiC(100) surfaces. *Journal of Applied Physics*, 67(1), pp.264-269.

[27] Wagner, C., Passoja, D., Hillery, H., Kinisky, T., Six, H., Jansen, W. and Taylor, J., 1982. Auger and photoelectron line energy relationships in aluminum–oxygen and silicon–oxygen compounds. *Journal of Vacuum Science and Technology*, 21(4), pp.933-944.

[28] Karasek, K., Bradley, S., Donner, J., Yeh, H., Schienle, J. and Fang, H., 1989. Characterization of silicon carbide whiskers. *Journal of the American Ceramic Society*, 72(10), pp.1907-1913.

[29] Wang, Y., Kusumoto, K. and Li, C., 2012. XPS analysis of sic films prepared by radio frequency plasma sputtering. *Physics Procedia*, 32, pp.95-102.

[30] Swift, P., 1982. Adventitious carbon? the panacea for energy referencing?. *Surface and Interface Analysis*, 4(2), pp.47-51.

[31] Uwamino, Y., Ishizuka, T. and Yamatera, H., 1984. X-ray photoelectron spectroscopy of rare-earth compounds. *Journal of Electron Spectroscopy and Related Phenomena*, 34(1), pp.67-78.

[32] Zheng, M., Swaminathan, N., Morgan, D. and Szlufarska, I., 2013. Energy barriers for point-defect reactions in3C-SiC. *Physical Review B*, 88(5).

[33] Lin, S., Chen, Z., Li, L. and Yang, C. (2012). Effect of impurities on the Raman scattering of 6H-SiC crystals. *Materials Research*, 15(6), pp.833-836.

[34] Ahn, H., Lee, D. and Um, Y., 2017. Substrate temperature effects on DC Sputtered Mo thin film. *Applied Science and Convergence Technology*, 26(1), pp.11-15.

[35] Hlatshwayo, T., Malherbe, J., van der Berg, N., Prinsloo, L., Botha, A., Wendler, E. and Wesch, W., 2012. Annealing of silver implanted 6H–SiC and the diffusion of the silver. *Nuclear Instruments and Methods in Physics Research Section B: Beam Interactions with Materials and Atoms*, 274, pp.120-125.

[36] Malherbe, J. B., van der Berg, N. G., Kuhudzai, R. J., Hlatshwayo, T. T., Thabethe, T. T., Odutemowo, O. S., Theron, C. C., Friedland, E., Botha, A. J. and Wendler, E., 2015. Scanning electron microscopy of the surfaces of ion implanted SiC.*Nuclear Instruments and Methods in Physics Research Section B: Beam Interactions with Materials and Atoms*, 354, pp.23-27.

[37] Thompson, C., 2000. Structure evolution during processing of polycrystalline films. *Annual Review of Materials Science*, 30(1), pp.159-190.

[38] Boltaks, B., 1963. Diffusion in semiconductors. *Infosearch Ltd, New York,*.

[39] Mehrer, H., 2007. Diffusion in solids. *Springer, Berlin*.

[40] Fisher, J., 1951. Calculation of diffusion penetration curves for surface and grain boundary diffusion. *Journal of Applied Physics*, 22(1), pp.74-77.

[41] Dwaraknath, S. and Was, G. (2016). The diffusion of cesium, strontium, and europium in silicon carbide. *Journal of Nuclear Materials*, 476, pp.155-167.

[42] Dwaraknath, S. and Was, G. (2016). Radiation enhanced diffusion of cesium, strontium, and europium in silicon carbide. *Journal of Nuclear Materials*, 474, pp.76-87.

CHAPTER 7

Conclusions

In this work, the effect of radiation damage on the migration behaviour of Eu implanted into silicon carbide (both polycrystalline and 6H-SiC) was investigated in temperatures ranging from 1000 up to 1400 ^{o}C in steps of 100 ^{o}C. A direct implantation was performed on samples at different temperatures (RT, 350 and 600 ^{o}C) to introduce different amount of radiation damage in the samples. Samples implanted at RT retained an amorphous layer while samples implanted at 350 and 600 ^{o}C retained crystallinity with defects albeit more defects were retained in the 350 ^{o}C implanted samples compared to 600 ^{o}C implanted samples. Thermal annealing of the as-implanted samples caused some re-crystallization of SiC to a certain extent, however, the initial structure of virgin SiC was not achieved up to the highest annealing temperature of 1400 ^{o}C. Annealing both RT implanted samples at 1000 ^{o}C resulted in the diffusion of Eu more towards the surface accompanied by the formation of europium oxalate surface peak. Further annealing of the RT implanted samples (initially annealed at 1000 ^{o}C) at 1100 ^{o}C resulted in significant loss of Eu accompanied by the disappearance of europium oxalate surface peak due to sublimation. Diffusion of implanted Eu accompanied by some loss progressed with annealing temperature. Diffusion coefficients of: 0.015, 0.033 and 0.035 nm^2/s (in RT implanted polycrystalline SiC) and 0.017, 0.024 and 0.31 nm^2/s (in the RT implanted 6H-SiC) at annealing temperatures of 1000, 1100 and 1200 ^{o}C respectively were extracted. The activation energies of 0.48 eV and 0.8 eV were obtained for RT implanted 6H-SiC and poly-SiC respectively. These activation energies are relatively close to each other indicating the same mechanism in both samples. The same diffusion mechanism was expected after annealing especially at 1000 ^{o}C as both samples were initially amorphous while the similarity at elevated temperatures might be an indication of the amorphized 6H-SiC recrystallized to polycrystalline SiC.

Annealing the 350 ^{o}C implanted samples resulted in different migration behaviour due to the effect of grain boundaries in the polycrystalline SiC. Annealing the polycrystalline SiC implanted at 350 ^{o}C resulted in the formation of rather small europium oxalate surface peak compared to the RT samples annealed at 1000 ^{o}C, while no changes were observed in the 350

^{o}C implanted 6H-SiC annealed samples. Further annealing of the 350 ^{o}C implanted samples at elevated temperatures caused progressive loss of implanted Eu in the polycrystalline sample with no loss observed in the 6H sample. Similar to the polycrystalline RT implanted sample, the loss was significant and was accompanied by the disappearance of europium oxalate surface peak due to sublimation during annealing at 1100 ^{o}C. Further loss at elevated temperatures was due to migration via grain boundaries. Only narrowing of the profiles was observed in the 350 ^{o}C implanted 6H-SiC sample annealed at elevated temperatures indicating some segregation of implanted Eu at these temperatures.

For the 600 ^{o}C implanted polycrystalline SiC, Eu was well retained, and no significant loss was observed at all annealing temperatures. This is because the grain boundaries observed on the surface were mostly narrow and intact as compared to the 350 ^{o}C implanted polycrystalline samples. The broadening of the 600 ^{o}C implanted depth profile was observed after annealing at 1100 ^{o}C and higher temperatures. However, the diffusion coefficients of these profiles could not be extracted due to the error limit of the RBS system used.

Given the similarity of diffusion behaviour in the RT implanted samples of poly-SiC and 6H-SiC, it can be seen that the type of diffusion mechanism taking place is of the same type in both samples, and therefore radiation enhanced. As it is known, the small activation energies for diffusion are usually ascribed to grain boundary diffusion or a kind of fast diffusion mechanism, it becomes clear that the grain boundary diffusion cannot be the immediate mechanism through which diffusion is taking place in the RT implanted samples. Since the activation energies in this study are similar to that predicted for Si interstitial diffusion in SiC, by Zheng *et al* [1], it can be concluded that the type of diffusion through which Eu diffuses to the surface in the RT implanted samples is mostly via interstitial diffusion, which seem to be mostly enhanced by radiation damage. Eu in the case of 350 ^{o}C implanted polycrystalline migrated to the surface purely via grain boundaries, this is true because the grain boundaries are not present in the 6H-SiC and thus neither migration nor diffusion was observed in this sample. A conclusion can be made that radiation induced defects enhances migration of Eu in the 350 ^{o}C implanted sample of poly-SiC, while the same defects create trapping sites in the 350 ^{o}C implanted sample of 6H-SiC.

The observations clearly indicate no migration of Eu in 6H-SiC and indicating the role of radiation damage in the enhancement of migration of Eu in SiC. Still, the diffusion

coefficients obtained in the RT implanted samples are essentially small, and therefore Eu release into the reactor's cooling system should be prevented by the SiC coatings of about 35 μm.

References

[1] Zheng, M., Swaminathan, N., Morgan, D. and Szlufarska, I., 2013. Energy barriers for point-defect reactions in3C-SiC. *Physical Review B*, 88(5).

Future studies

The results of this study imply that Eu diffusion is controlled by the amount of radiation retained after implantation. In a nuclear environment where continuous irradiation of SiC with FPs and neutrons with energies ranging from <0.001 eV to > 10 MeV which includes the range of swift heavy ions (SHI) in the presence of helium from nuclear decay and transmutation, is taking place, these results are of crucial important. To get holistic image of the migration behaviour of Eu in SiC, the following studies needs to be done:

- The migration of Eu implanted into SiC will be performed at atomic scale using transmission electron microscopy (TEM), especially In-situ TEM.
- Thermal annealing studies should be done at temperatures where diffusion was detected in this study, to collect enough data to determine more accurate diffusion coefficients.
- The effect of swift heavy ions (SHEs) irradiation on the migration behavior of Eu implanted into SiC.
- The effect of helium/alpha in the migration of the implanted Eu.
- The synergetic effect of other fission products in the migration behaviour of Eu in SiC need to be investigated.